

Calcium Vapour Deposition on Semiconducting Polymers Studied by
Adsorption Calorimetry and Visible Light Absorption

by

Sherman Siu-Man Hon

B.Sc., The University of British Columbia, 2001

A THESIS SUBMITTED IN PARTIAL FULFILLMENT OF
THE REQUIREMENTS FOR THE DEGREE OF

DOCTOR OF PHILOSOPHY

in

THE FACULTY OF GRADUATE STUDIES

(Chemistry)

THE UNIVERSITY OF BRITISH COLUMBIA
(Vancouver)

June 2008

© Sherman Siu-Man Hon, 2007

Abstract

A novel UHV microcalorimeter has been used to study the interaction between calcium and three polymers: MEH-PPV, MEH-PPP and P3HT. All three polymers behave differently in their reaction kinetics with calcium. On MEH-PPV we measure $45 \mu\text{J}/\text{cm}^2$ of heat generated in excess of the heat of bulk metal growth, $120 \mu\text{J}/\text{cm}^2$ for MEH-PPP, and $100 \mu\text{J}/\text{cm}^2$ for P3HT. Comparison of the MEH-PPV and MEH-PPP data indicate that the initial reaction of calcium with MEH-PPV occurs at the vinylene group. We propose, based on hypothetical models, that calcium reacts with the vinylene groups of MEH-PPV with a reaction heat of 360 kJ/mol and at a projected surface density of $1.7 \text{ sites}/\text{nm}^2$, while it reacts with the phenylene groups of MEH-PPP in a two-step process with reaction heats of 200 and 360 kJ/mol respectively, at a projected surface density of $3.5 \text{ sites}/\text{nm}^2$.

Optical absorption experiments, using either a 1.85 eV diode laser or a xenon lamp coupled to a scanning monochromator, have also been performed using the same calorimeter sensor. In the case of MEH-PPV, using the laser we find an optical absorption cross-section of $3 \times 10^{-17} \text{ cm}^2$ per incident calcium atom at low coverages. The change in absorptance at higher coverages correlates perfectly with the population of reacted Ca atoms determined calorimetrically. The size of the absorbance cross-section, and its position just within the band gap of the polymer, are consistent with the reaction being one of polaron formation. Calcium does not appear to dope P3HT, while the photon energy range of 1.5 to 3.75 eV used in these experiments is likely too small for probing polaronic energy states in MEH-PPP.

Table of Contents

Abstract.....	ii
Table of Contents	iii
List of Tables	v
List of Figures.....	vi
Acknowledgements	ix
1. Introduction.....	1
2. Calcium Chemistry	11
2.1. Ionic Species	11
2.2. Organometallic Species	12
2.3. Interactions with Semiconducting Polymers	19
2.3.1. MEH-PPV	24
2.3.2. MEH-PPP.....	25
2.3.3. P3HT	26
3. Experimental	28
3.1. Apparatus	28
3.2. Experimental Details.....	34
3.3. Processing of Raw Data from Apparatus.....	42
3.3.1. Extent of Calcium Deposition.....	42
3.3.2. Measured Heat and Standard Enthalpy.....	43

4. Calorimetric Studies	45
4.1. MEH-PPV	45
4.2. Oxygen-treated MEH-PPV	53
4.3. MEH-PPP.....	56
4.4. P3HT	71
4.5. Summary of Calorimetric Studies.....	77
5. Optical Studies	78
5.1. Laser Studies.....	79
5.1.1. Modelling of Data.....	79
5.1.2. Absorption Cross-sections	92
5.2. Xenon Lamp Studies.....	102
5.3. Summary of Optical Studies	111
6. Conclusion and Proposals for future work.....	113
Bibliography	116
Appendix 1.....	124

List of Tables

Table 4.1: Standard enthalpy of formation for some simple organic molecules 68

Table 4.2: Standard enthalpy of hydrogenation for some simple organic molecules 68

List of Figures

Figure 1.1: Schematic of a simple 3-layer OLED device.....	2
Figure 1.2: Chemical structures of some technologically important semiconducting polymers.....	4
Figure 1.3: Non-equilibrated schematic energy level diagram for the simple 3-layer OLED device	5
Figure 1.4: Work functions of metals of importance to OLED devices and band edge energies for several semiconducting polymers	6
Figure 1.5: Chemical structures of the polymers included in Figure 1.4	7
Figure 1.6: Chemical structures of the three polymers studied in this thesis.....	9
Figure 2.1: Structure of Ca(Cp) ₂	13
Figure 2.2: Structure of Ca(Cp) ₂	14
Figure 2.3: Structure of Ca(Cp*) ₂	15
Figure 2.4: Molecular structure of Ca(CHPh=C(CH ₃)—C(CH ₃)=CHPh)(THF) ₄	17
Figure 2.5: Molecular structure of Ca{[Si(CH ₃) ₃]CH=CH—CH[Si(CH ₃) ₃] } ₂ (THF) ₂	18
Figure 2.6: Schematic energy diagram of common species in the doping of semiconducting polymers	20
Figure 2.7: Diagrams for explaining the energies of polaronic levels	21
Figure 2.8: Chemical picture of polarons using PPV as a model.....	23
Figure 3.1: Schematic diagram of our UHV calorimeter	30
Figure 3.2: Schematic diagram of the sensor assembly	31
Figure 3.3: Typical voltage data collected during calorimetry experiments.....	36
Figure 3.4: Peak shape after manipulation of raw voltage data	38
Figure 4.1: Calorimetric data of MEH-PPV with calcium.....	46
Figure 4.2: Logarithmic plot of MEH-PPV calorimetric data.....	48

Figure 4.3: Chemical structure of the polyimide pyromellitic dianhydride-oxydianiline PMDA-ODA	52
Figure 4.4: Calorimetric data of oxygen treated MEH-PPV	54
Figure 4.5: Calorimetric data of MEH-PPP	57
Figure 4.6: Integrated reaction heats for MEH-PPV and MEH-PPP	58
Figure 4.7: Heat curves generated using the 3-state, 5-parameter model	64
Figure 4.8: Various best fits for MEH-PPP calorimetric data using the 3-state, 5-parameter model	65
Figure 4.9: Calorimetric data of P3HT.....	72
Figure 4.10: Fitting of P3HT calorimetry data using the 3-state model.....	73
Figure 4.11: Comparison of integrated reaction heats amongst MEH-PPV, MEH-PPP and P3HT	74
Figure 5.1: 1.85 eV (671 nm) laser diode data for the P3HT/Ca system	80
Figure 5.2: 1.85 eV laser data for P3HT, compared with calculated percentage absorbance changes assuming bulk metallic overlayer	84
Figure 5.3: Calculation of the percentage absorptance change at 1.85 eV for P3HT where the near-surface region is treated as a MG film	87
Figure 5.4: Calculation of the percentage absorptance change at 1.85 eV for P3HT using various effective-medium models	88
Figure 5.5: Best fit curve for the 1.85 eV P3HT laser experiments using a MG model with a Drude-metal	90
Figure 5.6: Percentage absorptance changes at 1.85 eV for all three polymers studied in this thesis.....	93
Figure 5.7: Laser data at 1.85 eV and calorimetry data for MEH-PPV	94
Figure 5.8: Plot of $n\sigma$ as a function of calcium deposition for P3HT	96
Figure 5.9: Plot of $n\sigma$ as a function of calcium deposition for MEH-PPV	97

Figure 5.10: Schematic diagram of possible transitions, and thus absorption energies, for negative polarons	100
Figure 5.11: Absorptance spectra for the three polymers, as well as the gold substrate, as collected using an integrating sphere	103
Figure 5.12: Comparison between measured absorptance of the gold substrate <i>ex situ</i> in integrating sphere and the calculation	104
Figure 5.13: Comparison between measured MEH-PPV absorptance <i>ex situ</i> in integrating sphere and the best fit calculation	105
Figure 5.14: Comparison between measured P3HT absorptance <i>ex situ</i> in integrating sphere and calculation.....	106
Figure 5.15: Comparison between measured MEH-PPP absorptance <i>ex situ</i> in integrating sphere and calculations for 11 nm, 14 nm (best fit), and 20 nm thick films	107
Figure 5.16: Percentage absorptance change upon the deposition of 4.5 atoms/nm ² of calcium for all three polymers as a function of photon energy	110
Figure A1.1: Schematic diagram of a 3-phase system	128

Acknowledgements

I would like to thank my previous research supervisor, Dr. J. Todd Stuckless, for his continued support, patience, and guidance, especially in light of his departure from the department, in helping with the completion of this thesis. Thanks are also extended to my current research supervisor, Prof. Dan Bizzotto, for the helpful discussions we have had, and for assuming the supervisory role after Todd's departure. As well, I would like to thank my defence examiners, Prof. Edward Grant, Prof. Andrew MacFarlane, Prof. Tom Tiedje, and Prof. Paul Rountree, for the important changes they have suggested.

I would like to acknowledge the excellent work by the members of the machine shop and electronics shop, who were very helpful in repairing broken parts from the apparatus to keep it in working order, as well as fabricating new parts required for the experiments.

I would like to also thank past members of the Metal/Molecule Interfaces group: Dr. Richard Murdey, Dr. Jan Richter, Dr. Youngku Sohn, Mr. Sam Liang, Ms. Sebine Hirth, and Mr. Gerald Li, for their contribution in the project, as well as their encouragement and friendship.

As well, I am very grateful for the love and support from my parents Edward and Stella, my girlfriend Janet, my sister Terry, and my friends for seeing me through the long journey that has been my graduate studies.

Lastly, I would like to acknowledge the financial support that was provided by the Natural Science and Engineering Research Council, and the University of British Columbia.

1. Introduction

In the world of electronics, one of the most pursued areas of research is in display technologies. Increasingly, traditional cathode ray tube displays are being replaced by less bulky liquid crystal and plasma displays, while the next generation of displays are developed. One of the most promising classes of these future displays are based on organic light emitting diodes (OLED).¹ An OLED is, in its simplest form, an organic layer sandwiched by electrodes, most often using the transparent indium tin oxide (ITO) as the anode for light to escape from the device.^{2,3} A schematic drawing of this device is shown in **Figure 1.1**. This organic layer can be a semiconducting molecular layer, or a semiconducting polymer. An OLED based on polymer (PLED) is particularly attractive when the polymer is soluble in common solvents, since this promises easy manufacturing using spin-coating or dip-coating techniques, as opposed to vacuum deposition with molecular semiconductors. Solubility in common solvents also promises novel device fabrication by “ink-jet printing”, where the dissolved semiconductor is accurately sprayed onto substrates using ink-jet printer heads adapted for the purpose.⁴

Semiconducting polymers owe their electronic properties to the conjugated backbone. While typical small organic molecules are insulators because of the wide band gaps between their bonding and anti-bonding orbitals, the formally alternating double bonds in these polymer chains give rise to the narrow band gap necessary for OLED operation.⁵ By having different backbone structures, the conjugation length can be altered and thus different band gaps can be realized in different classes of polymers. The choice of side groups can also be used to modify the band gap of the polymer, through a combination of direct electronic influences and steric interactions, i.e. twisting of the polymer backbone which in turn alters the conjugation length. As well, careful choice of side groups is a means of facilitating solubility in common solvents to ease device fabrication.

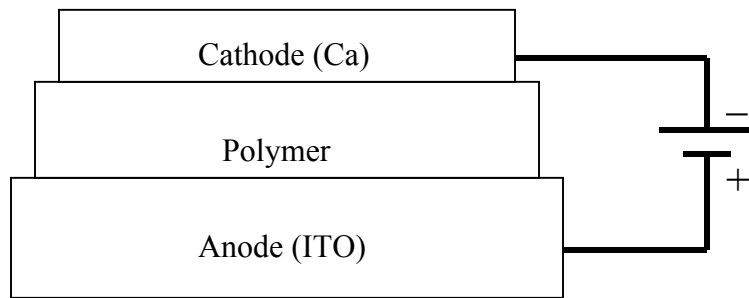


Figure 1.1: Schematic of a simple 3-layer OLED device

Note that the cathode is composed of a low work function metal, typically calcium, while the anode is typically indium tin oxide. Also of note is that while functionally a 3-layer device is sufficient, current state-of-the-art devices usually have charge injection layers to aid efficiency.

There are a few different families of conjugated polymers of interest for technological development: poly(para-phenylenevinylene), poly(para-phenylene), polyfluorene, and polythiophene are some examples. While researchers have investigated the first three polymers in terms of OLED applications, polythiophene has been studied primarily for its feasibility in transistors thanks to its high charge carrier mobility.⁶ The chemical structures of these materials are shown in **Figure 1.2**.

While some researchers study these polymers and fine tune their electronic properties,⁷⁻¹⁰ others study the actual fabrication of devices.¹¹⁻¹³ **Figure 1.3** shows a schematic of the energy levels of the various layers in the simple 3-layer OLED shown in **Figure 1.1**. From this figure, we see that it is desirable to have a cathode made of a low work function material to minimize the electron injection barrier due to the high energy of the lowest unoccupied molecular orbital (LUMO) in polymeric semiconductors. On the contrary, a high work function material is desirable as an anode to minimize the hole injection barrier given the polymer's low lying highest occupied molecular orbital (HOMO). A commonly used material for cathode fabrication is thus calcium metal, while the ceramic indium tin oxide (ITO) is often used as the anode both for its transparency to visible light and relatively high work function. **Figure 1.4** shows both the work functions of several metals of interest in OLED research as well as two that are commonly used as interconnect conductors, and the band edge alignments for a few semiconducting polymers.¹⁴⁻²⁰

As well as energy level alignment, there are many other interfacial issues that must be understood in order to fabricate efficient devices, e.g., adhesion between polymer and electrode,²¹ electrode metal grain size effects,²² the possibility of an insulating film between electrode and polymer due to the high reactivity of the low work function metal used,²³ and electro-migration of electrode material into polymer,²⁴ to name a few. To properly design OLED devices then, the interfaces between electrodes and polymer must be thoroughly understood. Indeed, there have been extensive investigations in the literature on metal-polymer interfaces, most of which have been

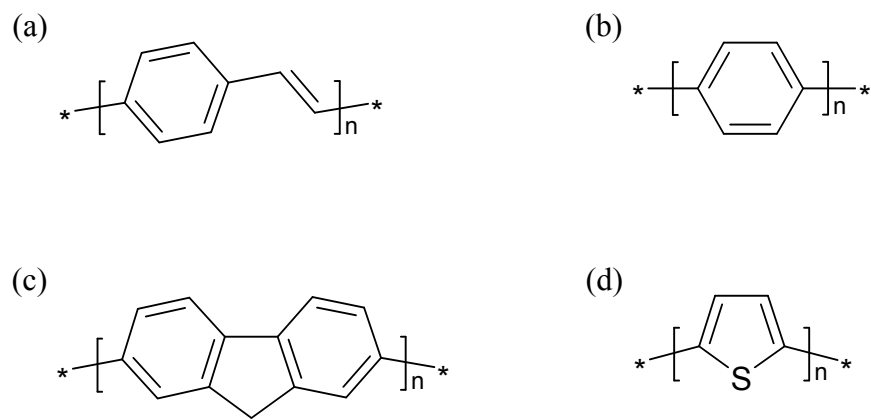


Figure 1.2: Chemical structures of some technologically important semiconducting polymers

- (a) poly(phenylenevinylene) (PPV); (b) poly(phenylene) (PPP);
- (c) polyfluorene (PF); and (d) polythiophene (PT).

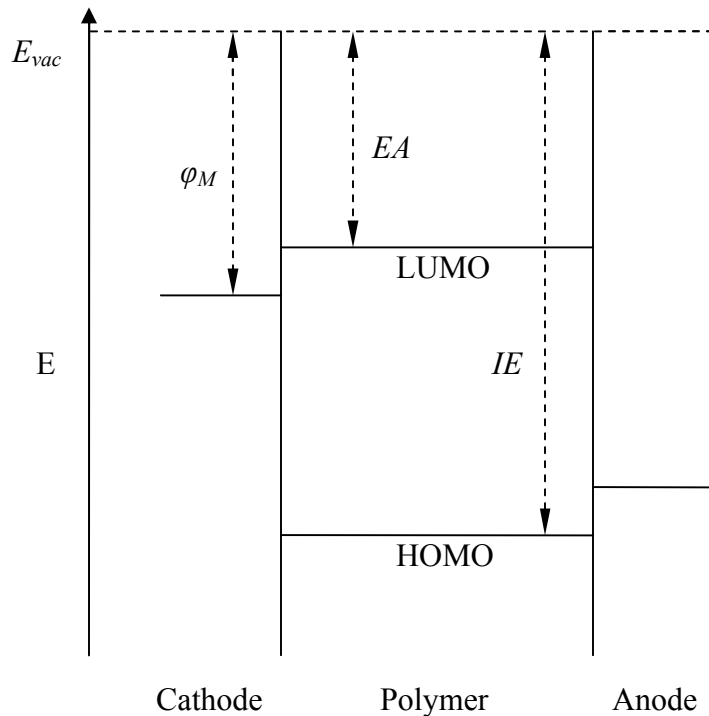


Figure 1.3: Non-equilibrated schematic energy level diagram for the simple 3-layer OLED device

Note that the cathode needs to be a low work function (φ_M) material for efficient electron injection. E_{vac} is the vacuum energy level, EA and IE are the electron affinity and ionization potential of the polymer respectively, while LUMO and HOMO are the lowest unoccupied molecular orbital and highest occupied molecular orbital respectively.

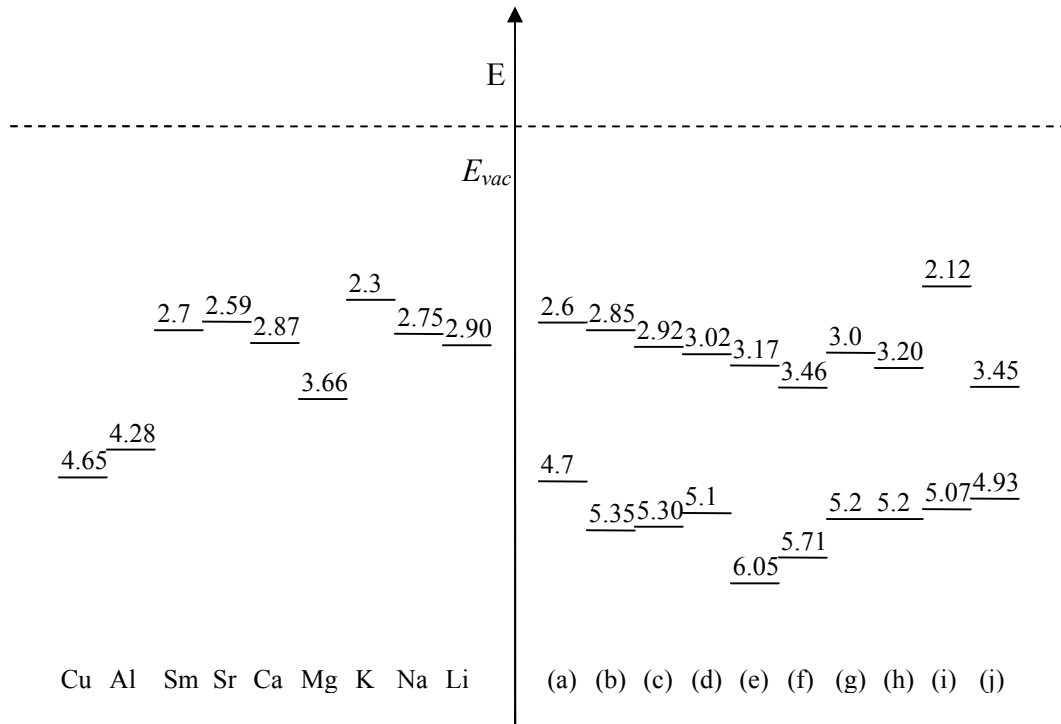


Figure 1.4: Work functions of metals of importance to OLED devices and band edge energies for several semiconducting polymers

The work functions are on the left hand side, while the band edge energies are on the right hand side: (a) MEH-PPV,¹⁴ (b) PPV,^{14,15} (c) NOD-PPV,¹⁶ (d) CN-PPV,¹⁴ (e) DD-PPV,¹⁷ (f) 2,5-DCN-PPV,¹⁵ (g) P3HT,¹⁸ (h) PT,¹⁹ (i) PFO,²⁰ (j) PA.¹⁹ The chemical structures of these polymers are shown in Figure 1.5.

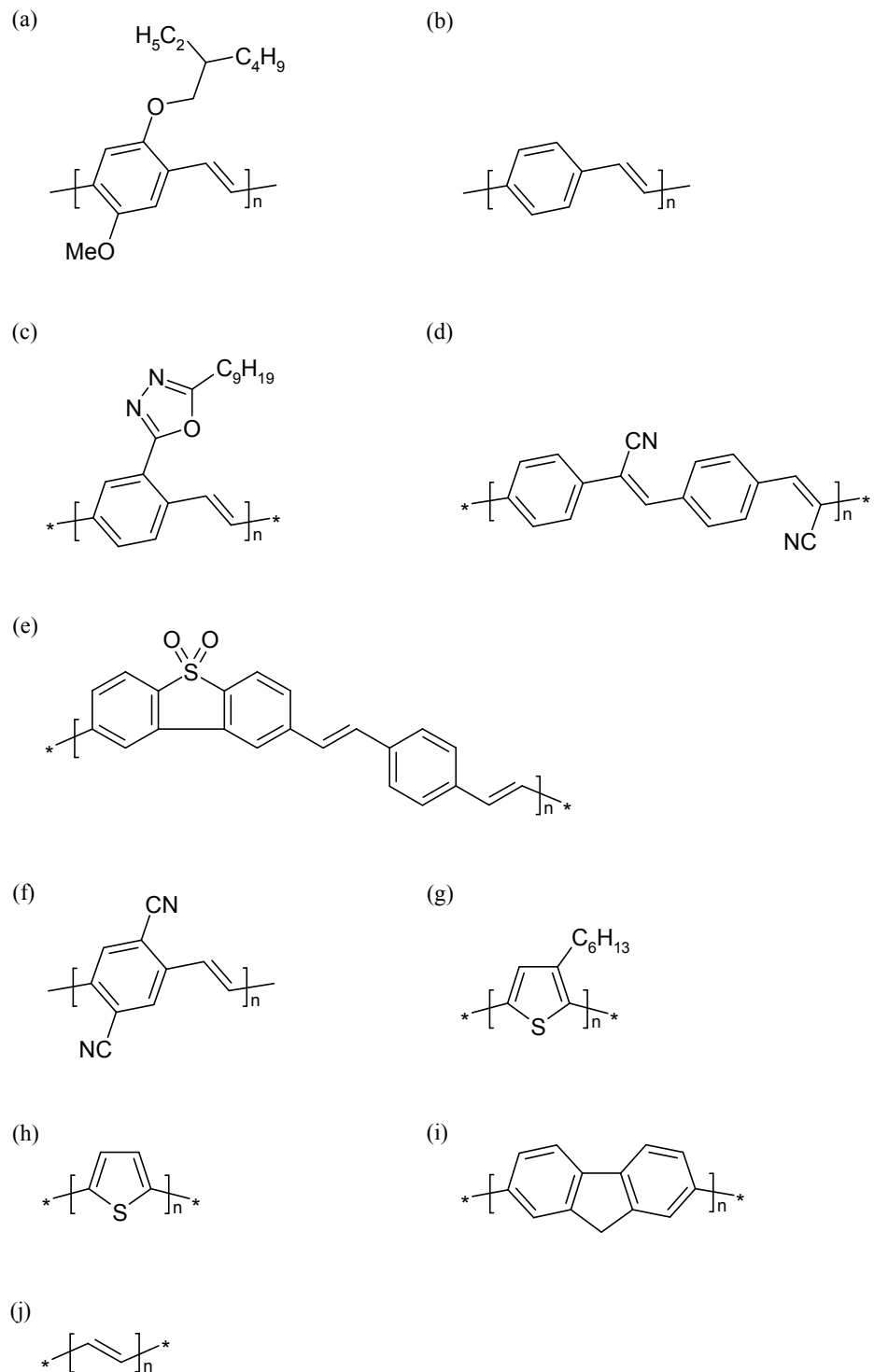


Figure 1.5: Chemical structures of the polymers included in **Figure 1.4**

carried out using spectroscopic techniques as will be discussed in the next chapter. While spectroscopy is useful, in fact very powerful, in deciphering the details of these interfaces, it is nevertheless beneficial to also study these systems using methods other than the measurement of electronic energies. We therefore introduce calorimetry so that new, complementary information might be obtained to further understand these systems. These calorimetric studies have been performed on a few metal-polymer interfaces, namely those between calcium and three particular polymers, poly[2-methoxy,5-(2'-ethylhexyloxy)-para-phenylenevinylene] (MEH-PPV), and poly[2-methoxy,5-(2' ethylhexyloxy)-para-phenylene] (MEH-PPP). The polymer poly(3-hexylthiophene) (P3HT) has also been studied for this work. Even though it is not normally studied for usage in OLED devices, this polymer was recently studied in detail using two-photon photoemission spectroscopy within our group,²⁵ thus making it an interesting material to study with calorimetry. The chemical structures of MEH-PPV, MEH-PPP and P3HT are depicted in **Figure 1.6**.

Taking advantage of the calorimeter's capabilities, simple optical spectroscopy has also been performed on these systems. This demonstrates the unique capabilities of the apparatus in our laboratory: by means of calorimetry, information can be gained about the strength of the interactions between the deposited metal and polymer. Moreover, the kinetics of these interactions can be elucidated through the shapes of the heat curves as a function of the amount of metal deposited. Furthermore, spectroscopy can give information with regards to phenomenon such as doping under conditions identical to those in calorimetric experiments, as well as potentially yielding a second means of determining reaction kinetics through the evolution of absorption as a function of deposited metal.

There are many different possible outcomes when calcium is deposited. Intuitively, calcium may interact strongly with the polymer substrate, or it may not. If there is a strong interaction, it may be due to calcium acting as a dopant to the polymer much like in conventional semiconductors, or it may be due to calcium undergoing a

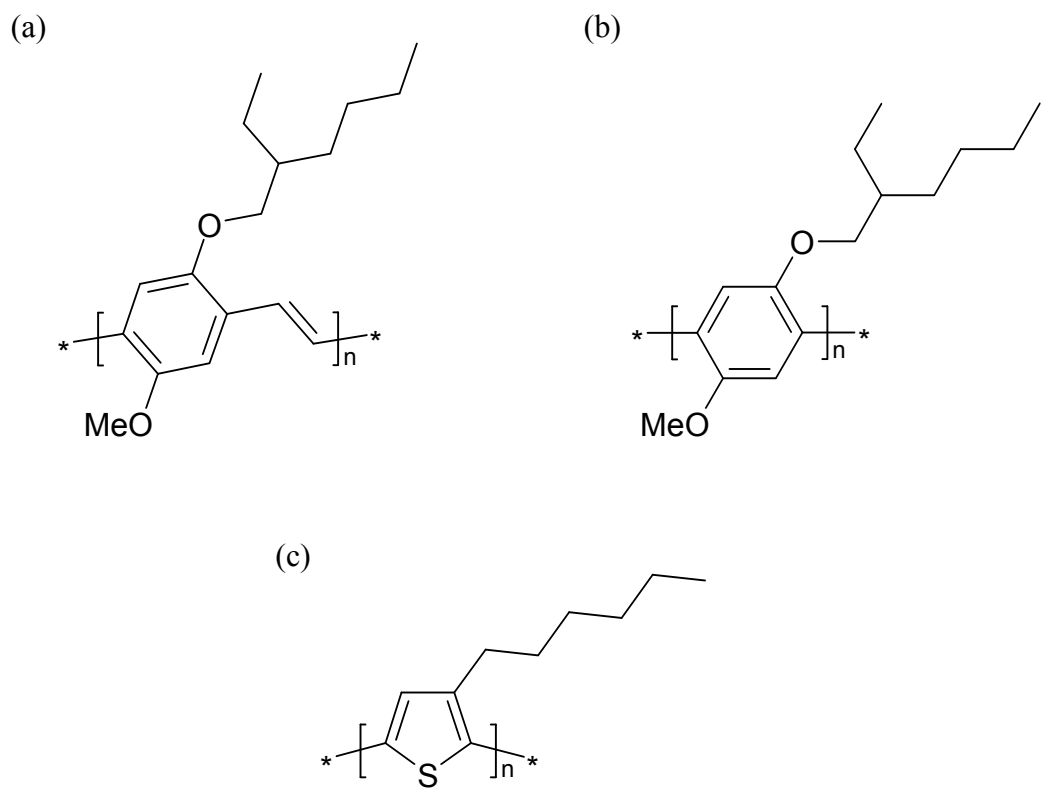


Figure 1.6: Chemical structures of the three polymers studied in this thesis

(a) MEH-PPV, (b) MEH-PPP, (c) P3HT.

chemical reaction with the polymer substrate. This reaction then may be due to calcium reacting with impurities in the polymer substrates, or with the polymer chains themselves, which may take place at functional groups on the side groups, or at the conjugated backbone. If calcium does not interact strongly with the polymer substrate, it may form a metallic overlayer with a sharp interface, or it may diffuse into the polymer, which can either occur to a limited extent such that the unreacted calcium stays close to the surface, or it may diffuse deep into the polymer layer. These ideas will be further discussed in the next chapter with respect to each of the polymers studied.

2. Calcium Chemistry

2.1. Ionic Species

In order to understand the interactions between calcium and polymers, it is instructive to have an understanding of general calcium chemistry. Calcium is an alkali earth metal, thus it readily gives up its 2 valence electrons to form ionic compounds.

Calcium can form different compounds with oxygen. One oxygen-containing compound is calcium oxide CaO , a white ionic solid with a standard heat of formation of -634.9 kJ/mol.²⁶ Another compound involving oxygen and calcium is calcium peroxide CaO_2 , which is thermodynamically unstable towards decomposition into CaO and oxygen gas. This compound is not well characterized, due partly to it always having traces of water or hydrogen peroxide trapped in the crystal lattice from synthesis, and partly to its instability toward decomposition. The standard heat of the aforementioned decomposition of CaO_2 to CaO and oxygen gas has been calculated to be -23.5 kJ/mol,²⁷ thus yielding a standard heat of formation of -611.4 kJ/mol for calcium peroxide. This reaction, however, occurs slowly, CaO_2 is therefore used as an oxygen releasing source in agriculture.²⁸

Calcium reacts with water to form calcium hydroxide $\text{Ca}(\text{OH})_2$, which has a standard heat of formation of -985.2 kJ/mol.²⁶ $\text{Ca}(\text{OH})_2$ is thus thermodynamically more stable than calcium oxide (standard heat of formation for water is -286 kJ/mol),²⁶ but can be converted to the latter by heating. Calcium also reacts with sulphur to form calcium sulphide CaS . This compound has a standard heat of formation of -482.4 kJ/mol,²⁶ which is less exothermic than that of CaO .

2.2. Organometallic Species

While calcium is more commonly known to form almost purely ionic compounds, it can also form molecular organometallic compounds. The most important family of these calcium compounds is calcocene, which consists of a Ca^{2+} cation sandwiched between 2 cyclopentadienyl C_5H_5^- (Cp^-) or related anions. Calcium can react with cyclopentadiene C_5H_6 to yield $\text{Ca}(\text{Cp})_2$, though this reaction is more facile if calcium is pre-reacted with ammonia to form calcium amide $\text{Ca}(\text{NH}_2)_2$ before reacting with cyclopentadiene.^{29,30} The structure of the compound is shown in **Figure 2.1** and **Figure 2.2**.^{29,30} Unlike the most well known sandwich compound ferrocene $\text{Fe}(\text{Cp})_2$ however, not all cyclopentadienyls are η^5 bonded to the calcium, where η^5 indicates that all 5 carbons in the Cp ring interact with the metal centre. Furthermore, the Cp rings are not 180 degrees from each other in $\text{Ca}(\text{Cp})_2$, unlike in ferrocene where the Cp rings are directly opposite to each other. Instead, being a large cation with a 1.0 Å radius compared to 0.61 Å for Fe^{2+} ,²⁶ each Ca^{2+} coordinates with 4 Cp rings. Some of these bridge across different calcium centres; as a result a three dimensional cross-linked structure is observed in the absence of solvent and impurities. This cross-linked structure is such that in the coordination sphere of each Ca^{2+} , there are 2 η^5 -bonded, 1 η^3 -bonded, and 1 η^1 -bonded cyclopentadienyls.³⁰ On the other hand, the non-cross-linked species $\text{Ca}(\text{Cp})_2(\text{THF})_2$ is known to be the product when $\text{Ca}(\text{Cp})_2$ is synthesized in THF before the solvent is driven away by heating in vacuum. Calcium cation also forms a compound with the bulkier pentamethylcyclopentadienyl anion $\text{C}_5(\text{CH}_3)_5^-$ (Cp^*). This compound does not have a cross-linked structure; instead it is a molecular compound with only 2 η^5 rings per metal centre as can be seen in **Figure 2.3**.²⁹ This phenomenon is attributed to the increased steric bulk on the ligands. Both $\text{Ca}(\text{Cp})_2$ and $\text{Ca}(\text{Cp}^*)_2$ readily react with Lewis bases, including solvent molecules, where the bases form dative bonds with the calcium center. When this happens, $\text{Ca}(\text{Cp})_2$ loses its cross-linked structure and becomes molecular, just as in the case of THF mentioned above.

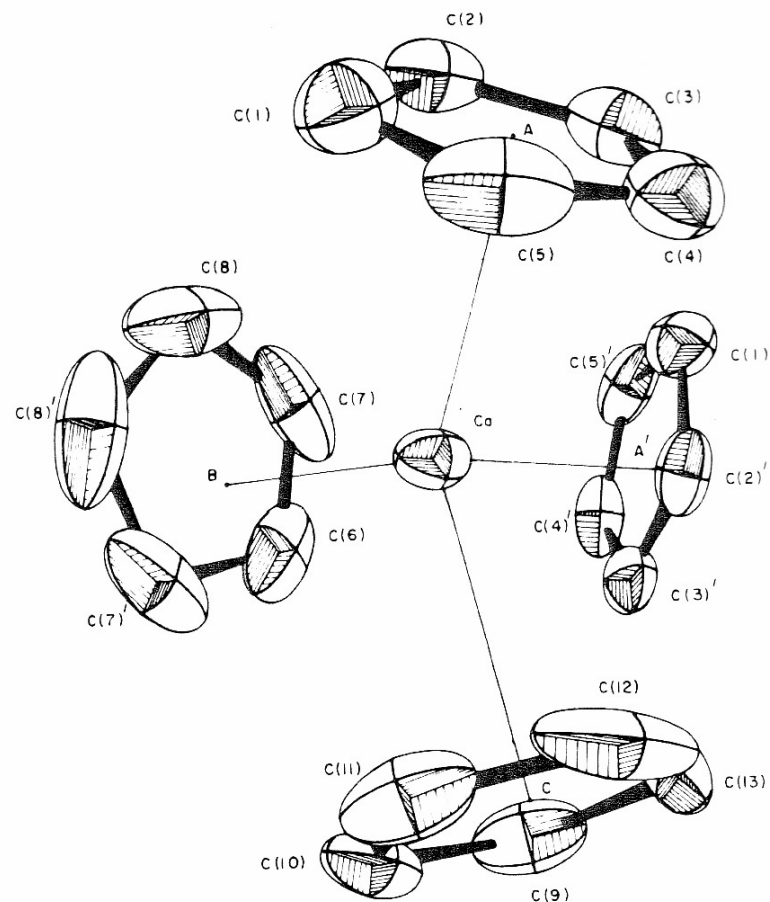


Figure 2.1: Structure of $\text{Ca}(\text{Cp})_2$

There are four rings in the coordination sphere of each calcium atom: rings A and C are η^5 -bonded to calcium, ring B is η^3 -bonded, while ring A' is η^1 -bonded. These rings can also interact with other calcium atoms to act as bridging ligands. (Reprinted from *J. Organomet. Chem.*, **80**, R. Zerger, and G. Stucky, Unsaturated organometallic compounds of the main group elements. Dicyclopentadienylcalcium, 7-17, Copyright 1974, with permission from Elsevier)

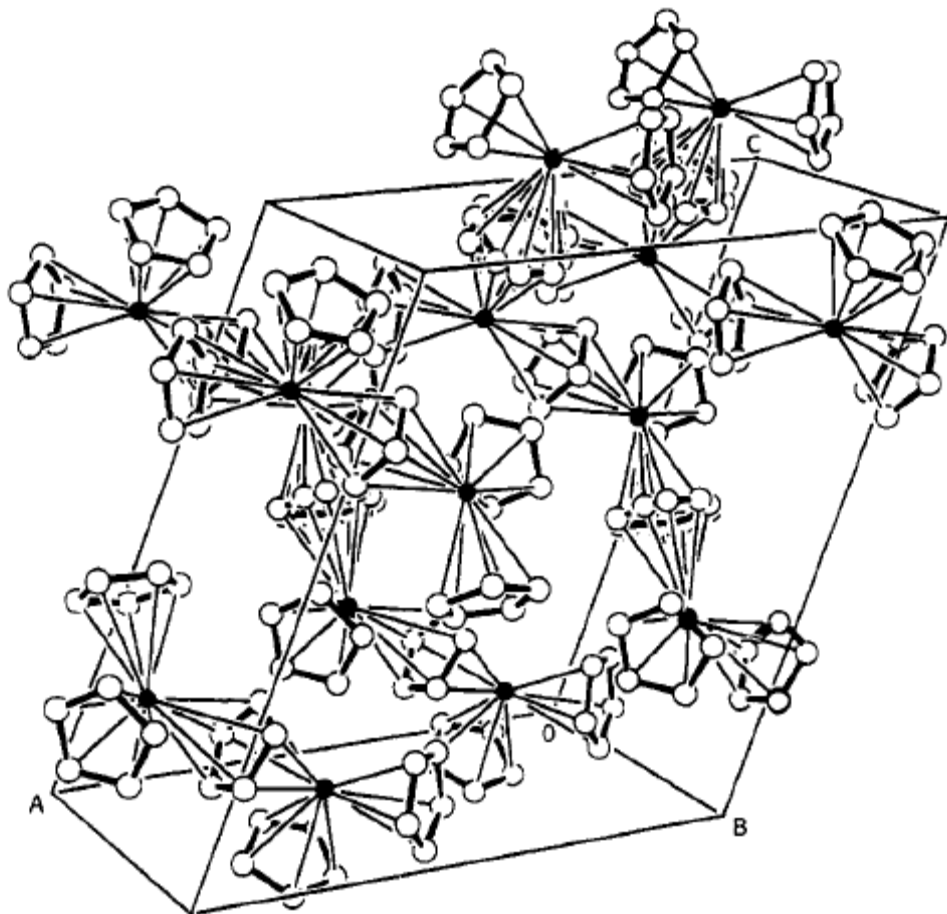


Figure 2.2: Structure of $\text{Ca}(\text{Cp})_2$

While this figure is not clear in indicating exactly what the interactions are between calcium and cyclopentadienyl, it shows that some Cp rings act as bridging ligand in forming an extended cross-linked structure. (Reprinted with permission from T. P. Hanusa, *Chem. Rev.* **93** (1993) 1023.

Copyright 1993 American Chemical Society.)

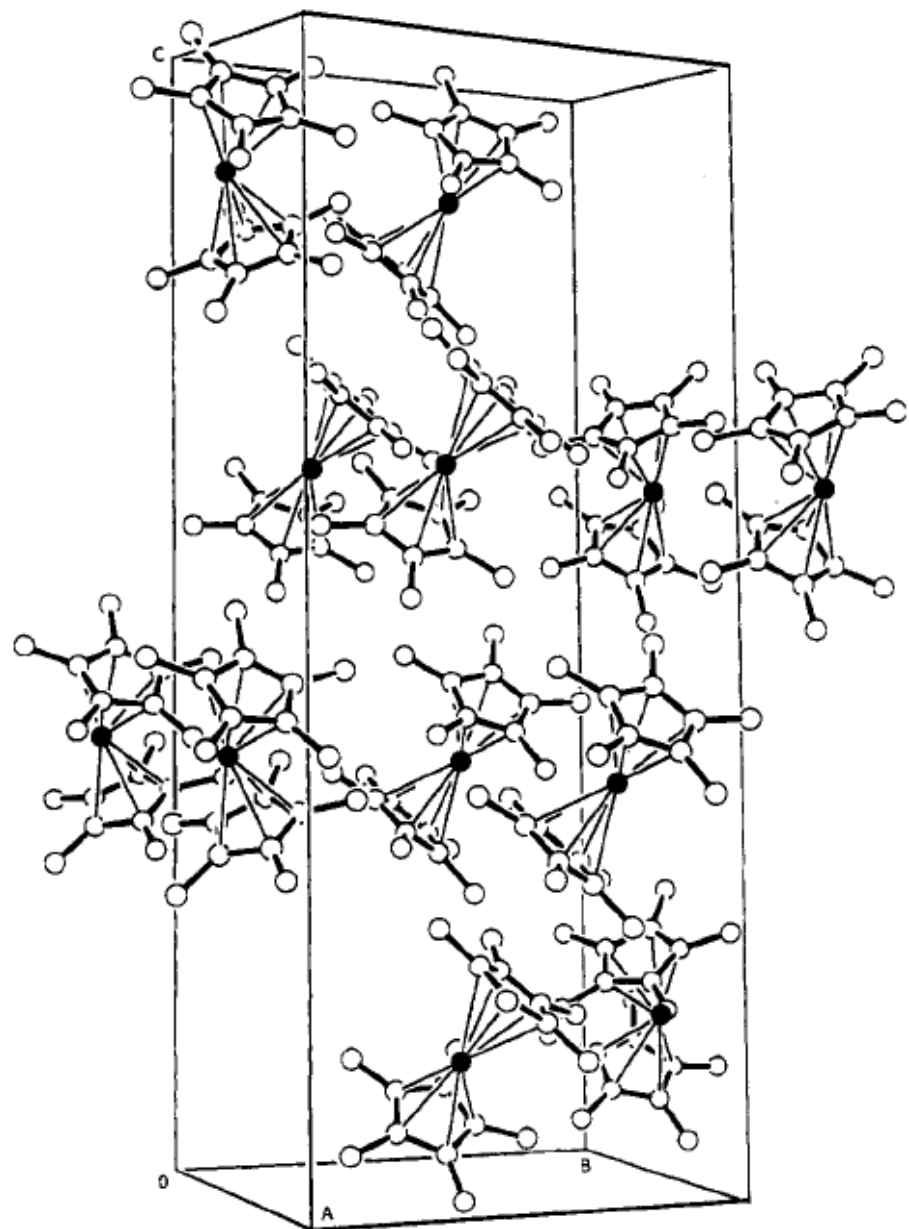


Figure 2.3: Structure of $\text{Ca}(\text{Cp}^*)_2$

Of note are the molecular nature of this compound, and that the Cp^* rings are not parallel to each other in each molecule. (Reprinted with permission from T. P. Hanusa, *Chem. Rev.* **93** (1993) 1023. Copyright 1993 American Chemical Society.)

Interactions between calcium and carbon-carbon double bonds in species unrelated to cyclopentadienyl are also possible. Examples of these are the molecular compounds $\text{Ca}(\text{CHPh}=\text{C}(\text{CH}_3)-\text{C}(\text{CH}_3)=\text{CHPh})(\text{THF})_4$, in which the unsaturated ligand is η^4 bonded to the Ca,^{31,32} and $\text{Ca}\{[\text{Si}(\text{CH}_3)_3]\text{CH}=\text{CH}-\text{CH}[\text{Si}(\text{CH}_3)_3]\}_2(\text{THF})_2$, where the ligand is η^3 bonded.^{32,33} These two molecules are shown in **Figure 2.4** and **Figure 2.5** respectively. It should be noted that the latter compound cannot be formed by a direct reaction between Ca metal and the neutral parent ligand; instead it is formed by an exchange reaction wherein calcium halide is reacted with the ligand anion that is typically prepared by the abstraction of a hydrogen atom using a strong base.³³

Direct reaction between calcium and benzene is thought to have been achieved by the co-deposition of calcium vapour and benzene: it has been reported that the highly unstable insertion compound PhCaH forms when calcium and benzene is co-deposited at 77K, followed by the warming of the reaction vessel to room temperature.³⁴ Insertion can also occur at the alkyl groups in substituted benzenes using the same preparation method, where calcium inserts both between the alkyl and phenyl groups, as well as within the alkyl chain.³⁴

Another compound involving benzene rings and calcium is CaPh_2 , which is the proposed product in the reaction between iodobenzene and metallic calcium carried out in THF at -20°C.³⁵ The authors did not report structural information on the compound, unfortunately, nor did they indicate whether THF is also complexed in the reaction.

One last species worth mentioning is the ring-sandwich anion that calcium forms with cyclooctatetraene. $[\text{Ca}(\text{C}_8\text{H}_8)_2]^{2-}$, with K^+ as counter ions, can be prepared by the addition of cyclooctatetraene to potassium and calcium metals in ammonia at -78°C. The two rings are reported to be eclipsed, and η^8 -bonded to calcium.³⁶

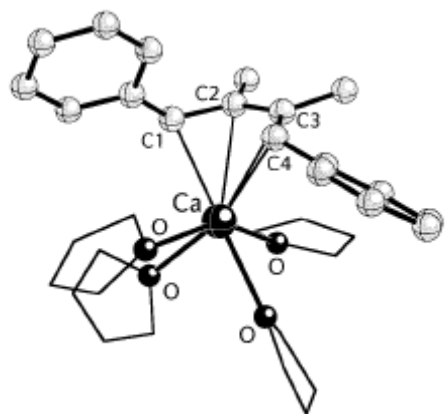


Figure 2.4: Molecular structure of $\text{Ca}(\text{CHPh}=\text{C}(\text{CH}_3)-\text{C}(\text{CH}_3)=\text{CHPh})(\text{THF})_4$

Calcium interacts with the ligand via the delocalized π -electrons that span 4 carbon atoms. (Reprinted from *Coord. Chem. Rev.*, **210**, T. P. Hanusa, Non-cyclopentadienyl organometallic compounds of calcium, strontium and barium, 329-367, Copyright 2000, with permission from Elsevier.)

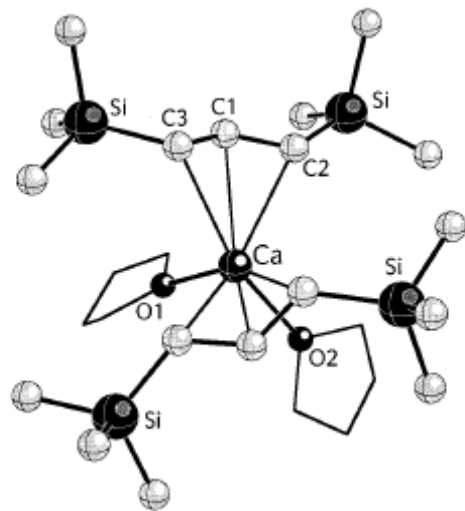


Figure 2.5: Molecular structure of $\text{Ca}\{[\text{Si}(\text{CH}_3)_3]\text{CH}=\text{CH}-\text{CH}[\text{Si}(\text{CH}_3)_3]\}_2(\text{THF})_2$.
Calcium cation interacts with the ligands via the delocalized π -electrons spanning three carbon atoms. (Reprinted from *Coord. Chem. Rev.*, 210, T. P. Hanusa, Non-cyclopentadienyl organometallic compounds of calcium, strontium and barium, 329-367, Copyright 2000, with permission from Elsevier.)

2.3. Interactions with Semiconducting Polymers

Polymeric semiconductors have been studied predominantly by researchers interested in fabricating electronic devices. As a result, instead of chemistry, they are often focused on physical electronic descriptions in terms of band structures, where polarons and bipolarons form when the semiconductor is doped.^{37,38} These new polaronic energy states are formed because doping, i.e. the addition or removal of electrons from the polymer, changes the geometry of the conjugated backbone that gives rise to the narrow-gap band structure that leads to the polymer's intrinsic semiconductivity. **Figure 2.6** shows a schematic energy level diagram of the various types of common polaronic species³⁹ proposed in the literature as possible charge carriers. The new energy states lie within the band gap. Interestingly, the energy level diagrams in **Figure 2.6(b)** and **Figure 2.6(c)** appear to indicate that polaron formation is an endothermic process. The following is an explanation of this phenomenon; **Figure 2.7** is an aid to this discussion.⁴⁰

In an ionization process from the neutral ground state of the polymer, an energy corresponding to the vertical ionization energy ($E_{IP,v}$) is required to promote the system to the charged state (**Figure 2.7(a)**). This $E_{IP,v}$ corresponds to the energy of the HOMO of the undoped polymer (**Figure 2.7(b)**). Since the equilibrium geometry of the charged (doped) state is in general different from that of the ground neutral state, there is a relaxation energy (E_r) upon doping as the charged system relaxes to the new equilibrium geometry. If we then consider the de-doping of this charged ground state, an energy corresponding to $E_{IP,d}$ is gained, which is different from $E_{IP,v}$, by the sum of E_r and E_d , the latter being the distortion energy of the ground state to get to the geometry of the doped state. Thus, when a polaron is formed, the HOMO shifts higher in energy into the band gap by the sum of E_r and E_d , with a corresponding shift in the opposite direction for LUMO.⁴⁰ Note that the same argument applies to the further shifting of the energy levels when bipolarons are

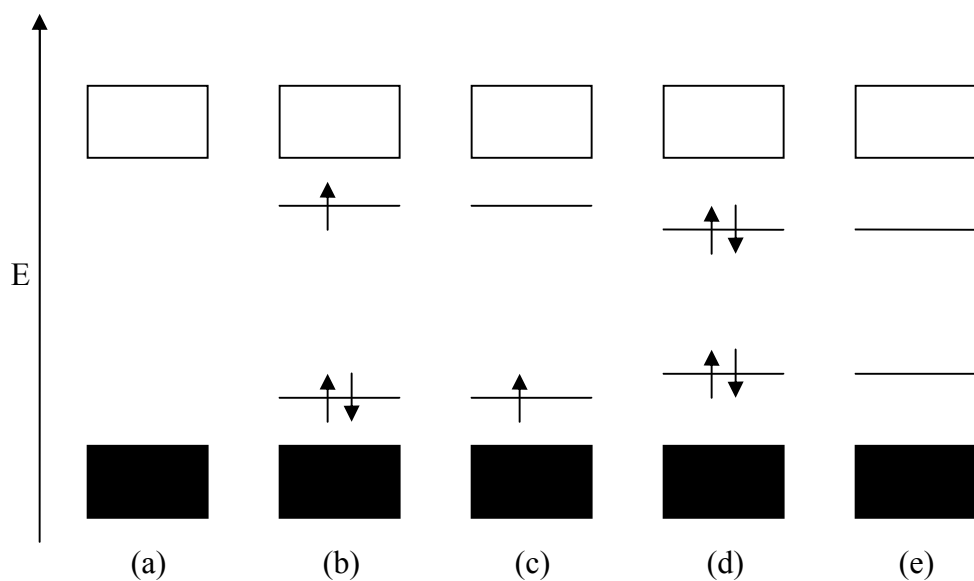


Figure 2.6: Schematic energy diagram of common species in the doping of semiconducting polymers

The empty boxes represent the empty conduction band, while the filled ones represent the occupied valence band. The diagrams represent the following species: (a) undoped, (b) negative polaron, (c) positive polaron, (d) negative bipolaron, (e) positive bipolaron.

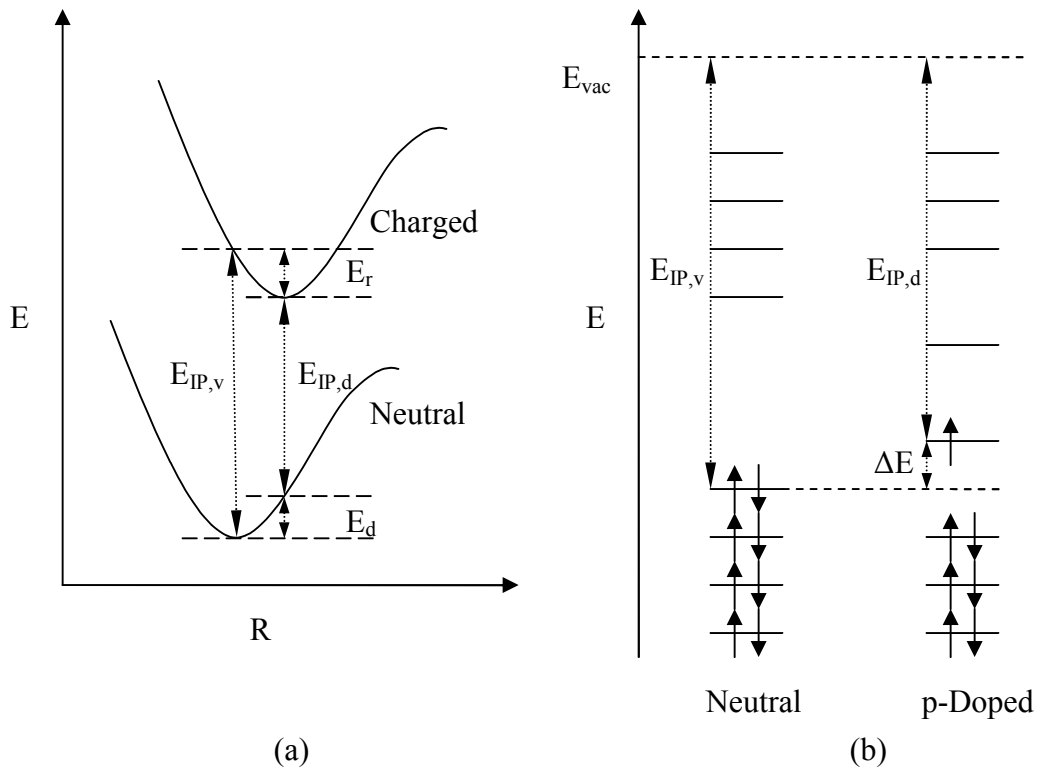


Figure 2.7: Diagrams for explaining the energies of polaronic levels

(a) Schematic diagram of the energy surfaces of neutral and charged species. The R axis designates atomic distances. $E_{IP,v}$ is the vertical ionization energy, $E_{IP,d}$ is the ionization energy of the distorted species, E_r is the relaxation energy, and E_d is the distortion energy. (b) Schematic energy level diagrams of the neutral and doped (charged) species at their respective equilibrium geometries. ΔE , the energy shift of the polaronic state from the HOMO of the undoped polymer, corresponds to the sum of E_r and E_d in (a).

formed.

Using PPV as an example, **Figure 2.8** demonstrates the proposed geometry of polarons and bipolarons.^{40,41} The quinoid geometry, as adopted by the negative polaron shown in **Figure 2.8(b)**, is higher in energy than the benzoid geometry of the undoped polymer; thus **Figure 2.8** demonstrates chemically why a polaron should be destabilized compared to the pristine polymer. This figure also demonstrates why a bipolaron should be energetically more stable than 2 independent polarons: since the formation of a polaron requires a change in the entire conjugated length from where the charge is located, whereas in a bipolaron there is a change only in the segment between the charges, less energy is required for its formation.

From a chemist's perspective, one desires an understanding of polymer doping by the calcium in terms of chemical bond formation. In previous sections different types of chemical interactions between calcium and various molecular species have been discussed; what about interactions with polymers? One possible type of interaction between calcium and polymer is a redox reaction involving the entire conjugated polymer backbone. This could be a favourable reaction, since the extended conjugated backbone of these polymers should be able to accommodate negative charges readily, which can lead to interactions analogous to high- η interactions seen in conjugated molecules. Analogous to calcacene compounds, another possible type of reaction involves calcium bridging either different parts of a single polymer chain, or bridging across chains. The extent of these reactions would depend strongly on the geometry of the polymer chains, which in turn depends strongly on the side groups. Of course, calcium can also interact not with the polymer backbone but with the side groups instead. Clearly there cannot be a blanket statement about the interaction of calcium with different polymers; the following is a brief survey of literature information on the three polymers studied in this thesis.

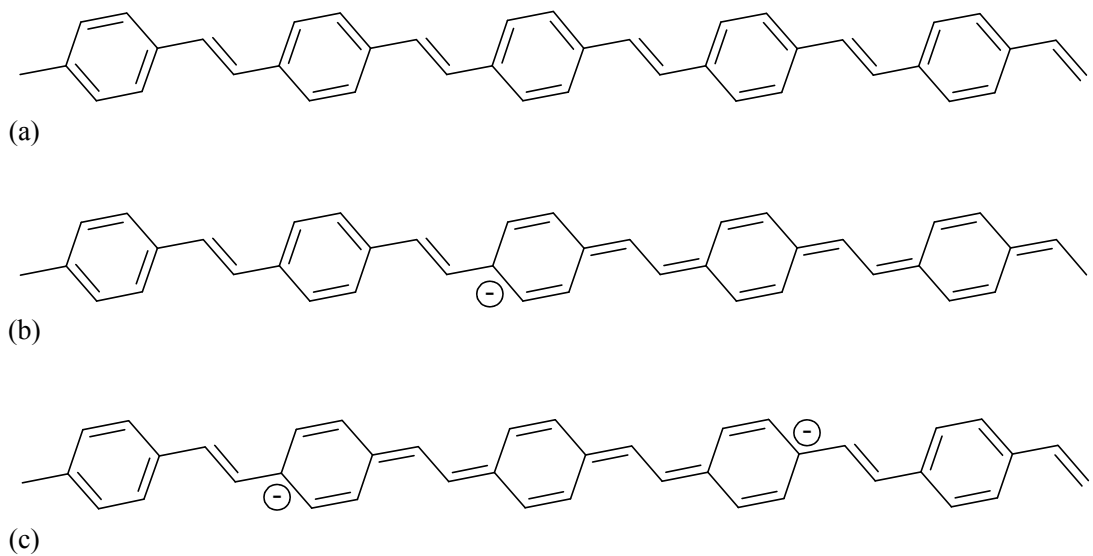


Figure 2.8: Chemical picture of polarons using PPV as a model

(a) neutral, (b) negative polaron, (c) negative bipolaron. Note in this picture the quinoid form is adopted when a polaron is formed.

2.3.1. MEH-PPV

There are conflicting conclusions in the literature about the interaction between calcium and MEH-PPV. Some researchers report that polarons/bipolarons form when calcium is deposited onto PPV-type polymers.^{42,43} These studies are usually done using x-ray photoelectron spectroscopy (XPS) and/or ultraviolet photoelectron spectroscopy (UPS). In XPS, where core electrons are investigated, new calcium peaks attributed to Ca²⁺ can be seen to grow in as calcium is deposited, while in UPS, where valence electrons are probed, new peaks that arise inside the band gap have been concluded to be due to the formation of polarons/bipolarons. These spectroscopic studies do not include discussion of the localized bonding structure of the calcium. It has been suggested through theoretical studies that the calcium interacts with the vinylene double bond, forming new electronic states within the band gap, consistent with the formation of polarons/bipolarons.⁴⁴ In this picture calcium is calculated to be located at the vinylene carbons, with electrons transferred onto the conjugated backbone, forming delocalized new states.

Contrary to those who suggest calcium reacts via charge transfer into the conjugated backbone of the polymer, some researchers find that calcium interacts with the vinylene double bond to form localized carbide bonds between the carbons and the calcium centre.⁴⁵ Here it is proposed that calcium bonds formally with both of the vinylene carbons to form a 3-membered ring, as evidenced by fragments with a mass-to-charge ratio of 65, assigned to the cation [CaC₂H]⁺, seen in the secondary ion mass spectrometry (SIMS) spectra, together with changes in carbon XPS signals corresponding to C-C, O-C, and C-O-C environments when the interface is exposed to oxygen.

Some researchers contend that while calcium reacts with the polymer substrate, no calcium polymer complex is formed.⁴⁶ In this picture calcium oxide is said to form at the surface of the polymer via two possible mechanisms. The first is that calcium

breaks alkoxy bonds and extracts oxygen atoms, while the other is that calcium reacts with oxygen impurities embedded in the polymer substrate near the surface. These conclusions have been drawn through XPS studies where the authors argue that the growth of a narrow new oxygen peak, as well as the way oxygen and calcium signals change during the course of deposition, indicate the formation of a crystalline compound.

2.3.2. MEH-PPP

Information is scarce about MEH-PPP in the literature: it appears that this polymer has only been studied purely in terms of suitability as a candidate for device fabrication, such that only device performance data is available but not chemical details. p-Sexiphenyl (6P), an oligomer of the unsubstituted PPP backbone with six repeat units, is concluded to form polarons and bipolarons in the presence of sodium, since the observed Raman spectra closely resemble the calculated spectra of the anion and dianion using DFT.⁴⁷ Based on the result for 6P as well as other oligomers of PPP, the authors contend that the Raman spectra of unsubstituted PPP can also be adequately explained by the formation of polarons and bipolarons through doping by sodium.^{48,49}

Calcium, on the other hand, is argued in one study to induce bipolarons in 6P from the very beginning of deposition, as opposed to the usual formation of polarons followed by the coalescence into bipolarons.⁵⁰ The authors draw this conclusion by a peak shape argument of the intra-gap state seen in the UPS spectra. They argue that if bipolaron formation was stepwise, the peak shape should change with deposition since a peak component should first grow in and then decay while a second component appears. Instead, they observe no peak shape change in their experiments.

2.3.3. P3HT

Information about the interaction between P3HT and calcium is also scarce. In a study of a copolymer with alternating phenylenevinylene and thiophene monomer units, it has been reported that calcium reacts primarily with the sulphur atom.⁵¹ This is argued by the growth of a new sulphur peak in XPS. The authors have not suggested what the chemical structure might be when calcium reacts with sulphur centres, only that the XPS peak corresponds to a Ca-S bond. The authors also suggest that a smaller fraction of calcium dopes the polymer by a parallel competing mechanism, as seen in the growth of new signals in the carbon XPS peak and the smearing of the HOMO-derived peak in UPS.

A few studies have been done on the oligomer α -sexithiophene (α 6T). Some researchers conclude that while it is possible to describe the interaction between sodium and α 6T in terms of doping, where polarons, followed by bipolarons form as coverage increases, it is more appropriate to describe the interaction as sodium reacting with sulphur centres by transferring its electron to S, since a low conductivity is measured when sodium is present.⁵² In another study where sodium is deposited on P3HT, the authors contend that sodium reduces and abstracts sulphur from the polymer, breaking apart the thiophene ring to form sodium sulphide in the process, which makes n-doping of the polymer in the conventional sense impossible.⁵³ They base their argument on the formation of an XPS signal that can be assigned to sulphur in a reduced state, along with the decay of the thiophene sulphur signal. Contrary to this study, it has also been reported that potassium, an alkali metal like sodium, n-dopes polythiophene instead of forming localized bonds with the sulphur atoms: polarons, followed by bipolarons, can be observed by the growth of intra-gap states in UPS.⁵⁴

In studies on the aluminum/polythiophene system, aluminum is argued to bond to thiophene rings in the α -positions (atoms that are immediately next to the sulphur in the ring), thus localizing the former π -electrons into strong Al-C bonds and disrupting

the conjugated backbone in the process.^{55,56} Hartree-Fock calculations have been done in these studies using a model where aluminum dimers (chosen such that a closed-shell system is obtained for ease of calculation) interacts with the polymer. Within this framework, electron density between the Al centres in the dimer is transferred to the resultant Al-C bonds. It is noteworthy that according to these calculations, an electron-rich sulphur XPS signal does not necessarily imply atom abstraction and formation of metal sulphide.

3. Experimental

3.1. Apparatus

While adsorption calorimetry has a long history in surface science studies,⁵⁷ the need to study reactions involving small sample sizes, thus small amounts of heat, has been the drive to further refine this age-old technique. In one of the earlier designs of the modern ultra-high vacuum (UHV) microcalorimeters designed by D.A. King, the temperature measurement is done remotely by a broadband infrared photon detector viewing the back side of the substrate.^{58,59} The substrates for this apparatus are mostly thin film single crystals of epitaxially grown metals. The next major update to UHV microcalorimeters is by C. T. Campbell, which has a heat detection system that is based on a pyroelectric ribbon of β -polyvinylidene fluoride placed in contact with the substrates.⁶⁰ The pyroelectric material acts as a heat detector by producing an electrical signal when there is a change in heat input. This phenomenon arises from the material's crystal structure, which is polar. At equilibrium, charges accumulate at the surfaces through internal conduction (albeit limited) or other ambient sources such that the intrinsic dipole of the crystal is neutralized. However, when it is perturbed, be it by mechanical means or by heating, the crystal's dipole changes. If an external circuit is present connecting the surfaces corresponding to the two ends of the dipole, this change would induce a flow of charges as the equilibrium is being re-established. This charge flow can be measured as a voltage, thus yielding the electrical signal needed for the material's use as a heat detector.⁶¹

The use of pyroelectric materials in direct contact to the system being studied is clearly a better heat detection method than a remote photon counter, especially since considerable precautions need to be taken to minimize stray photons unrelated to the system studied in the latter method. However, the somewhat cumbersome assembly

required for the ribbon pyroelectric detector, makes it difficult to achieve a good thermal contact between the detector and sample.

Taking advantage of the low treatment temperature required for polymer surfaces compared to metallic crystalline surfaces, a novel apparatus specially adapted for studying polymer metallization was designed in our group. A disc made of a pyroelectric material was used as the substrate for the polymer, as well as being the heat detector. This pyroelectric is of a ceramic type, able to withstand polymer degassing temperatures without losing polarization.

A schematic diagram of this unique UHV microcalorimeter is presented in **Figure 3.1**. The sensor assembly was built around a pyroelectric lithium tantalate (LiTaO_3) crystal disk with the crystal's dipole normal to the circular surfaces (Marketech International, z-cut, 10 or 11 mm diameter, 0.5 mm thickness). These two surfaces were gold plated (200 nm), with chromium (10 nm) as an adhesive layer between LiTaO_3 and gold, to serve as electrodes. The polymer was spin-coated onto the crystal, which was then mounted such that contacts were made between the crystal's two faces and, respectively, the copper back electrode and the mounting stub. **Figure 3.2** is a schematic diagram of this sensor assembly.

The calorimeter consisted of two chambers separated by a gate valve: a main chamber for carrying out metal deposition and measurements, and a preparation chamber for curing and/or degassing of the sample. A base pressure on the order of 10^{-10} torr was achieved by a turbomolecular pump (Varian V-250), backed by a rotary vane roughing pump at the preparation chamber, and three ion pumps at the main chamber (Thermionics IP-200 outside of the effusion cell section and two Thermionics IP-020 pumps at the effusion cell section).

Calcium deposition was carried out via an atom beam generated from an effusion cell (Applied EPI) containing a 10 cm^3 tungsten crucible with calcium granules in an

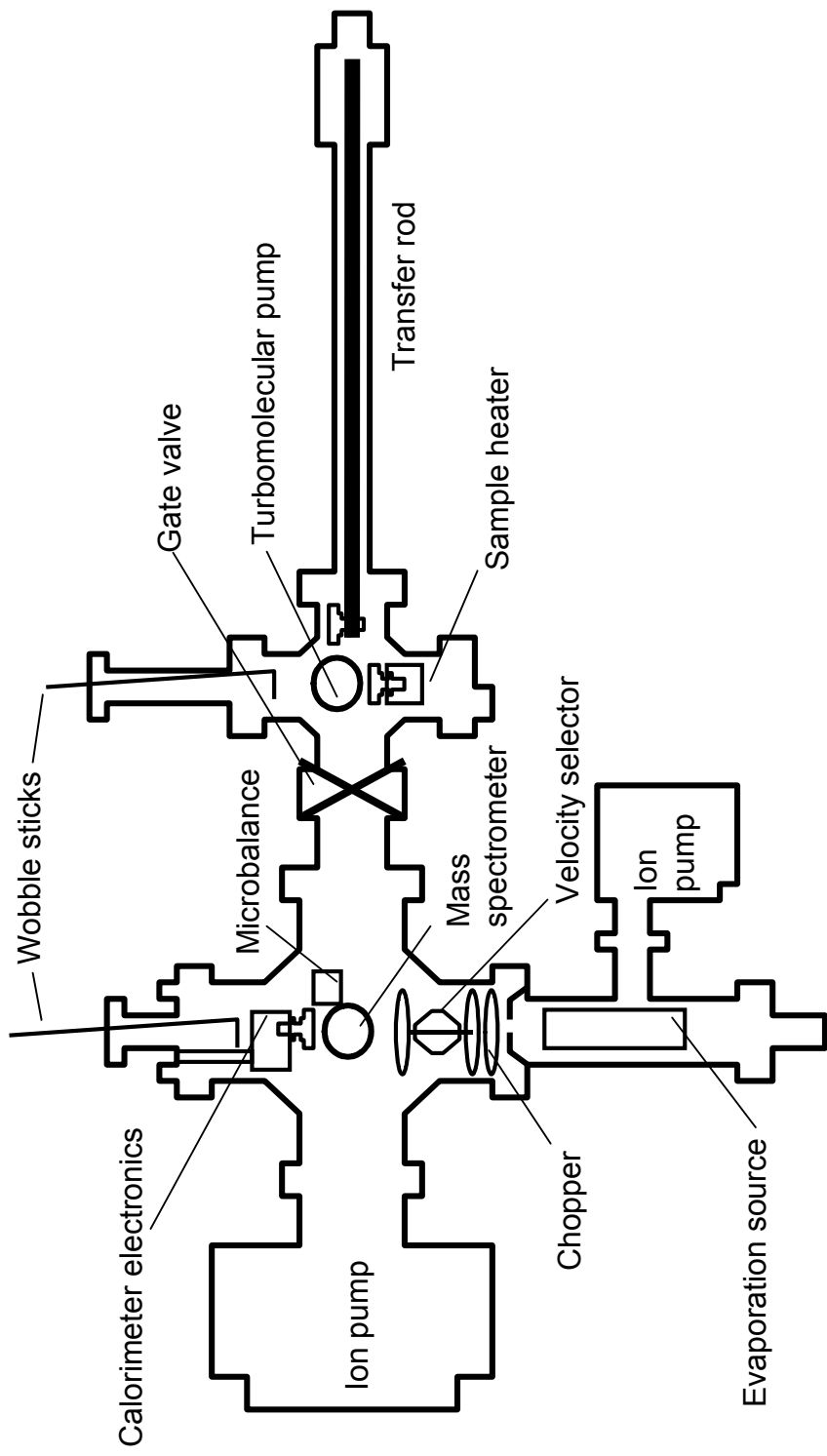


Figure 3.1: Schematic diagram of our UHV calorimeter

A gate valve separates the main calorimetry chamber on the left from the sample preparation chamber on the right, such

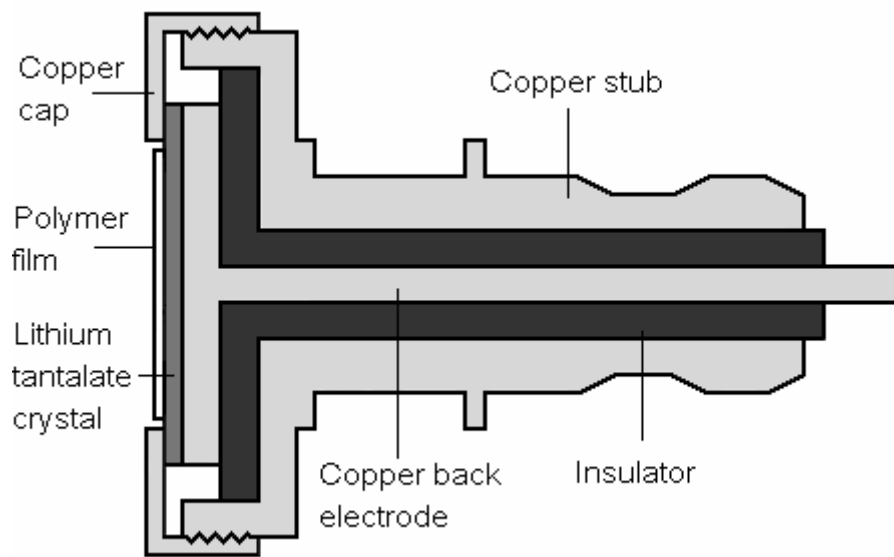


Figure 3.2: Schematic diagram of the sensor assembly

The cap is screwed onto the mounting stub such that the entire casing acted as an electrode, in contact with the front face of the pyroelectric crystal. The back face is in contact with a second electrode along the centre of the stub.

alumina liner (Ozark Technical Ceramics). The effusion cell was surrounded by a custom water jacket made of stainless steel.

The pyroelectric heat detector responded to changes in heat input; experiments were therefore carried out using a pulsed calcium metal beam, such that voltage pulses were obtained as a function of time. The heights of these voltage signals were proportional to the amount of heat generated when calcium arrived at the polymer. The metal atoms from the cell first passed through a 4 mm-wide slit, followed by an externally driven chopper wheel with a single 60° notch. This yielded the pulsed metal beam necessary for the pyroelectric heat detection system, with a duty factor of 1/6. The last item the atoms had to pass through before reaching the sample assembly was the velocity selector, which was first and foremost designed as a photon block to minimize background signal due to the high temperature effusion cell. It was comprised of 2 staggered multi-notched chopper blades, such that at any given time there was no direct line of sight between the effusion cell and the detector.^{62,63} These blades were mounted on a single drive shaft and were driven by a high speed motor mounted inside the vacuum chamber. When the motor spun at a “slow” speed of 44 revolutions per second, atom transmission was essentially zero. However, at higher speeds, atom transmission was appreciable; thus the velocity selector acted also as a shutter for the metal atom beam as well as being a photon block.

The main chamber is equipped with a quadrupole mass spectrometer, which is used to perform residual gas analysis on the quality of the vacuum achieved in the calorimeter. It is also equipped with a quartz crystal microbalance (Inficon XTM/2) to monitor metal atom flux. The sample holder houses the calorimeter electronics: a field-effect transistor-based voltage follower acting as a preamplifier that also lowers the impedance to reduce the possibility of noise pickup. Final voltage amplification is carried out outside the chamber.

The resulting signal is monitored and logged by a computer with a data acquisition and control card (National Instrument AT-MIO-16XE-50 initially, which was then replaced by National Instrument PCI-6052E). The computer is also used to drive and synchronize the chopper wheel and the velocity selector with data acquisition, using a LabView programming environment.

3.2. Experimental Details

The calcium granules used in these experiments were purchased from Alfa Aesar (99.5%), and was used directly from the bottle without any treatment as appears to be common practice given the lack of documented treatments in most OLED studies involving calcium deposition.^{64,65,66} Degassing was done at around 770 K, which is about 100 K higher than the normal operating temperature. This drives off volatile contaminants, while reaction products between calcium and air such as oxides and hydroxides, which are non-volatile at this temperature, will stay behind at the crucible during deposition. Attempts to cleanse the calcium by dilute acid rinse followed by transfer under cyclohexane⁶⁷ yielded no appreciable difference in the amount of time needed to sufficiently degas the calcium to reach operating pressure, nor did it yield a significant difference in the composition of the background residual gas, which was principally hydrogen, with water, nitrogen, carbon monoxide and carbon dioxide also present, but reduced to trace amounts after degassing. The pressure of the vacuum chamber with the metal source at operating temperature is in the high 10^{-8} to low 10^{-7} torr range.

MEH-PPV was obtained from American Dye Source (ADS100RE), as well as MEH-PPP (ADS256BE), while P3HT was obtained from Aldrich (510823). Polymer spin-coating was done at 1500 revolutions per minute (rpm) using THF solutions with a concentration of 1 g/mL. After the polymer was spin-coated, the sensor assembly was placed in the heating dock at the preparation stage for degassing and annealing at a temperature of 375 K for 3 hours in vacuum. It was then allowed to return to room temperature, before being transferred into the main calorimetry chamber. In experiments studying the effects of oxygen embedded in polymer films, 1 atm of pure oxygen gas was introduced, in the dark, to the sample after the aforementioned degassing/annealing process. The sample was exposed to the oxygen atmosphere for 20 minutes before it was returned to UHV conditions.

Calorimetry experiments were carried out with the beam chopper operating at 234 rpm, thus generating 234 peak-shaped voltage signals per minute. The instantaneous calcium deposition rate was between 0.05 and 0.15 Å/s at the sample, measured with an open beam chopper. The detector voltage signal was digitized at a rate of 2340 Hz, such that each peaked-shaped voltage signal that corresponds to a pulse of calcium atoms is composed of 600 data points. **Figure 3.3** demonstrates what this voltage data looks like. Typically, data for 1000 pulses of calcium atoms were collected with the velocity selector operating at the low speed setting (44 Hz) such that metal flux was effectively blocked, followed by 2000 pulses at the high speed setting (173 Hz) where calcium atoms were allowed to pass through. This was then repeated until the desired amount of calcium was deposited.

While there was no direct line of sight between the effusion cell and the heat detector, there were nevertheless scattered photons that could find their way to the detector. The amount of stray photons that the detector saw depended on the position of the chopper wheel used to generate the pulsed metal beam: the chopper wheel was in close proximity (~5mm) to the slit from which the calcium atoms exited the effusion source, such that there was a significant difference in the amount of photons that were allowed into the main chamber between when it was open and closed. Thus, the data collected at the low speed setting measured the effusion cell thermal radiation that was allowed into the main chamber that was subsequently scattered onto the sample. This was then subtracted from the high speed data to yield voltage peak heights due to reactions. While this correction was more significant in experiments carried out previously in our group where the effusion source was operated at temperatures upward of 1500K, it was nevertheless around 5-10% of the total voltage signal height at the low deposition temperatures of 670K in these calcium experiments.

During data analyses blocks of 100 pulses are averaged in order to improve signal to noise ratio. This lowers the coverage resolution, but since each pulse corresponds to the deposition of a minute amount of calcium of between $\sim 2.0 \times 10^{-4}$ to $\sim 6.5 \times 10^{-4}$ Å,

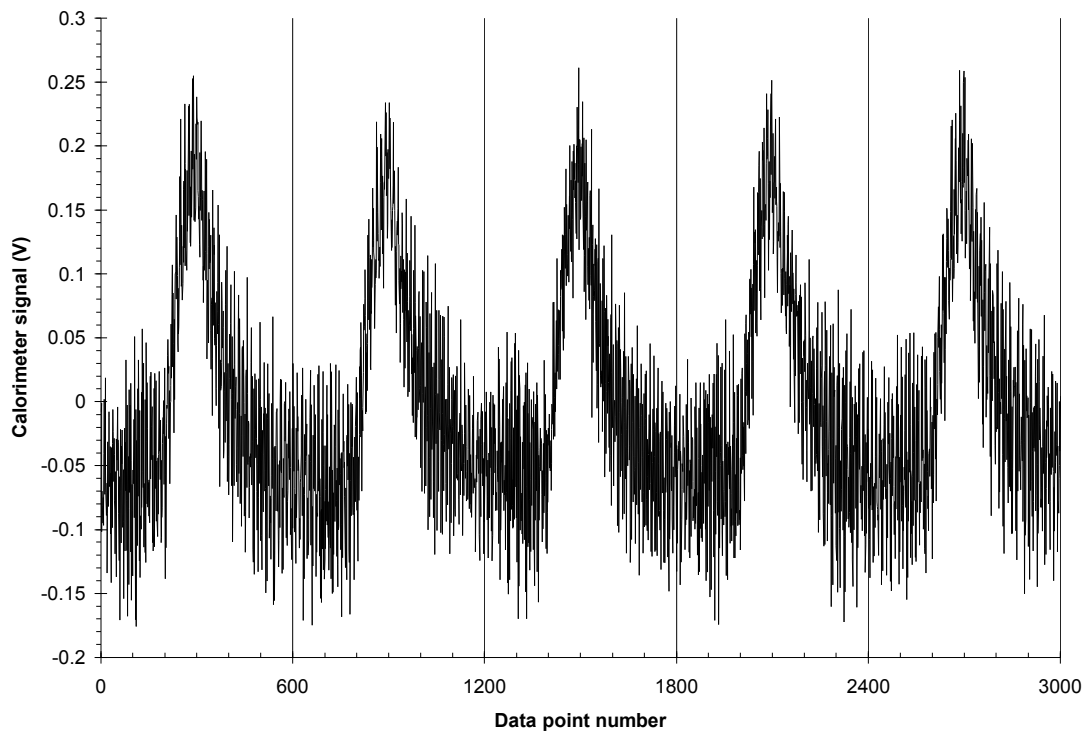


Figure 3.3: Typical voltage data collected during calorimetry experiments

Shown in this figure are 5 consecutive pulses of calcium atoms that are allowed to reach the sample, as generated by the 1/6 duty factor chopper. Each of the pulses is composed of 600 data points. Note that the horizontal axis is effectively time.

or ~ 0.005 to ~ 0.015 atoms/nm², the coverage resolution after this averaging is still exceptionally good. The pulse shapes are still rather noisy after this averaging, thus each averaged pulse is further smoothed by applying a running average: for each of the 600 data points that make up a pulse shape, 40 surrounding points are averaged together, before the peak heights are determined and shown as the results in subsequent chapters. A comparison between the raw data, averaged data, and smoothed averaged data is shown in **Figure 3.4**.

Calibration of the calorimeter was made using a 671 nm laser diode of known power. The absorbance of the bare sensor crystal at this wavelength was first measured using an integrating sphere *ex situ*. An experiment was then carried out where the laser beam from the diode was directed onto the detector assembly put together using this sensor crystal, during which the laser was pulsed at the same frequency and duty factor as the calcium metal beam in calorimetry experiments. The voltage signal due to heating by the laser was measured. Since the absorbance was already measured, the amount of energy absorbed by the sensor could be calculated, which was then used to yield a sensitivity factor that correlated the voltage signal peak height to input energy.

This sensitivity factor is used during data analysis to convert the measured voltage peak heights to the energy released when pulses of calcium reach the sample.

Together with flux measurements from the quartz crystal microbalance, the heat measured can be reported in the conventional kJ per mole of calcium. However, due to the design geometry of the velocity selector, there is a non-uniform deposition profile, as could be seen in Auger electron spectroscopy (AES), which introduces a systematic shift in the microbalance's readings.⁶³ One possible solution to this problem is to assume that the reaction between incoming calcium and the substrate after a large amount of deposition is the condensation of calcium onto calcium, such that the heat of reaction corresponds to that of calcium's tabulated condensation enthalpy of -178 kJ/mol.²⁶ To check the validity of this assumption, we measured the

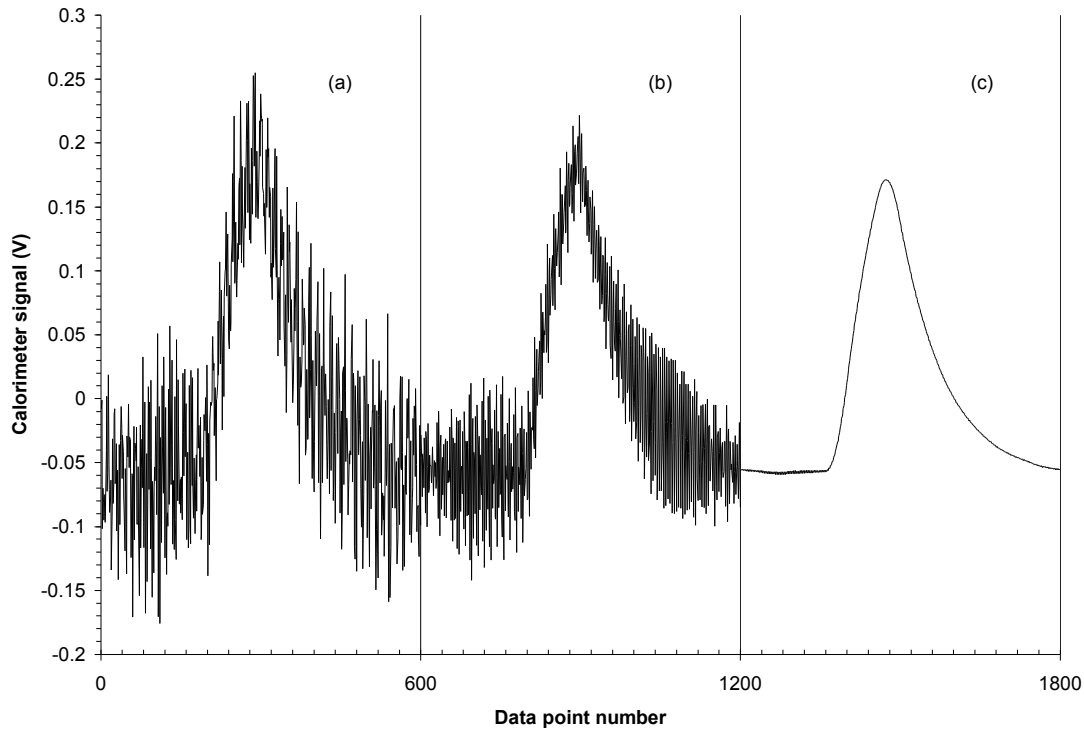


Figure 3.4: Peak shape after manipulation of raw voltage data

(a) Raw data as shown in **Figure 3.3**; (b) Averaging of 100 pulses; (c) Averaging of 40 neighbouring data points from the 100-pulse average as shown in (b). Note that the horizontal axis is effectively time.

reaction heat when calcium was deposited onto a thick film of calcium without the velocity selector in place such that the microbalance reading was reliable. The measured heat was in agreement with the calcium condensation energy. As well, another calorimetry experiment involving calcium and a polymer by another research group has been found to yield calcium's condensation energy at high coverages.⁶⁸ It thus appeared that the reaction heat at high calcium coverage could be used as an internal standard for calibrating flux measurements.

With the velocity selector in place, measured fluxes were between 1.5 and 2.5 times those determined using the internal standard at high coverage. This correction factor varied especially after the replenishment of calcium in the effusion cell. Since a precise alignment of the calcium beam was very difficult for our calorimeter, the geometry must be slightly altered every time a new load of calcium was placed into the effusion cell, which may be the reason for the varying correction factor. Nevertheless, a calibration of the microbalance by measuring the deposited calcium overlayer thickness using Auger electron spectroscopy yielded a correction factor of 1.85, which is in reasonable agreement with those suggested in the calorimetry data.

Optical experiments were also carried out, taking advantage of the pyroelectric's sensitivity to heat due to absorbed light. These experiments explored the possibility of using the calorimeter as a novel optical spectrometer. Two types of experiments were carried out: one where a diode laser was used, and the other where a xenon lamp was used. In both cases light was directed into the main chamber through a view port, which was then directed to the sample by a mirror mounted at the tip of the transfer rod that was used for moving the sample between main and preparation stages. As well, the velocity selector was removed to eliminate the calcium deposition gradient that would otherwise be difficult to account for without the internal reference as in the calorimetry experiments. This did not adversely affect optical experiments, since a photon block was unnecessary here: the chopper wheel used in the generation of the pulsed calcium beam can simply be stopped when the signal due to the pulsed laser

was collected. As a side benefit, the absence of this rapidly spinning component reduced noise due to vibration.

In the laser experiments, wavelength of 671 nm from a diode laser was used, as they are readily available and have a photon energy just below the band gap of pristine PPV and P3HT, in the region where new band edge states might form. The laser light was chopped to match the repetition rate and duty cycle of the chopped metal beam in calorimetry experiments. The laser intensity was attenuated using neutral density filters to give signal strengths approximating those seen in calorimetry to prevent overloading of the calorimeter electronics, and also as a precaution to avoid affecting the polymers. As well, the laser beam was defocused such that the entire sample was illuminated. Calcium was deposited stepwise using fluxes similar to those in calorimetry experiments. After the deposition of calcium, the mirror was moved into place, and 100 laser pulses were shone on the sample with the resultant voltage signals recorded. The 100 pulses in each deposition step are averaged during data analyses to yield a single data point, as described for the calorimetry data.

In the xenon lamp experiments, a 100W xenon lamp was used as the light source, with the output fed into a scanning monochromator. Photon energies ranging from 1.55 to 3.875 eV (800 to 320 nm) were scanned in 0.025 eV steps for samples before and after the deposition of 2 Å of calcium, using the same sample averaging as described previously. The light from the monochromator was directed through a chopper to achieve the same repetition rate and duty cycle as in previously discussed experiments, after which it was split into two such that a secondary beam was directed to a photodiode for light intensity monitoring. Before being directed into the vacuum chamber, the main beam was passed through two lenses for focusing and magnification such that the entire sample was illuminated.

To calibrate the apparatus, experiments were carried out using bare gold-plated lithium tantalate, and compared with the known absorbance of gold to determine the sensitivity of the whole system at each wavelength step. As well, absolute

absorptances of the polymers and the bare gold-plated lithium tantalate were measured *ex situ* using an integrating sphere. These *ex situ* measurements were used to estimate the polymer thicknesses, as well as for verification of the calorimeter's responses for these substrates prior to calcium deposition, which were in good agreement.

3.3. Processing of Raw Data from Apparatus

3.3.1. Extent of Calcium Deposition

The calcium atom flux incident at the polymer was monitored by a quartz crystal microbalance. The commercial unit used in this task reported film thicknesses in Ångstroms. It is perhaps not the most appropriate, however, to report data from these experiments in thickness of calcium deposited, since this rather naturally leads one to picture a sharp interface between polymer and calcium when considering these systems, which might not be the case. As well, polymer surfaces are seldom perfectly flat. Thus at low coverages the thickness of calcium deposited can easily be of the same order as the height of surface features, which is another detail that one might not picture when discussing possible coverage as a thickness.

A perhaps more instructive unit of metal dosage is the number of atoms per unit area, since this readily allows for comparison with the surface density of repeat units for the polymers studied. However, it must be stressed that we are not necessarily indicating a surface density of calcium atoms when using this unit of measure, but rather a vertical projection of atoms in a given cross-section. The conversion factor between atoms per unit area and the thickness of calcium deposited on the microbalance, assuming bulk metal density, is 2.33 atoms/nm² per Ångstrom, which is obtained from the following relationship:

$$\tilde{n} = \frac{t\rho N_A}{M} \quad (3.1)$$

where t is the thickness of the deposited calcium as reported by the microbalance, ρ is calcium's bulk density, N_A is Avogadro's number, and M is calcium's atomic mass. As a reference, the isotropic areal density for bulk calcium metal is 8.12 atoms/nm², as calculated from the 2/3 power of the bulk density.²⁶

3.3.2. Measured Heat and Standard Enthalpy

The heat measured using the calorimeter, q , is not quite the same as the heat that would be measured under ambient gas conditions. In our experiments, calcium atoms arrive at the sensor with a kinetic energy governed by the velocity selector. As well, the calorimetry experiments were carried out in vacuum. In order to facilitate comparison between our measured heats with tabulated values which are typically enthalpy values, all the heats presented in this work have been converted to take into account these differences.

To arrive at a heat measured under standard conditions, the calcium beam's translational kinetic energy (E_K) needs to be subtracted from the measured heat, while the corresponding kinetic energy for an ambient Ca gas, treated as ideal (the concentration of calcium in the atom beam is low at the fluxes used in the experiments, which makes this a reasonable assumption), needs to be added:

$$-\Delta U = q - E_K + \frac{3}{2}RT \quad (3.2)$$

Here, $\frac{3}{2}RT$ is the translational kinetic energy of an ideal monatomic gas, where T is taken to be 298 K in our conversion. E_K , as calculated from the velocity of the calcium atoms in the beam after passing through the velocity selector, is 9.9 kJ/mol⁶² while $\frac{3}{2}RT$ equates to 3.7 kJ/mol.

In order to compare to standard enthalpies for reactions of a gas to make a solid product, we add a further factor of $-P\Delta V = RT$, the “work of compression”. This assumes all the Ca gas condenses, which may not be true at all coverages. However as a convenience in data presentation, the heat curves have this constant correction

applied at all coverages. The possible error introduced is small, less than 2.5 kJ/mol at room temperature, compared to our measured heats of typically 190 kJ/mol.

All the reaction heat data presented in this work are exothermic. One should bear in mind therefore that while all the heats presented in this thesis are shown as positive values, there should be a negative sign associated with them, as indicated on the vertical axis labels.

4. Calorimetric Studies

4.1. MEH-PPV

The heat signal for Ca on MEH-PPV as a function of calcium dosage is shown in **Figure 4.1**, which is an average of 4 trials, each starting from a freshly prepared bare polymer film. The reaction heat dropped off very quickly at low coverage and settled to an essentially constant heat by around 6 atoms/nm². Note that while the data beyond 25 atoms/nm² is not shown in **Figure 4.1**, this same signal continues on to 60 atoms/nm² and beyond, the longest exposures measured. We ascribe this constant heat signal to calcium deposition on a thick calcium overlayer. All the various trials showed decays with similar rates, and with initial heats that are within 50 kJ/mol from the averaged value of 360 kJ/mol. If we define the interaction energy between the calcium and the polymer as just that amount of the heat evolved above the heat of bulk metal growth, i.e. the area between the heat curve and the horizontal line on the graph, the interaction energy between Ca and MEH-PPV is 40 µJ/cm² of exposed polymer substrate.

The exposure by which point the heat decay subsided correlates with a study by Y. Yang *et. al.*⁶⁹ Those authors found, via current-brightness-voltage measurements, that the performance of MEH-PPV based PLED devices improved markedly as a function of deposited calcium thickness when it was less than around 2 Ångstroms, or 5 atoms/nm², while no meaningful improvement could be realized afterwards. They suggested that n-doping of the polymer was essentially complete by this coverage, thus explaining the performance plateau. Perhaps our high initial reaction heat was also related to the n-doping of the polymer, with this reaction completed by around 6 atoms/nm². This also agrees with another PLED device performance study by Gao *et. al.*,⁷⁰ where the authors measured photoluminescence intensity (PL) of a PPV polymer without side groups as a function of deposited calcium. They observed a

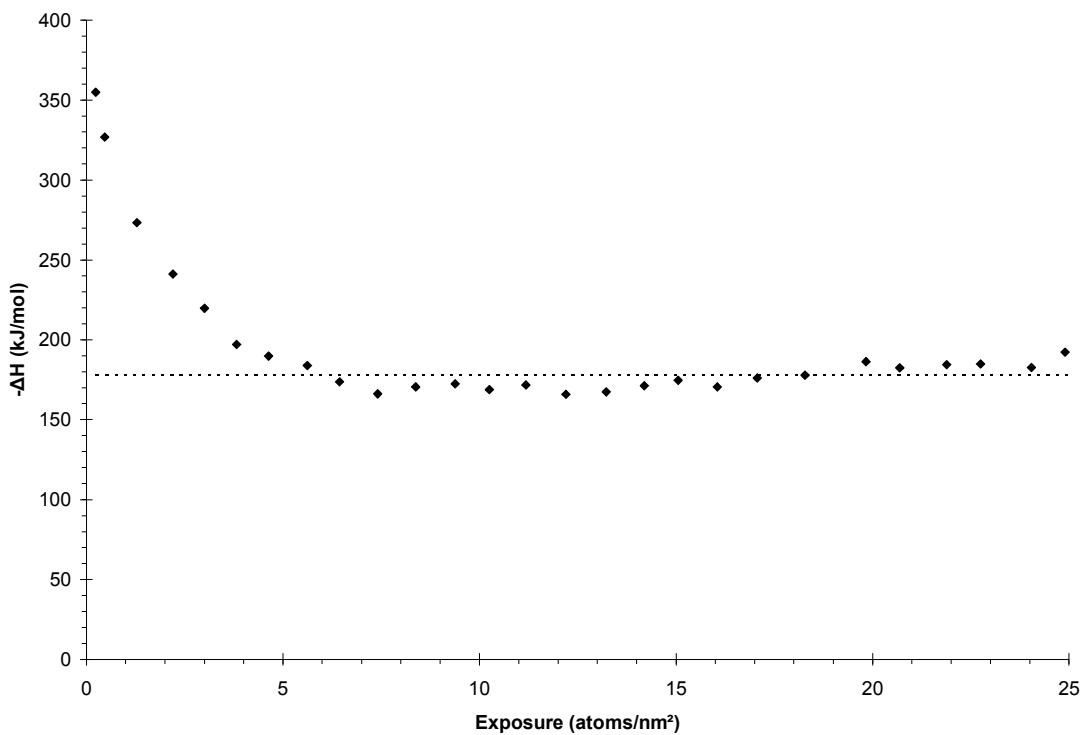


Figure 4.1: Calorimetric data of MEH-PPV with calcium

The high initial reaction heat of ~ 360 kJ/mol decays rapidly; from ~ 6 atoms/nm² onward the reaction heat is essentially constant at ~ 180 kJ/mol. The dotted line indicates the calcium condensation enthalpy.

decrease in PL, which was again attributed to n-doping of the polymer by calcium, that levelled off by roughly the same coverage. Furthermore, the authors attributed the PL levelling to bulk metal formation, which correlates with our constant heat from ~ 6 atoms/nm² onward. It is perhaps worth noting, however, that the exposure resolution on these other studies were rather coarse on the order of 2 to 5 atoms/nm², while our resolution is considerably finer.

Figure 4.2 shows a logarithmic plot of the reaction heat against calcium exposure, where the logarithm of the difference between ΔH , the reaction heat at a given coverage, and ΔH_B , the asymptotic heat, is plotted. As can be seen from the linear behaviour, the initial drop in heat was an exponential decay. This result strongly suggests a two-state model, where a high reaction heat occurs for calcium atoms incident on unoccupied sites and a low reaction heat occurs for calcium atoms incident on already occupied sites. We can analyse the reaction heat using this 2-state model by writing the measured heat as a sum of two terms, one each for the high and low energy states, designated as A and B respectively:

$$\Delta H = f_A \Delta H_A + f_B \Delta H_B \quad (4.1)$$

ΔH in this expression is the heat measured, ΔH_A and ΔH_B are the binding energies of the respective sites, and f_A and f_B are the fractions of calcium from the metal beam that react with the respective sites. The immediate drop in calorimetric heat with exposure indicates that the calcium atoms are not able to move around the surface searching for the A sites with the larger reaction enthalpy. Instead the exponential drop in heat indicates that the atoms either react or desorb at the first site encountered, so that the fraction of atoms that react at empty A sites is proportional to the fraction of the surface still composed of such sites. Note that this supposition does not necessarily preclude calcium atoms from diffusing into the polymer, nor their lateral movement on the polymer surface: it only states that there is no preference for

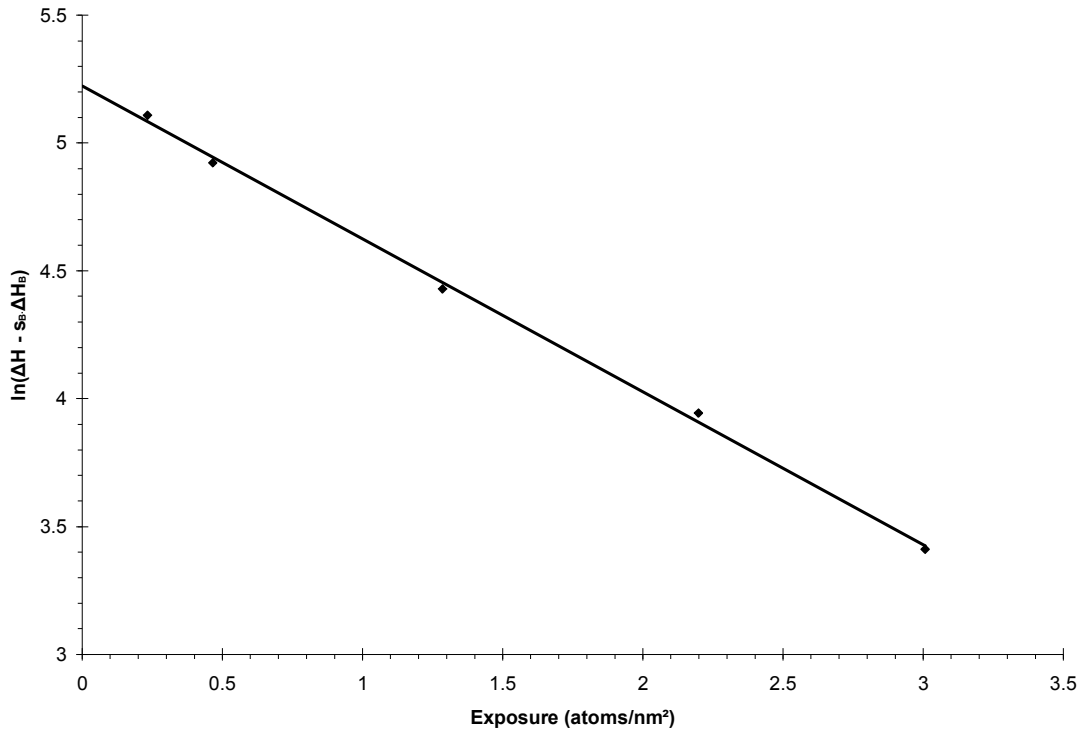


Figure 4.2: Logarithmic plot of MEH-PPV calorimetric data

The natural logarithm of the difference between the heat and the asymptotic heat is plotted against the amount of deposited calcium. This exponential decay of reaction heat points strongly at the presence of a 2-energy-state system in the calcium deposition on MEH-PPV.

calcium to either reaction site, and that the calcium atom is immobilized after a reaction. Writing n_A as the number of empty site A, n_0 as the total number of sites A and B combined, and s_A as the sticking probability for site A, the fraction of free site A is:

$$f_A = s_A \frac{n_A}{n_0} \quad (4.2)$$

Since the reaction site is either an A site or a B site at any moment, an analogous expression can be written for f_B , with s_B being the sticking probability for site B:

$$f_B = s_B \left(1 - \frac{n_A}{n_0}\right) \quad (4.3)$$

For each incremental amount of incident calcium atoms $d\theta$, we have:

$$dn_A = -f_A d\theta = -s_A \frac{n_A}{n_0} d\theta \quad (4.4)$$

Rearranging this separable differential equation and integrating from $n_A = n_0$ at $\theta = 0$ yields:

$$\frac{n_A}{n_0} = e^{\frac{-s_A}{n_0} \theta} \quad (4.5)$$

An expression for the measured heat can then be obtained by combining equations 4.5, 4.3, 4.2 and 4.1. Rearranging the result of this substitution gives:

$$\ln(\Delta H - s_B \Delta H_B) = -\frac{s_A}{n_o} \theta + \ln(s_A \Delta H_A - s_B \Delta H_B) \quad (4.6)$$

which is straight-line plot shown in **Figure 4.2**. In this model site A is depleted over time and turns into site B, which does not deplete; in other words, reaction B is a metal condensation reaction.

At this point, a conservative further assumption is that the thick film condensation energy is -178 kJ/mol,²⁶ and the sticking of metal atoms on the thick film is near unity.^{68,71,72} With this calibration (discussed earlier), the intercept of the straight line plot in **Figure 4.2** corresponds to a heat of reaction of 360 kJ per mole of incident calcium atoms, while the slope (n_0 / s_A) yields 1.7 sites/nm². The density of binding sites is therefore 1.7 sites/nm² multiplied the sticking probability. We then consider as a hypothesis that there is unit sticking between calcium and the polymer. This appears to be a common assumption in the literature, where coverage is typically equated with exposure in studies on the deposition of materials onto organic substrates of interest to electronic devices.^{46,51,69,70,73-80} It also seems likely with respect to the large reaction heat observed per incident atom. That being said, there is at least one system with high initial reaction heat that has a low initial sticking probability,⁶⁸ and so the alternative of a coverage dependant non-unit sticking must be kept in mind.

According to data in the literature, there are ~1.9 monomers per nm² at the surface of MEH-PPV.⁸¹ A reaction site density of 1.7 sites/nm² from our model (or lower, if there is non-unit sticking) might suggest that each calcium atom is bound to at most 1 monomer unit. However calcium is known to be multiply coordinated in its known metallocene compounds. If this is the case for PPV, our result indicates that calcium would have to at least have limited diffusivity into the polymer, which is not precluded from the analysis presented here. We have not claimed that the reaction sites are at the surface instead of within the polymer's near-surface region: one can certainly envision reaction sites that are surrounded by more than one functional

group on the polymer chain or a few neighbouring chains such that they can only be found within the polymer film. Indeed, this limited diffusivity has been reported by some researchers.⁸² However, it is a controversial subject: calcium diffusivity has been deemed by yet others to be very limited, if it occurs at all.^{71,75}

The initial heat of 360 kJ/mol is a large binding energy, but how does it compare to the value for other polymers? Since calorimetry is a novel technique in studying polymer metallization, there are not many binding energies to compare the MEH-PPV values with. One polymer that was studied previously in our group is the polyimide pyromellitic dianhydride-oxydianiline (PMDA-ODA, the chemical structure is shown in **Figure 4.3**), which had a binding energy of 610 kJ/mol with calcium, and displayed a similarly profiled heat curve as the Ca/MEH-PPV system.⁸³ We note that MEH-PPV has an electron affinity of 250 kJ/mol (2.6 eV),¹⁵ which is larger than that of PMDA-ODA at 140 kJ/mol (1.4 eV).⁸⁴ The smaller binding energy for MEH-PPV is therefore somewhat surprising, since a stronger ionic contribution to the bonding with calcium might be expected. However, the large electron affinity in MEH-PPV is due to the extended conjugation instead of localized electronegative carbonyls in PMDA-ODA. This large EA can potentially suffer considerably when localized interaction with calcium forms and destroys the conjugation, which is one possible explanation for the observed smaller binding energy for MEH-PPV.

As mentioned previously in the calcium chemistry discussion (**Chapter 2**), there are claims in the literature that calcium deposition on PPV-type polymers leads to the formation of calcium oxide through reactions with oxygen impurities trapped in the polymer.⁴⁶ Experiments were thus carried out on oxygen-treated MEH-PPV.

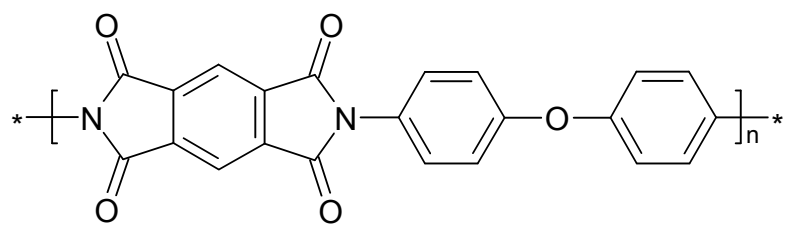


Figure 4.3: Chemical structure of the polyimide pyromellitic dianhydride-oxydianiline
PMDA-ODA

4.2. Oxygen-treated MEH-PPV

In these experiments, the polymer was first treated with oxygen before calcium deposition, which we did by exposing the polymer to a dry oxygen atmosphere in the dark prior to calorimetry experiments. If the reactivity seen in untreated MEH-PPV was due to trapped oxygen impurities, a similarly shaped heat curve ought to be observed in these experiments with oxygen-dosed samples.

The heat of reaction as a function of calcium exposure on oxygen-treated MEH-PPV is presented in **Figure 4.4**, which is an average of 3 trials, all showing similar flat behaviours. There is a marked difference in profile between the heat curves of MEH-PPV and the oxygen-dosed samples. The initial heat of the latter is much lower, at ~ 180 kJ/mol and the entire heat curve is relatively flat, with the peak at ~ 5 atoms/nm 2 barely ~ 30 kJ/mol larger than the initial value. The high initial heat observed previously for MEH-PPV is absent in these oxygen-treated samples. This strongly suggests that the reaction seen previously is not due to trapped oxygen as other researchers have proposed.

Compared with the bulk standard heat of formation of calcium oxide from the elements, which is 634.9 kJ/mol,²⁶ and the corresponding value of 611.4 kJ/mol²⁷ for calcium peroxide, the measured heat for the oxygen-treated polymer is extremely low. In fact, the calorimeter should have measured 810 or 790 kJ/mol respectively²⁶ if CaO or CaO₂ was formed since the calcium in the experiments was from an atom beam and can be considered to be gaseous, instead of the solid calcium at standard conditions. The small heat signal obtained may indicate a low sticking coefficient for calcium atoms on the oxygenated surface, which would require that the molecular oxygen has a significant activation barrier to reaction and is also able to prevent the polymer from reacting. Alternatively, the low heat observed in this system is due to the small size of the product clusters formed, since the formation of bulk ionic solids involves a large amount of long range lattice energy. A more appropriate comparison

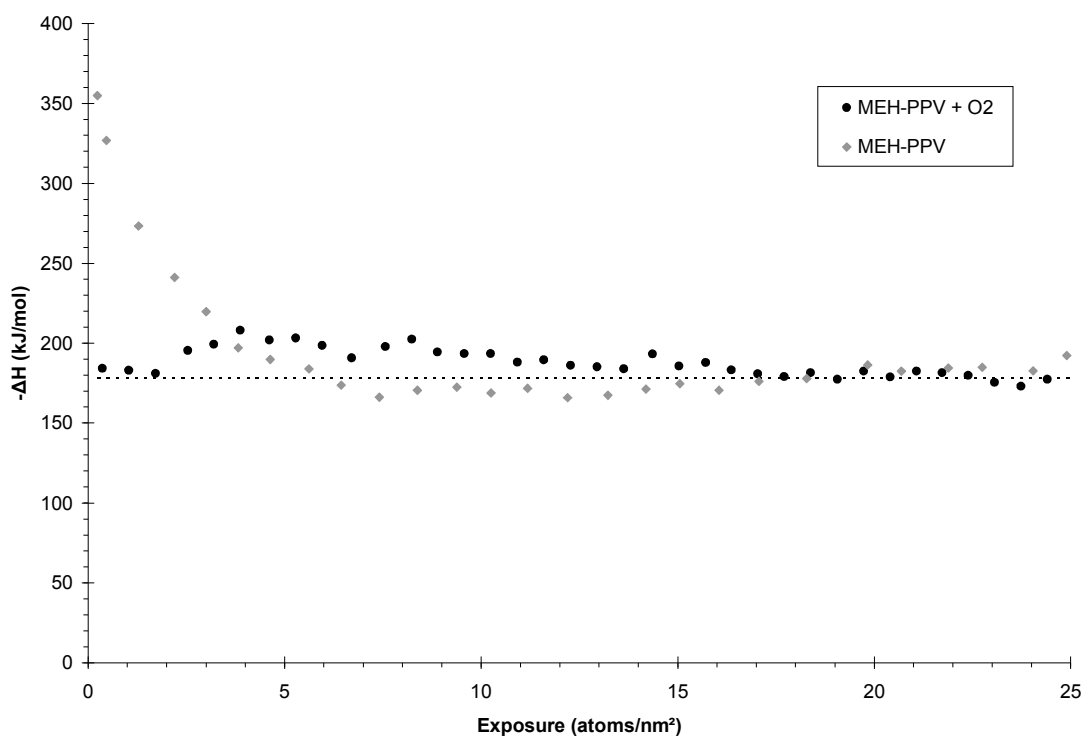


Figure 4.4: Calorimetric data of oxygen treated MEH-PPV.

The heat curve is almost flat, peaking to ~ 210 kJ/mol at about 5 atoms/ nm^2 . The dotted line indicates the calcium condensation enthalpy.

then would be with the formation of gas phase oxide molecules as opposed to bulk CaO or CaO₂ solids.

In an infrared study of the reaction between gas-phase Ca and O₂, the authors concluded that there is a significant amount of gaseous molecular calcium peroxide present through comparison of IR spectra with DFT calculations.⁸⁵ The calculated dissociation energy of this molecule towards the gaseous elements is 250 kJ/mol. This value is roughly similar to the ~180 kJ/mol observed in the oxygen-treated MEH-PPV, in contrast to the bulk heat of formation of CaO and CaO₂.

Other than molecular calcium peroxide, molecular calcium oxide has also been studied in the literature. There is general agreement between various experiments and theory that the bond dissociation energy of gaseous diatomic CaO is 400 kJ/mol.⁸⁶⁻⁸⁸ Given that the standard heat of formation of atomic O from diatomic oxygen gas is 250 kJ/mol,²⁶ the reaction between calcium atom and oxygen gas to form diatomic CaO has a reaction heat of 150 kJ/mol. This reaction heat is similar the reaction heat of ~180 kJ/mol observed for the oxygen-treated MEH-PPV.

Having concluded that the high initial heat observed for calcium deposition on MEH-PPV is not likely to be due to oxygen impurities, it would be instructive to systematically study other polymers to investigate how different functional groups contribute to the reactivity. Since the vinylene double bond has been claimed to be a reaction site towards calcium,^{44,45} MEH-PPP, which does not have the vinylene double bond but is otherwise identical to MEH-PPV, was next studied.

4.3. MEH-PPP

The calorimetric data of MEH-PPP is presented in **Figure 4.5**. The interaction energy for this system, defined again as the total heat generated in excess of the heat of metal film growth measured at high coverage, is $120 \mu\text{J}/\text{cm}^2$. This is substantially larger than was found for MEH-PPV, but is delivered more “slowly”, i.e. over a larger dosage regime. The initial heat of $\sim 200 \text{ kJ/mol}$ of incident atoms is much smaller than the 360 kJ/mol observed for MEH-PPV. The reaction heat increases to $\sim 250 \text{ kJ/mol}$ as the exposure increases to $\sim 3 \text{ atoms}/\text{nm}^2$. Since MEH-PPP and MEH-PPV differ only by the lack of vinylene groups in the backbone of the former polymer; the very different heat curves strongly suggest that the binding site on MEH-PPV is the vinylene moiety.

It should be pointed out at this point that the data presented is an average of just two experiments. Three more experiments were carried out, but during these experiments, for reasons that are still unknown, the calorimeter signal underwent large sudden stepwise changes. Even in those experiments, though, the general peak shape seen in **Figure 4.5** could be discerned. The location of the peak is consistently at $\sim 3 \text{ atoms}/\text{nm}^2$ in all experiments performed. The numerical values of the reaction heats for the two averaged experiments differed by $\sim 50 \text{ kJ/mol}$ both for the initial heat, and the maximum heat.

The shape of the heat curve is not an exponential decay, thus the reaction kinetics between calcium and MEH-PPP did not proceed as previously discussed for MEH-PPV. It is surprising that while the initial heat is much smaller than for MEH-PPV, the total interaction energy is much larger. The integrated heat as a function of exposure is shown in **Figure 4.6**. It suggests that more calcium atoms are able to react with the MEH-PPP, due either to a greater surface density of sites or to a deeper calcium penetration into the polymer. One possibility is that the strong reaction between calcium and vinylene in MEH-PPV forms a barrier preventing further

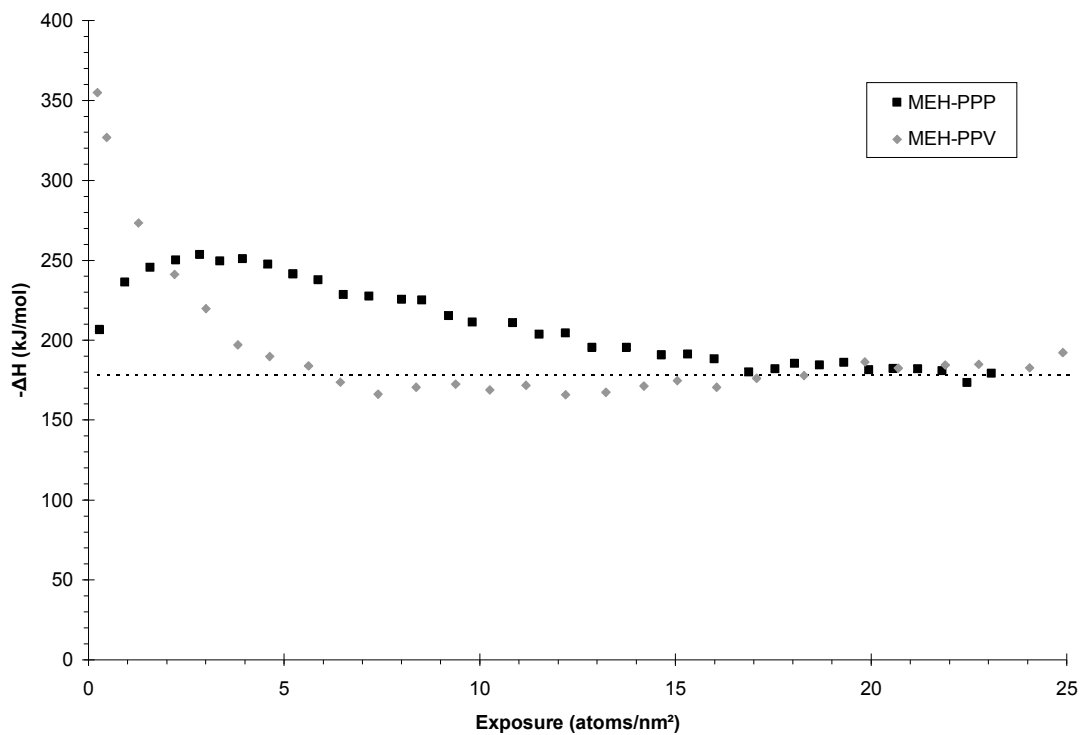


Figure 4.5: Calorimetric data of MEH-PPP

The shape is distinctly different from the Ca/MEH-PPV system, with a pronounced peak at ~ 3 atoms/ nm^2 . The dotted line indicate the calcium condensation enthalpy.

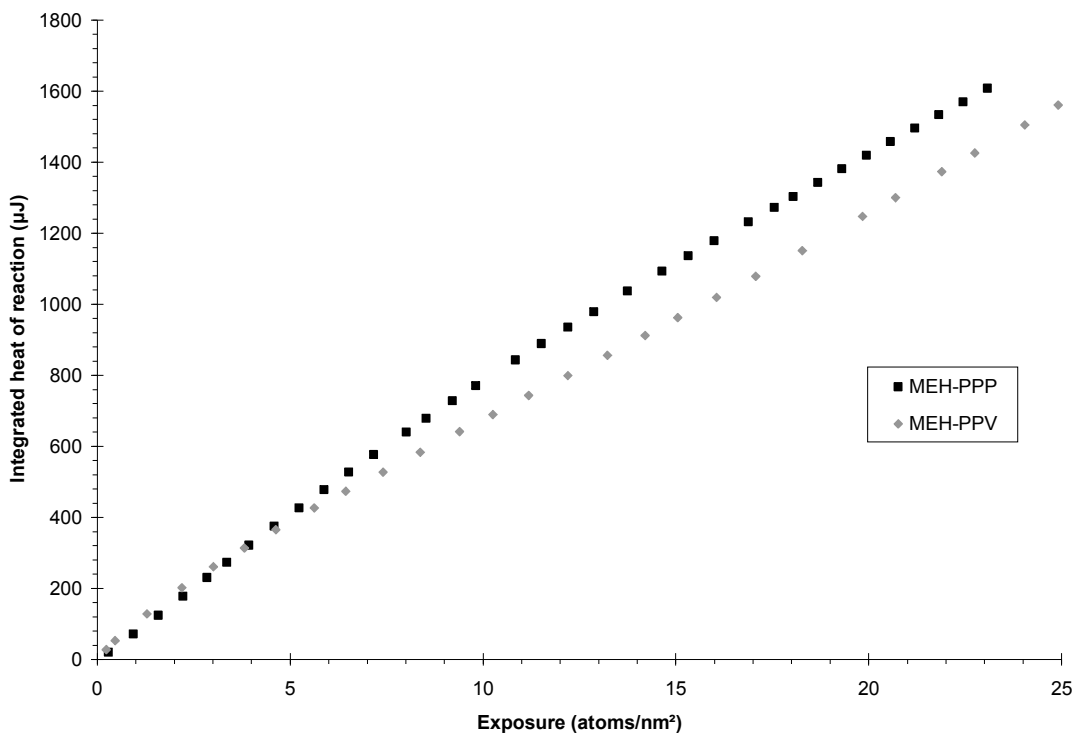


Figure 4.6: Integrated reaction heats for MEH-PPV and MEH-PPP

Note the larger total amount of heat evolved during calcium deposition on MEH-PPP. This may be due to a more thorough reaction with MEH-PPP than MEH-PPV.

reaction or penetration.

Looking at the shape of the heat curve, it resembles in profile the build up and subsequent decay in the amount of some intermediate species during a sequential A → B → C reaction. Thus we attempt to model the reaction heat of the MEH-PPP/Ca system using those classic kinetics. In this model the calcium reacts with a particular reaction heat if it encounters an empty reaction site, reacts with a different reaction heat if it arrives at an “intermediate species” site which has already been activated by reaction with another Ca atom, and reacts with a heat corresponding to the heat of condensation for sites which have already reacted with two or more Ca atoms. This is similar then to the previous model for MEH-PPV, except that each reaction site can accept two calcium atoms before acting as a nucleation site for calcium overlayer growth.

For the sake of simplicity in the following discussion of this 3-state model, a reaction site that is empty will be referred to as site A, while one that has received one calcium atom will be referred to as B, and C otherwise. In other words, the binding site changes from being an A site to a B site upon receiving a calcium atom, and finally to a C site which continues to act as a C site upon further calcium deposition. In terms of chemical formulae then, the following describes this three-state model:



Mathematically then, if the numbers of binding sites with 0, 1, and 2 or more calcium atoms, corresponding to sites A, B, and C, are designated as n_A , n_B and n_C respectively, while n_0 designates the total number of binding sites, these different numbers of sites can be related by:

$$n_A + n_B + n_C = n_0 \quad (4.7)$$

Using the same notations as before with f 's of different subscripts being the fractions of the calcium beam that reacts with the respective sites and ΔH of different subscripts being the respective reaction heats, the measured heat can be written as a sum of three terms:

$$\Delta H = f_A \Delta H_A + f_B \Delta H_B + f_C \Delta H_C \quad (4.8)$$

If calcium atoms bind to the first site encountered upon deposition regardless of which type it is, as in the previously proposed 2-state model for MEH-PPV, the fractions of incident atoms that react with the respective sites are equal to the corresponding fractions of empty site on the surface multiplied by their respective sticking probabilities s_A , s_B and s_C , such that:

$$f_A = s_A \frac{n_A}{n_0}, \quad f_B = s_B \frac{n_B}{n_0}, \quad f_C = s_C \left(1 - \frac{n_A}{n_0} - \frac{n_B}{n_0}\right) \quad (4.9)$$

Rate equations can then be written to derive expressions for the number of each type of site. Before proceeding to derive mathematic expressions, however, it is perhaps instructive to first consider qualitative how these three n_i 's should evolve over the course of deposition.

Prior to any deposition, all of the binding sites are empty, thus they are all A sites, such that $n_A = n_0$. As calcium is deposited, some of the A sites become B sites, thus n_B grows in the expense of n_A . Since the number of binding sites is limited, $n_A \rightarrow 0$ after a large amount of Ca is deposited. B sites will also be depleted as the deposition progresses as they are converted into C sites, thus the number of B sites should increase from 0 prior to deposition, and subsequently decay back to 0. There is no C

site prior to deposition as well, but since C sites react with calcium to give further C sites, $n_C \rightarrow n_0$ after a large amount of calcium is deposited.

Having discussed qualitatively how n_A , n_B and n_C should evolve as a function of the amount of deposited calcium, let us now consider the mathematics of this model. Concentrating for the moment on the reaction $A + \text{Ca} \rightarrow B$, the number of times this occurs, $r_{A \rightarrow B}$, depends on the amount of calcium arriving at the polymer, θ , as well as the fraction that reacts, f_A . Writing this in differential form then yields:

$$dr_{A \rightarrow B} = f_A d\theta = s_A \frac{n_A}{n_0} d\theta \quad (4.10)$$

A similar expression can be written for the reaction $B + \text{Ca} \rightarrow C$ as well. Since the change in the number of a particular site depends both on the number of reactions that create it as well as the number of reactions that destroys it, the following rate equations are obtained:

$$\frac{dn_A}{d\theta} = \frac{-dr_{A \rightarrow B}}{d\theta} = \frac{-s_A}{n_0} n_A \quad (4.11)$$

$$\frac{dn_B}{d\theta} = \frac{dr_{A \rightarrow B} - dr_{B \rightarrow C}}{d\theta} = \frac{s_A}{n_0} n_A - \frac{s_B}{n_0} n_B \quad (4.12)$$

The differential equation 4.11 is the same as the one in the previously described 2-state model (equation 4.4), such that the integrated form is:

$$n_A = n_0 e^{\frac{-s_A \theta}{n_0}} \quad (4.13)$$

Having obtained an expression for n_A , we can now proceed to derive an expression for n_B . Substituting equation 4.13 into 4.12 yields the following differential equation after some rearrangements:

$$\frac{dn_B}{d\theta} + \frac{s_B}{n_0} n_B = s_A e^{\frac{-s_A}{n_0} \theta} \quad (4.14)$$

To solve this differential equation, we multiply both sides by an integrating factor:

$$\frac{dn_B}{d\theta} e^{\frac{s_B}{n_0} \theta} + n_B \frac{s_B}{n_0} e^{\frac{s_B}{n_0} \theta} = s_A e^{\frac{-s_A}{n_0} \theta} e^{\frac{s_B}{n_0} \theta} \quad (4.15)$$

The left hand side of this equation is then just the derivative of the product between n_B and the exponential term. Simplifying the right hand side then gives:

$$\frac{d}{d\theta} \left(n_B e^{\frac{s_B}{n_0} \theta} \right) = s_A e^{\frac{s_B - s_A}{n_0} \theta} \quad (4.16)$$

We then integrate from $n_B = 0$ at $\theta = 0$ to arrive at the expression for the number of free B sites after some rearrangement:

$$n_B = \frac{s_A}{s_B - s_A} n_0 \left(e^{\frac{-s_A}{n_0} \theta} - e^{\frac{-s_B}{n_0} \theta} \right) \quad (4.17)$$

Finally, we can write an expression for the measured reaction heat by substituting equations 4.13 and 4.17 into 4.9, then into 4.8:

$$\Delta H = s_A e^{\frac{-s_A \theta}{n_0}} \Delta H_A + \frac{s_A s_B}{s_B - s_A} \left(e^{\frac{-s_A \theta}{n_0}} - e^{\frac{-s_B \theta}{n_0}} \right) \Delta H_B \\ + s_C \left[1 - e^{\frac{-s_A \theta}{n_0}} - \frac{s_A}{s_B - s_A} \left(e^{\frac{-s_A \theta}{n_0}} - e^{\frac{-s_B \theta}{n_0}} \right) \right] \Delta H_C \quad (4.18)$$

In this model, there are 7 parameters that can be used to fit the experimental data: the number of reaction sites n_0 , the 3 sticking probabilities for the different type of sites s_A , s_B , s_C , and the 3 binding energies for these sites ΔH_A , ΔH_B , ΔH_C . After we assign site C as metal condensation sites as before, such that $\Delta H_C = -178$ kJ/mol and $s_C = 1$, we are left with 5 parameters to fit the data. Before attempting any data fitting, it is perhaps instructive to first explore how the parameters affect the shape of the calculated heat curve.

The dependence of the heat curve on the different parameters is shown in **Figure 4.7**, where a single parameter is varied in each set of the curves. As can be seen from the figure, n_0 affects the width and location of the peak on the exposure axis. s_A and s_B both affect the height of the peak, as well as the rate at which it grows and decays. Since ΔH_A corresponds to the initial heat of the system, this parameter affects where the heat curve begins at zero exposure, while ΔH_B primarily affects the height of the peak.

As shown in **Figure 4.8**, we can fit the data with various sets of parameters, all with a R^2 value of around 0.985. To further the analysis, let's suppose there is unit sticking between calcium and polymer, which is, as pointed out earlier, commonly assumed in the literature, and see if the resulting values yield reasonable results.

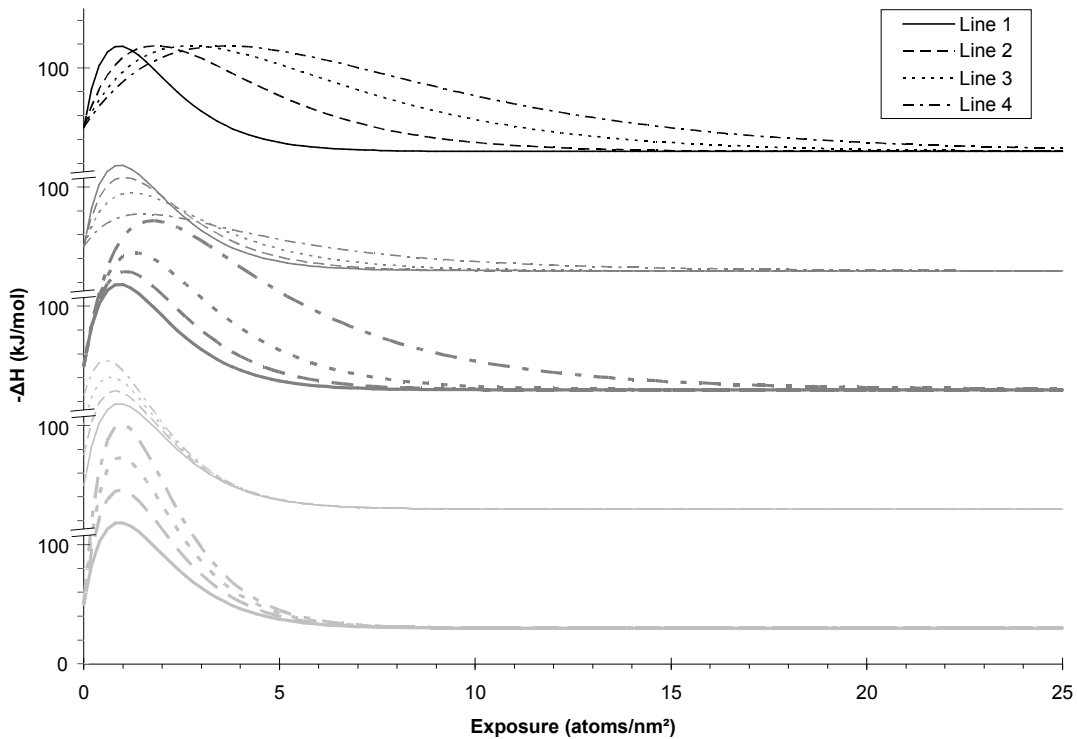


Figure 4.7: Heat curves generated using the 3-state, 5-parameter model

Different n_0 (sites/nm²), s_A , s_B , ΔH_A and ΔH_B (kJ/mol) are plotted to illustrate their respective effect on the shape of the curve. The first line in each set of curves has $n_0 = 1$, $s_A = 1$, $s_B = 1$, $\Delta H_A = 200$ and $\Delta H_B = 400$, while the other lines in the set have the same parameters as the first line except for one varying parameter. The first set of lines have $n_0 = 1, 2, 3$, and 4 . The second set of lines have $s_A = 1, 0.75, 0.5$, and 0.25 . The third set of lines have $s_B = 1, 0.75, 0.5$, and 0.25 . The fourth set of lines have $\Delta H_A = 200, 225, 250, 275$. The last set of lines have $\Delta H_B = 400, 475, 500$, and 625 .

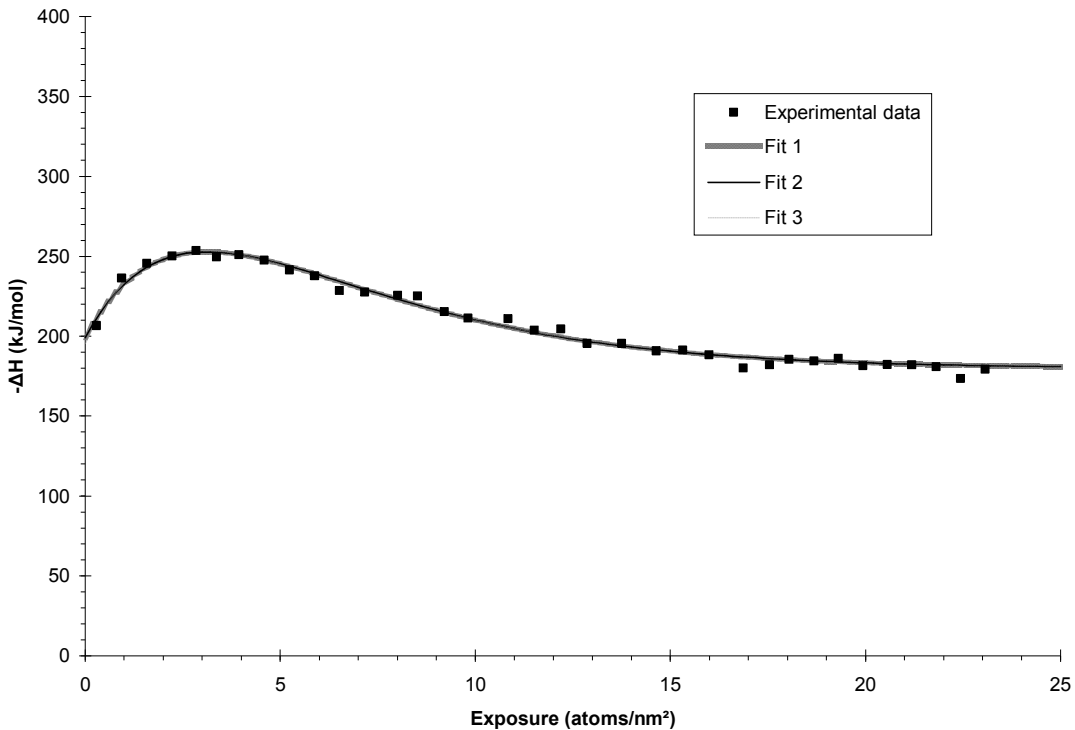


Figure 4.8: Various best fits for MEH-PPP calorimetric data using the 3-state, 5-parameter model

Fit 1 has $n_0 = 3.49$ sites/nm², $s_A = 1.00$, $s_B = 1.00$, $\Delta H_A = 199$ kJ/mol and $\Delta H_B = 358$ kJ/mol. Fit 2 has $n_0 = 1.66$ sites/nm², $s_A = 0.476$, $s_B = 0.476$, $\Delta H_A = 199$ kJ/mol and $\Delta H_B = 358$ kJ/mol. Fit 3 has $n_0 = 0.272$ sites/nm², $s_A = 0.0566$, $s_B = 0.118$, $\Delta H_A = 195$ kJ/mol and $\Delta H_B = 449$ kJ/mol. It's clear that there is no unique fit.

It should perhaps be noted that equation 4.18 fails when $s_A = s_B = 1$, due to the $(s_B - s_A)$ term in the denominator. In that case the differential equation 4.16 drops the exponential term on the right, with the result:

$$\Delta H = e^{\frac{-\theta}{n_0}} \Delta H_A + \frac{\theta}{n_0} e^{\frac{-\theta}{n_0}} \Delta H_B + \left(1 - e^{\frac{-\theta}{n_0}} - \frac{\theta}{n_0} e^{\frac{-\theta}{n_0}} \right) \Delta H_C \quad (4.19)$$

But in practice, it is sufficient for our fitting to use equation 4.18, with two just slightly different values assigned to the sticking probabilities, e.g. $s_A = 1$ while $s_B = 0.999$.

The least-squares best fit for unit sticking occurs with $n_0 = 3.49$ sites/nm², $\Delta H_A = 199$ kJ/mol, and $\Delta H_B = 358$ kJ/mol. This now appears to be a unique fit, as this set of parameters represent a local minimum for the least squares values in the ranges $0.5 < n_0 < 19.5$ sites/nm², $-100 < \Delta H_A < 800$ kJ/mol, and $-100 < \Delta H_B < 800$ kJ/mol, which should be chemically reasonable limits for the parameters. As mentioned previously, the R² value is 0.985, indicating a very good fit, which gives some credence to this intermediate species model.

Without experiments using other techniques, it is impossible to determine the exact nature of the reaction products. The low initial heat may be due to a weak calcium-polymer interaction, or a strong interaction that is offset by bond breakage, such as the abstraction of oxygen from alkoxy side chains, or cleavage of the polymer backbone, which would require an appreciable amount of energy. With that said, the extracted binding energies from the proposed model can be interpreted to give a reaction scheme that is consistent with the experiment data. In fact, it is one that is not as radically different from MEH-PPV as it might appear.

The value of ΔH_B , the binding energy for the second incident calcium atom, has a best fit value of 358 kJ/mol. This is the same value as the 360 kJ/mol that corresponds to the binding energy between calcium and MEH-PPV. Since we have suggested that calcium is likely to be reacting with vinylene double bonds in MEH-PPV, perhaps we should explore the possibility that the second calcium atom arriving at an MEH-PPP binding site also reacts with a double bond. Since the only double bonds formally present in MEH-PPP are on the phenyl rings, the supposition that the second calcium reacts with a “free” double bond requires that the aromaticity of the ring be broken. This then leads to the hypothesis that the first calcium atom breaks the aromaticity of the phenyl ring. Thus, if we suppose that the first calcium reacts also via a double bond, the extracted first binding energy ΔH_A should be less than ΔH_B by the aromatic stabilization energy.

What is the value of the aromatic stabilization energy? One way to estimate this is through the comparison of thermodynamic properties of benzene with other relevant non-aromatic compounds. A benzene molecule formally has three carbon-carbon double bonds. If there was no aromatic stabilization, the hydrogenation of 1 mole of benzene to cyclohexane should give off a similar amount of energy as the hydrogenation of 3 moles of ethene to ethane. The standard enthalpies of formation from the elements for these four simple compounds are shown in **Table 4.1**.²⁶ The enthalpy change associated with the hydrogenation of 1 mole of benzene is -205.5 kJ, while the corresponding value for the hydrogenation of 3 moles of ethene is -409.2 kJ. Comparing these enthalpy changes, the aromatic stabilization in benzene is therefore ~200 kJ/mol. Similarly, a comparison amongst the enthalpies of hydrogenation for cyclohexane, 1,3-cyclohexadiene and benzene (**Table 4.2**)⁸⁹ yields an aromatic stabilization of ~150 kJ/mol, which is a similar value as the estimate from hydrogenation.

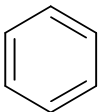
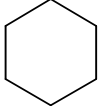
Name	Formula	Standard enthalpy of formation (kJ/mol)
Benzene		49.1
Cyclohexane		-156.4
Ethene	$\text{H}_2\text{C}=\text{CH}_2$	52.4
Ethane	$\text{H}_3\text{C}-\text{CH}_3$	-84.0

Table 4.1: Standard enthalpy of formation for some simple organic molecules

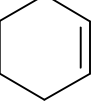
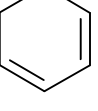
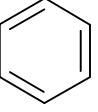
Name	Formula	Standard enthalpy of hydrogenation (kJ/mol)
Cyclohexene		-118
1,3-Cyclohexadiene		-230
Benzene		-206

Table 4.2: Standard enthalpy of hydrogenation for some simple organic molecules

The difference between ΔH_A and ΔH_B is 159 kJ/mol. This is very similar to the aromatic stabilization energy estimates above. The binding energies from the 3-state model is therefore consistent with a reaction scheme where calcium atoms react with the phenyl rings in MEH-PPP, with each of these reaction sites reacting with 2 calcium atoms before becoming nucleation sites for calcium island and/or overlayer growth with subsequent deposition. If this model is correct it suggests that reaction of the Ca with the vinylene group protects the neighbouring phenyl ring from attack.

It would have been instructive to compare the derived density of reaction sites with the surface density of MEH-PPP monomer units. Unfortunately structural information about PPP-related materials is scarce in the literature: the only we are aware of is for sexiphenyl (6P), an oligomer of the unsubstituted PPP-backbone (i.e., a chain of six phenyl rings attached at the 1,4-positions). As a reference then, the isotropic monomer areal density of 6P crystals grown via vapour deposition is 8.6 units/nm², determined using x-ray and transmission electron diffraction techniques.⁹⁰ This value is significantly larger than the 3.5 reaction sites/nm² deduced for MEH-PPP. It would be expected though that the vapour-grown 6P would have a higher monomer unit density than the MEH-PPV, due to its lack of bulky side groups and to its well ordered crystal packing compared to the spin-coated polymer.

It is tempting to think of the reaction sites we have proposed as binding sites that are located immediately at the surface of the substrate, such that the deposited atoms must only react from above. If viewed in this manner, our model with 2 calcium atoms reacting with one single phenyl ring seems highly improbable: it would not seem sensible for two calcium atoms, each with a diameter of 2.8 Å,²⁶ to react with a single phenyl ring, which is about 2.8 Å across.²⁶ However, we are not suggesting that both calcium atoms must interact on the same side of the phenyl ring. Instead, a picture where the two calcium atoms react on different sides of the phenyl ring would

be more appropriate, such as in the case of the bridging cyclopentadienyl ligands in calcacene as we have discussed in the introduction.

We should state clearly here that if each MEH-PPP binding site reacts with 2 calcium atoms while each MEH-PPV site reacts with only 1, and if the site density on the MEH-PPP is about twice that of the MEH-PPV, we are actually proposing that the number of reacted calcium atoms with the MEH-PPP is 4 times larger than with the MEH-PPV. In this context we note that the model does not preclude calcium atoms from moving into the near surface region of the polymer upon deposition; it only requires them to be immobilized once they have encountered a reaction site.

The binding site areal densities for the two polymers, 1.7 sites/nm^2 and 3.5 sites/nm^2 , are each smaller than the areal density of calcium in a bulk film, which is 8.1 atoms/nm^2 . It is not proposed that the condensation proceeds as a continuous metal film at low coverages. Instead, reacted binding sites act as nucleation centres, such that calcium clusters grow both laterally and vertically.

4.4. P3HT

The calorimetric data for the P3HT/Ca system is presented in **Figure 4.9**, which is an average of 4 trials. The interaction energy for this system is $\sim 100 \text{ }\mu\text{J/cm}^2$, which indicates some reaction between calcium and the polymer. However the initial heat signal is very low at $\sim 100\text{kJ}$ per mole of incident atoms. This is followed by a strong rise upon further deposition to a peak value of $\sim 220 \text{ kJ/mol}$ at $\sim 12 \text{ atoms/nm}^2$. It is interesting to note that a significantly higher calcium dosage is needed to reach a constant metallization heat than was the case for MEH-PPV or MEH-PPP substrates.

It is obvious that this heat curve is not an exponential decay, thus the reaction between P3HT and calcium did not proceed with the same kinetics as in MEH-PPV. At first glance the P3HT heat curve resembles that of MEH-PPP, which leads one to suspect similar reaction kinetics. **Figure 4.10** shows the curve that best fits the data using the 3-state model discussed previously, with the same chemically reasonable limits on the parameters as before and assuming unit sticking. It is not a very good fit, with a R^2 value of 0.9374. It is also apparent that the fit does not accurately reproduce the curvature on either side of the peak. A better fit cannot be achieved even when freely adjusting all five parameters. We conclude then that the reaction kinetics are actually different from that with MEH-PPP.

For completeness, **Figure 4.11** is a comparison of the integrated reaction heats amongst the three polymers studied in this thesis. The integrated heat of P3HT is appreciably lower than the others, as one would expect from the very low initial heat and the large calcium coverage required before the peak is reached. It does, however, overtake MEH-PPV at higher coverages.

The very low initial heat observed in the P3HT experiments is rather surprising. The most straightforward explanation to this would be that perhaps P3HT has very little reactivity towards calcium. This would seem to conflict with the numerous accounts of reactive metals interacting with polythiophene-related materials through bonding

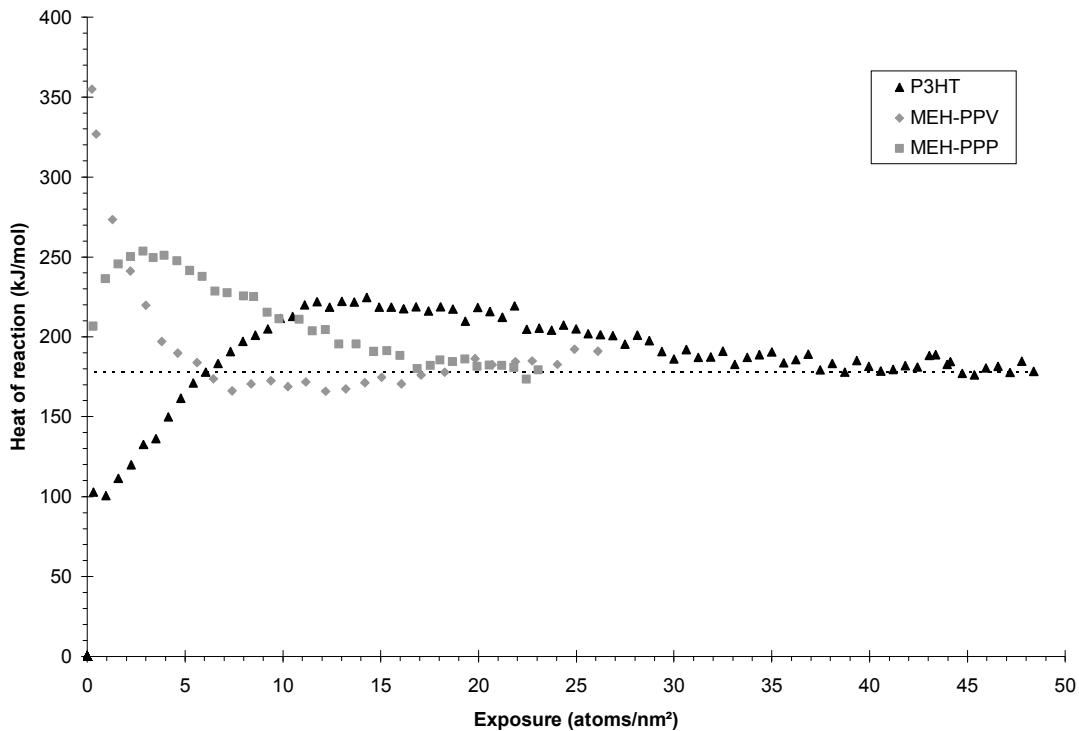


Figure 4.9: Calorimetric data of P3HT

The shape of the heat curve is different from the other two systems. As well, a much larger amount of calcium is required before the heat signal started levelling off. The dotted line indicates the calcium condensation enthalpy.

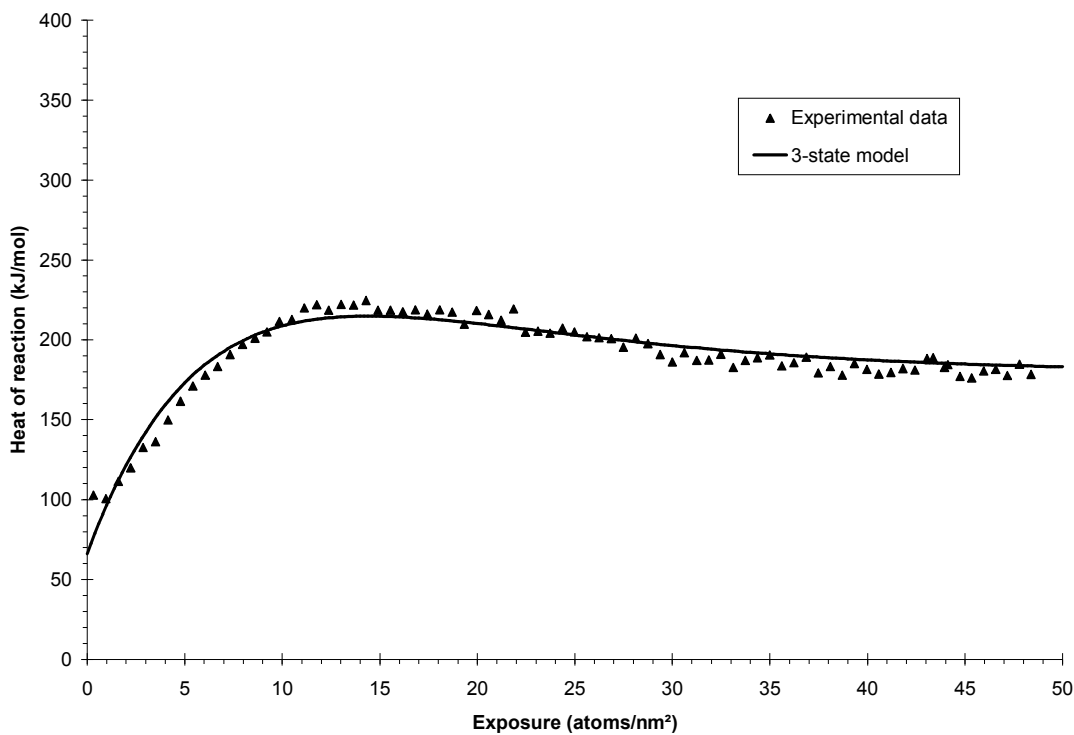


Figure 4.10: Fitting of P3HT calorimetry data using the 3-state model

The best fit curve has $n_0 = 8.8 \text{ sites/nm}^2$, $\Delta H_A^\circ = 66 \text{ kJ/mol}$, $\Delta H_B^\circ = 359 \text{ kJ/mol}$ when unit sticking is assumed. The 3-state model does not fit the P3HT data very well, with a R^2 value of 0.9374.

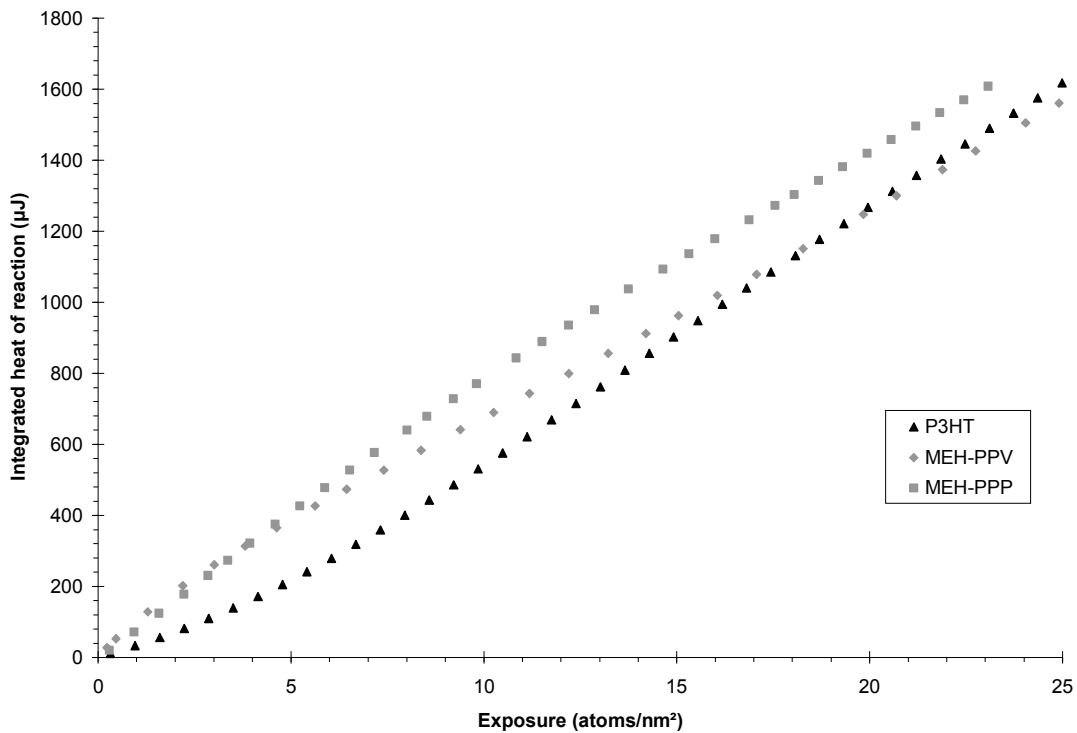


Figure 4.11: Comparison of integrated reaction heats amongst MEH-PPV, MEH-PPP and P3HT

The integrated reaction heat of P3HT is appreciably lower at low coverages than both the other polymers. The peaked nature of the heat curve, however, does translate to an integrated heat that overtakes MEH-PPV at higher coverages.

at the sulphur centres, or at the carbons in the thiophene rings, or through doping, as discussed in **Chapter 2**. However, we are not aware of any study done specifically on the P3HT/Ca system.

While it is very tempting to attribute the low initial heat to low reactivity (including low sticking), this is not necessarily the case. Strong interactions that are offset by energetically expensive processes can also explain the low initial heat. One such scenario would be if calcium undergoes an energetically expensive sulphur atom abstraction upon deposition onto the P3HT surface, as has been argued for the formation of sulphides when sodium is deposited onto thiophenes.⁵³ Indeed, in this picture, there is another factor that can contribute to the low initial heat: when the amount of deposited calcium is small, the CaS would form small clusters, thus having a low heat of formation as opposed to the high heats associated with the long range Madelung energy of a bulk crystal.

Similarly shaped heat curves have been observed for some other systems in the literature. In systems where Pb atoms are deposited onto either metal oxides or poly(methyl methacrylate) substrates, the initial rise in heat has been attributed to the growth of Pb islands.^{91,92} When the amount of deposited metal is small, these metal clusters are tiny, such that the number of interactions between Pb atoms is low, leading to a low reaction heat. As the clusters grow in size incoming metal atoms can interact with more neighbouring atoms, thus leading to the heat increase towards the bulk heat of condensation. Those authors observed but did not discuss the fact that the reaction heat rises above the bulk heat of condensation before settling down, just as in our Ca/P3HT data (**Figure 4.10**). This effect was also observed in unpublished work in our group on Cu cluster growth on a polyimide substrate. These observations can be explained by coalescence of the islands at high coverage, where metal atoms filling in voids between clusters actually have more interactions than for bulk film growth.

In the case of Pb deposition the authors measured initial sticking coefficients of between ~ 0.2 and ~ 0.4 , depending on the substrate.^{91,92} This sticking increased continuously as a function of coverage, approaching unity for bulk metal film growth. For our system of Ca on P3HT, the low initial heat of ~ 100 kJ per mole of incident atoms makes it plausible that it also has a low initial sticking.

Even without knowledge of the sticking coefficients, the information obtained in the calorimetry experiments should be useful for device fabrication, since the heat curve gives a good indicator of the exposure regime over which reaction with the polymer is occurring. But in an attempt to improve our analyses we have explored using the calorimeters sensitivity to optical absorbance as a means of measuring the sticking as a function of calcium exposure. The results of these experiments will be discussed in Chapter 5.

4.5. Summary of Calorimetric Studies

In this chapter, we have shown that MEH-PPV, MEH-PPP and P3HT have distinct reaction kinetics. The reaction heat of MEH-PPV decays exponentially with calcium exposure. This reaction heat profile has been attributed to a reaction between polymer and calcium, which is consistent with a 2 step chemical process where the second step is calcium condensation. If we assume unit sticking, the reaction heat for Ca atoms in the first step is 360 kJ/mol, with a projected site density of 1.7 sites/nm². We have also concluded that the binding site is very likely to be the vinylene double bond on the polymer backbone.

MEH-PPP has also been shown to react with calcium. However, the reaction kinetics is rather different from that seen in the MEH-PPV/Ca system: the reaction heat increases initially, before decaying to a constant value at higher calcium coverage. This suggests a 3 step process, with the last one being calcium condensation.

Assuming unit sticking, the reaction heat in the first step is 200 kJ/mol, and is 360 kJ/mol in the second step, while the projected site density is 3.5 sites/nm². We propose that the binding site for this polymer is the phenyl ring on the polymer backbone, where each ring can react with 2 calcium atoms, the first atom having a lower reaction heat due to aromatic stabilization of the still intact phenyl ring.

The reaction heat of the P3HT/Ca system also increases initially before decaying to a constant value. This is roughly similar to the MEH-PPP system, however the data cannot be fit to a 3 step reaction model. The calorimetric data is consistent with calcium island growth without a strong interaction with the polymer. However, the reaction heat profile may also be due to the formation of a product that simultaneously alters the polymer's chemical structure significantly, e.g., the formation of a calcium sulphide film which involves abstracting sulphur atoms from the thiophene backbone.

5. Optical Studies

As has been discussed in the previous chapter, it is important to study whether all the incident calcium atoms are sticking to the surface of the polymer. While our data, reported in terms of calcium exposure, is valid as presented and constitutes measurements that are novel to the study of these systems, it would certainly be more meaningful if we can instead report our findings in terms of calcium coverage, which would allow us to compare our reaction heats with standard reaction heats of tabulated reactions and hopefully gain more insight into our results. Our first attempt in measuring the sticking probability was to use a line-of-sight mass spectrometer to detect any calcium atoms that might reflect from the polymer surface instead of sticking.⁶⁰ Unfortunately there was not enough signal strength from our mass spectrometer, most likely due to the geometrical constraints present in our current vacuum chamber design. Our next attempt was to use XPS to determine the absolute amount of calcium deposited. However, because of the need to transfer the samples from one vacuum chamber to another, an unacceptable amount of contamination from atmospheric gases such as oxygen and water vapour was introduced, which made XPS an unviable method for measuring sticking in our experiments.

Since the calorimeter can detect heat due to light absorption, we determined that it was possible to detect changes in the amount of light absorbed as a function of calcium deposition. We therefore worked to use the calorimeter as an analytical tool to quantify calcium coverage, and also as a spectroscopic tool to probe the electronic structure of the interfaces. The discussion presented in the rest of this chapter is the result from this exploratory work.

5.1. Laser Studies

5.1.1. Modelling of Data

The first set of optical studies was carried out using a readily available red diode laser at 1.85 eV (671 nm). **Figure 5.1** demonstrates the percentage change in the measured signal as calcium was deposited onto P3HT, which can be equated to the percentage change in absorbance, as will be demonstrated shortly. The results for MEH-PPV and MEH-PPP will be presented in later pages. The absorbance of the P3HT/Ca system increases monotonically as a function of calcium coverage with some roll over at higher coverages. The R^2 value for a linear fit on this data is 0.9365, with a slope of $\sim 6.5 \times 10^{-3}$ initially and $\sim 1.7 \times 10^{-3}$ at the high coverage end.

This is an interesting result. If this system behaves according to Beer's Law, the amount of light the system absorbs should increase linearly as calcium is deposited. This also means that if the sticking probability is to rise as more calcium is deposited, the absorbance plot should curve upwards since the amount of deposited calcium would be increasing faster than linearly over the course of the experiment. The mostly linear increase in absorbance then appears to indicate a uniform sticking probability.

This argument calls for Beer's Law behaviour, which is of course observed in dilute solutions, but may not be a valid assumption for the thin-film system studied here. The concept of absorbance is familiar to chemists. However, absorptance is a more appropriate quantity when discussing thin film optics. It is thus worthwhile to first comment on the relationship between the two measures of light absorption, before we continue with addressing the question regarding thin-film optics.

Absorbance, A_B , is defined as a function of the intensity of the transmitted light that passes through the sample I_{out} and the incoming light intensity I_{in} :

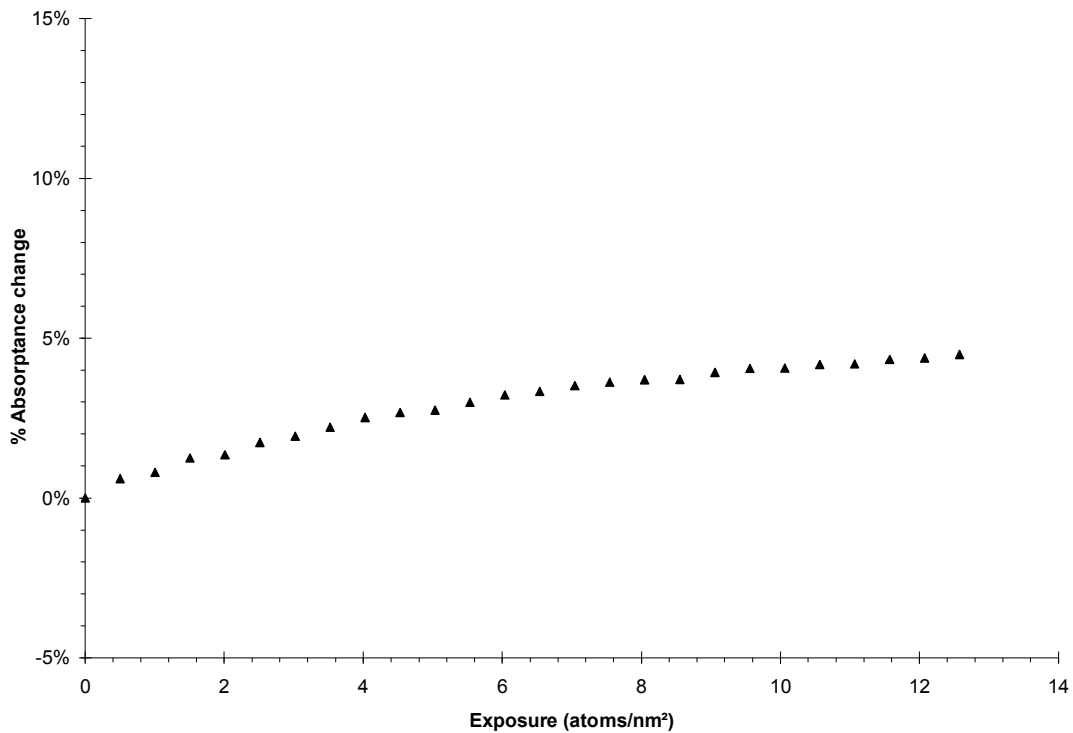


Figure 5.1: 1.85 eV (671 nm) laser diode data for the P3HT/Ca system

The absorbance change is a small rise as a function of coverage with an initial slope of $\sim 6.5 \times 10^{-3}$, rolling over to $\sim 1.7 \times 10^{-3}$ as coverage increased. The linear fit R^2 value is 0.9365.

$$A_B = -\log \frac{I_{in}}{I_{out}} \quad (5.1)$$

Absorptance, A_T , on the other hand, is defined as the ratio of the amount of light absorbed I_A to the amount of incident light I_0 :

$$A_T = \frac{I_A}{I_0} = 1 - R - T \quad (5.2)$$

Absorptance is also related to two other similarly defined quantities reflectance R and transmittance T , corresponding to the amount of light reflected and transmitted respectively as indicated on the expression on the right in equation 5.2.

In standard UV-visible experiments using cuvettes, a blank subtraction procedure is commonly performed, which corrects for the amount of light that is reflected off of the various interfaces between the atmosphere, the cuvette, and the solution, and light that is otherwise scattered. This means that the effective incident light intensity I_{in} is the amount of incident light that is not reflected. Equation 5.1 can thus be re-written as:

$$A_B = \log \frac{I_0(1-R)}{I_T} = -\log T + \log(1-R) \quad (5.3)$$

Recalling that absorptance, reflectance and transmittance add to unity, rearranging equation 5.2 and substituting for T in equation 5.3 yields an expression relating absorbance and absorptance after some rearrangements:

$$A_T = (1-R) \cdot (1 - 10^{-A_B}) \quad (5.4)$$

The exponential term can be written as a series. In the low absorbance regime, higher order terms can be discarded, such that:

$$10^{-A_B} \approx 1 - A_B \ln 10 \quad (5.5)$$

This approximation can be considered acceptable up to an absorbance of around 10%, by which point the error is $\sim 3\%$. Using expression 5.5 then, there is a linear relationship between absorbance and absorptance when only a small amount of light is absorbed:

$$A_T = [(1 - R) \ln 10] A_B \quad (5.6)$$

Since the focus of the optical studies here is on the percentage change in the amount of light absorbed, the constants that differentiate absorptance from absorbance, i.e., $(1 - R) \ln 10$, cancel out in writing $\Delta A/A$, assuming that the reflectance does not change appreciably. There is thus no distinction between percentage absorbance change and percentage absorptance change in the low light absorption regime, which is what we observe in these experiments. From this point onward all references to the amount of light absorbed will be designated as A , and the words absorbance and absorptance will be used interchangeably. However, one must be aware that this is not the case when there is a large amount of absorption: while absorptance can only be as large as unity, absorbance does not have an upper bound.

Having clarified the difference between absorbance and absorptance, we shift our attention back to the question we posed before: can we expect Beer's Law behaviour when calcium is deposited onto the polymer? The metallization is a process that involves, in the most simplistic view, 4 layers of materials, the substrate, the polymer, the metal overlayer, and finally vacuum. We need to determine if the growth of the overlayer should cause a linear increase in absorptance.

This thin-film optics problem can be treated in a similar way as O. S. Heavens did in his analysis on a simpler 3-layer system.⁹³ The complete derivation is presented in **Appendix 1**. Through this analysis, we conclude that there should indeed be a linear increase in the absorptance change with the overlayer thickness, irrespective of how many layers we include in the multilayer model as long as the optical properties of these buried layers do not change in the course of deposition. Our observed linear change of absorptance as a function of calcium dosage for deposition on P3HT lends us some confidence then that there is constant sticking in this system, ruling out that the shape of the heat curve profile was due to a change in sticking. We next examine the laser data in more detail, in an attempt to quantify the absorptance change so that the value of the sticking coefficient might be obtained.

The percentage change in absorptance depends on a number of factors if we are to attempt to analyse it using the simplest multilayer model: the refractive index of the gold substrate, the refractive index of the polymer, the thickness of the polymer, the refractive index of the overlayer, and the thickness of the overlayer. If there is no reaction between calcium and a particular polymer, the growing overlayer may simply be metallic calcium. To determine if this is the case for P3HT, calculations have been carried out at a photon energy of 1.85 eV, using refractive indices found in the literature.^{94,95,96} The thickness of the polymer has been estimated to be 18 nm, as will be discussed later in the xenon lamp section (**Chapter 5.2**). Since no optical data appears to have been published in the literature for P3HT, the refractive index used for these calculations is actually that of poly(3-octylthiophene) (P3OT), a polythiophene polymer with octyl side chains as opposed to hexyl in P3HT. The refractive indices of P3OT and P3HT ought to be rather similar, given the minor differences between the two species.

The result of the calculation, assuming complete sticking of the incident calcium, is shown in **Figure 5.2**. The first thing to note is that the calculation, which was carried out without using the $d \ll \lambda$ approximation, yields an absorptance that increases

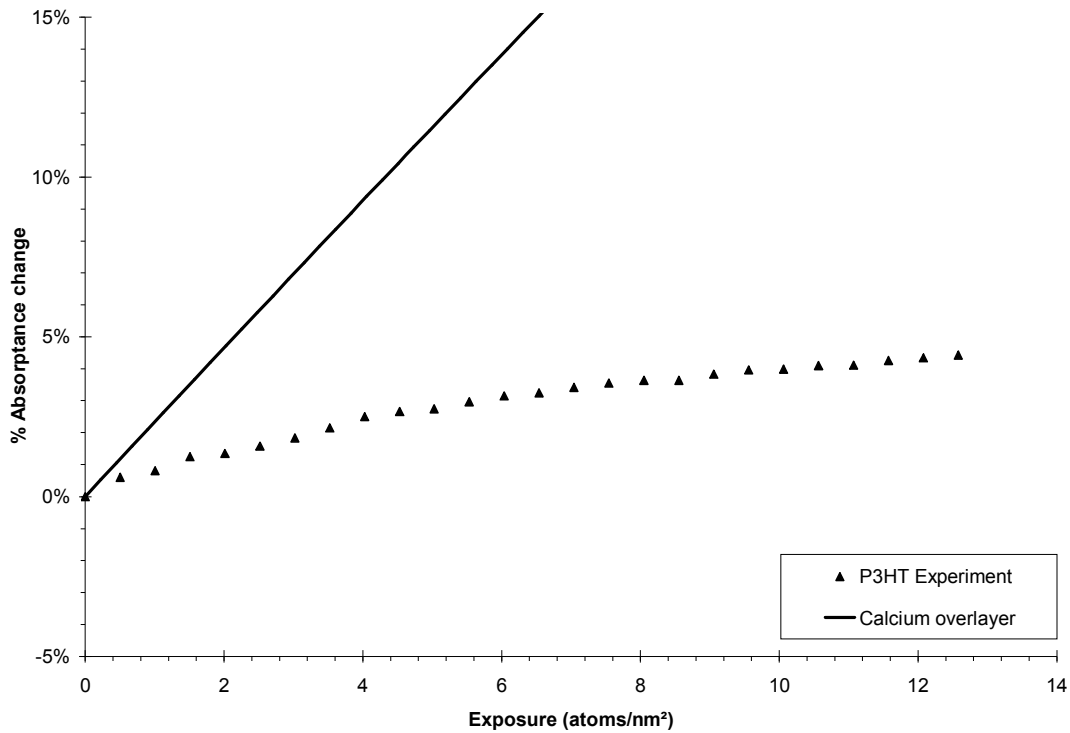


Figure 5.2: 1.85 eV laser data for P3HT, compared with calculated percentage

absorbance changes assuming bulk metallic overlayer

It is obvious that the calculated values do not match the experimental data, indicating either a small calcium sticking coefficient, or that the overlayer does not have bulk metallic properties in this coverage regime.

linearly with coverage; thus this 4-phase model does obey Beer's Law, in accordance with our more general proof. The slope is approximately 7 times steeper than the experimental data, which may indicate a very low calcium sticking. However, there is no curvature in the experimental data even though the calorimetric data indicates that calcium must be reacting with the surface and eventually building up. Also, if the initial sticking is ~14% as the magnitude of the slope suggests, the initial heat of reaction between calcium and P3HT would be ~700 kJ/mol (recall that the initial heat previously reported for this polymer is ~100 kJ/mol of incident calcium), which seems exceedingly large. An alternative explanation is that the calcium overlayer at these low coverages has a dielectric function different than that of a metal film: there are reports by some researchers that even by 30 Å calcium is still not entirely metallic on PPV-type polymers.⁴³

In a second attempt to model the film, the calcium is embedded in a near-surface layer of the substrate to create a film of metal-polymer composite. Since an interfacial region of between 20 to 40 Å has been suggested when calcium is deposited onto a PPV-type polymer,²³ 30 Å is used as the thickness. This layer is treated as a Maxwell-Garnett (MG) film of calcium in P3HT, which takes into account field effects caused by the dispersed particles: MG theory is an effective-medium approximation which describes how oscillators in the film are driven by the incident field plus the polarization field from neighbouring oscillators.^{93,97,98} The refractive index of this MG film is calculated by taking the square root of its dielectric function ε_{MG} , which in turn is calculated using the following relationship:

$$\frac{\varepsilon_{MG} - \varepsilon_p}{\varepsilon_{MG} + 2\varepsilon_p} = q \frac{\varepsilon_{Ca} - \varepsilon_p}{\varepsilon_{Ca} + 2\varepsilon_p} \quad (5.7)$$

where ε_p is the dielectric function of the polymer, ε_{Ca} is the dielectric function of calcium, and q is the volume fraction of calcium in the MG film.

The calculated absorptance change is plotted and shown in **Figure 5.3**. Clearly, this system cannot be properly modeled by a MG film. It is quite surprising that the MG model predicts an even stronger absorbance for the overlayer. This is because at the 1.85 eV photon energy, the real part of calcium's dielectric function $\text{Re}(\varepsilon_{Ca})$ is -6.6, while the corresponding value for the polymer $\text{Re}(\varepsilon_P)$ is 3.4, such that the denominator on the right hand side of equation 5.7 is close to zero.

There are other effective-medium models that offer different approximations to the dielectric function of a medium with embedded absorbers. Our next attempt was therefore to try to see if we can obtain a better fit using the Bruggeman (B) model, the Sheng (S) model, the Landau-Lifshitz-Looyenga (LLL) model, and the Monecke (M) model. The respective expressions for evaluating the dielectric functions, designated as ε_B , ε_S , ε_{LLL} and ε_M , are shown below:⁹⁹

$$(q-1)\frac{\varepsilon_P - \varepsilon_B}{\varepsilon_P + 2\varepsilon_B} = q \frac{\varepsilon_{Ca} - \varepsilon_B}{\varepsilon_{Ca} + 2\varepsilon_B} \quad (5.8)$$

$$\frac{U_1}{U_1 + U_2} \frac{\varepsilon_P - \varepsilon_S}{\varepsilon_P + 2\varepsilon_S} = \frac{-U_2}{U_1 + U_2} \frac{\varepsilon_{Ca} - \varepsilon_S}{\varepsilon_{Ca} + 2\varepsilon_S};$$

$$U_1 = (1 - \sqrt[3]{q})^3, \quad U_2 = (1 - \sqrt[3]{1-q})^3 \quad (5.9)$$

$$\varepsilon_{LLL} = \left[(\sqrt[3]{\varepsilon_{Ca}} - \sqrt[3]{\varepsilon_P})q + \sqrt[3]{\varepsilon_P} \right]^3 \quad (5.10)$$

$$\varepsilon_M = \frac{\varepsilon_P \frac{\varepsilon_{Ca} - \varepsilon_P}{\varepsilon_{Ca} + 2\varepsilon_P} + 4(1-q)\varepsilon_P + 2(1-q)^2(\varepsilon_{Ca} - \varepsilon_P)}{\frac{\varepsilon_{Ca} - \varepsilon_P}{\varepsilon_{Ca} + 2\varepsilon_P} + (1-q)} \quad (5.11)$$

The results of these calculations, as well as from the MG model, are shown in **Figure 5.4**. It should be noted that of the 4 models, the Sheng and Monecke models do not give a dielectric function equalling that of the polymer when the volume fraction is 0,

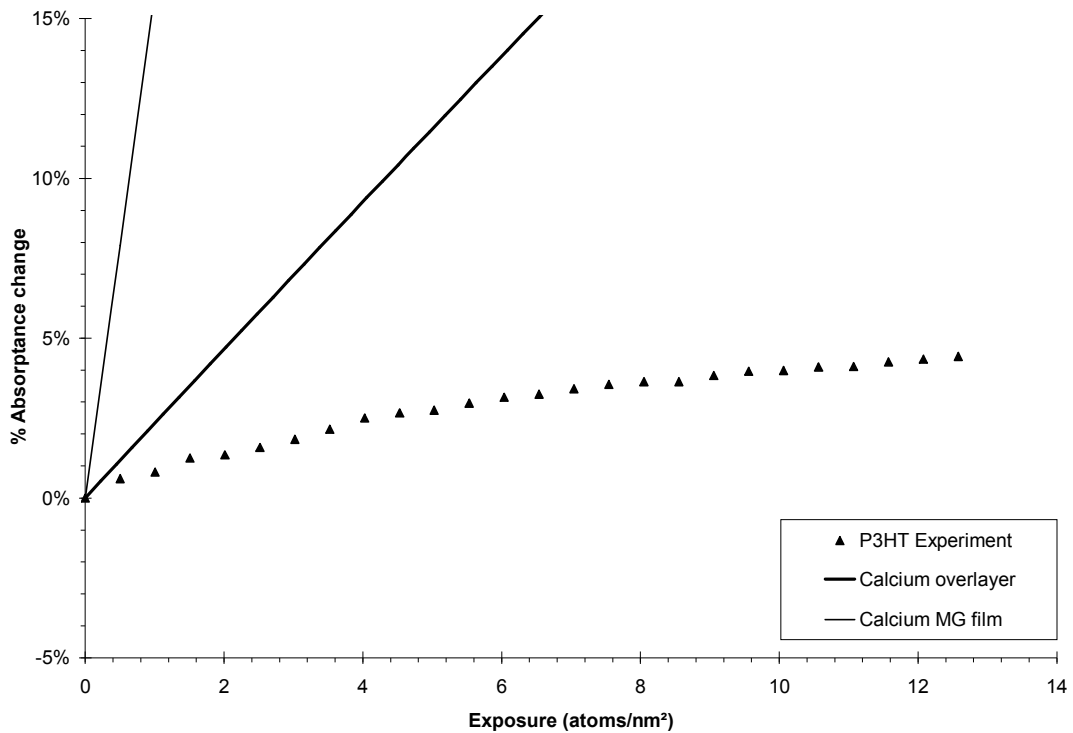


Figure 5.3: Calculation of the percentage absorptance change at 1.85 eV for P3HT where the near-surface region is treated as a MG film
 Clearly the calcium MG film model is not a better model than the calcium overlayer model.

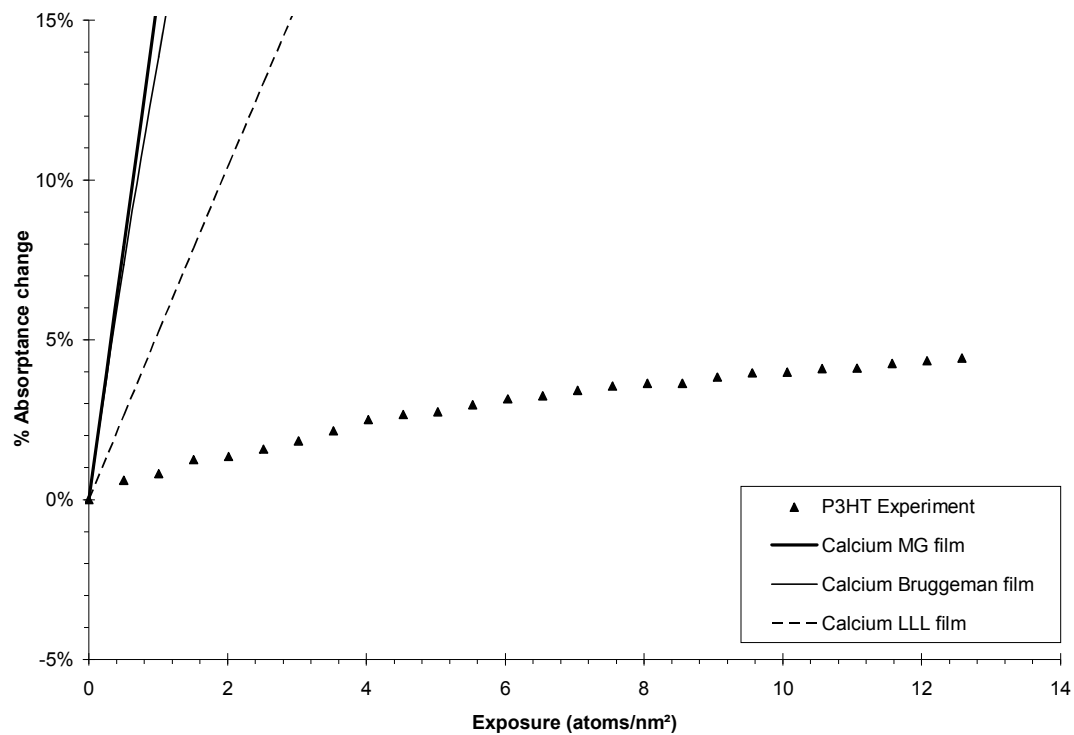


Figure 5.4: Calculation of the percentage absorptance change at 1.85 eV for P3HT using various effective-medium models

While the other models produce better results than MG, they are nonetheless still poor fits to the data.

i.e. when no calcium is present. These 2 models thus yield calculated absorptance changes that are unrealistic in the low exposure regime in our experiments, and are hence not shown in the figure. While the other effective-medium models yields calculated absorptances that are closer to the experimental data, they are still extremely poor fits. This might be an indication that the embedded calcium clusters do not themselves have bulk metal properties, due either to their size or to reaction with the polymer.

According to classical Drude theory which describes metals as having free electrons surrounding the ion cores, the dielectric function of a metal can be written as:^{100,101}

$$\epsilon_{Ca} = \left(1 - \frac{\omega_p^2 \tau^2}{1 + \omega^2 \tau^2} \right) + i \left(\frac{\omega_p^2 \tau}{\omega(1 + \omega^2 \tau^2)} \right) \quad \omega_p^2 = \frac{4\pi e^2 n^*}{m} \quad (5.12)$$

where ω_p is the angular plasma frequency, τ is the relaxation time, ω is the angular frequency of the incident photons, n^* is the effective density of free electrons in the metal, and m is the mass of electron. Since the real and imaginary parts of the refractive index for calcium are known at 1.85 eV, ω_p and τ can be evaluated, which is commonly done in the literature.^{96,102-105} Thinking simplistically, the size of the particle should not significantly affect n^* , and thus ω_p should also not be significantly altered. However, it should play a role in how long an electron can remain free before encountering an edge of the particle, which then leads to scattering. Thus, calculations using the MG, Bruggeman and LLL models are carried out with τ as a fitting parameter. The result is plotted in **Figure 5.5**, where only the fit line using the MG model is shown since the best fit lines for all 3 models are virtually identical.

Whereas bulk calcium has $\tau = 7.6 \times 10^{-16}$ s (calculated from the dielectric function at

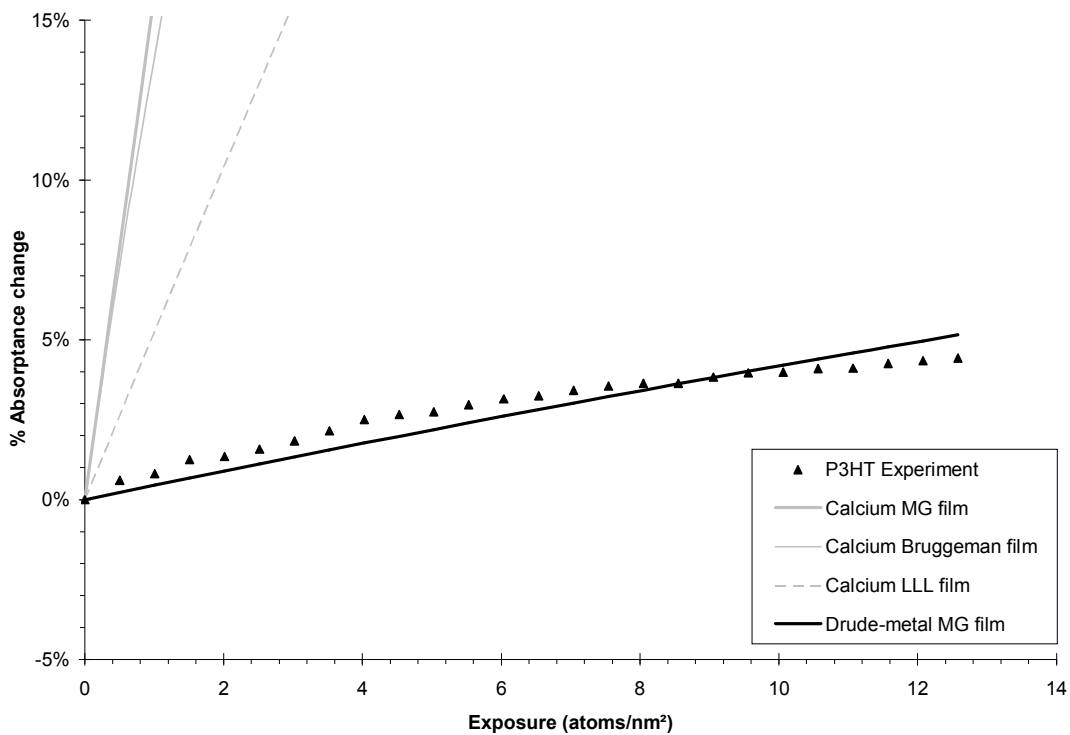


Figure 5.5: Best fit curve for the 1.85 eV P3HT laser experiments using a MG model with a Drude-metal

The best fit τ for the MG model is 2.3×10^{-17} s, while $\tau = 2.2 \times 10^{-17}$ s for the Bruggeman model, and $\tau = 1.8 \times 10^{-17}$ s for the LLL model. These other models yield essentially the same curve as the MG model.

1.85 eV), the least squares fit to the experimental data yields $\tau = 2.3 \times 10^{-17}$ s using the MG model, $\tau = 2.2 \times 10^{-17}$ s using the Bruggeman model, and $\tau = 1.8 \times 10^{-17}$ s using the LLL model. The best fit τ is smaller than the bulk value, which is as should be since the amount of time between scattering events is supposed to be shorter with a smaller particle. However, the calculated bulk calcium value of 7.6×10^{-16} s is quite low: it is comparable to liquid tin's value of between 3.5×10^{-16} and 5×10^{-16} s,⁹⁹ while solid metals typically have values on the order of $10^{-15} \sim 10^{-14}$ s.^{96,104,106-109} Taking calcium's Fermi velocity of 1.3×10^{15} nm/s,¹¹⁰ the small value of $\tau \approx 2 \times 10^{-17}$ s corresponds to an electron mean free path of about 0.3 Å, which is most likely too short to be physical possible.

One possible reason for the failure of Drude theory may be that inter-band transitions can occur in calcium when irradiated with light at 1.85 eV. However, the only reported inter-band transitions below ~5.5 eV are at 5.2 and 4.5 eV,¹¹¹ while a 2.9 eV absorption has been predicted theoretically but not observed experimentally.¹¹² However Lorentz oscillator terms might also need to be added to the Drude dielectric expression in cases where the plasma frequency is a function of nanoparticle size.¹¹³ This is unfortunately impossible to do with the single photon energy used in these experiments.

The laser experiments were carried out originally in a quest to gain more information on the sticking probability, in particular with respect to calcium deposition on P3HT. While the data cannot be used to quantify sticking, it does indicate that the sticking is constant. Since the calorimetric heat increases quite dramatically in this regime, this may indicate the sticking is already close to unity. Unit sticking appears to be a common assumption when vapour depositing calcium on organic substrates.^{46,51,69,70,73-80,114}

While the modelling still requires significant work, thanks to the high signal-to-noise ratio achievable, and it being an *in situ* procedure, this technique does have potential.

With further development it might be integrated with calorimetric measurements to yield real-time sticking information during deposition. As well, it may be possible to develop this technique as a monitor for when the material being deposited attains bulk optical properties.

5.1.2. Absorption Cross-sections

Having discussed the linearity in percentage absorptance change at 1.85 eV for P3HT in relative detail, let us now examine the absorptance changes for all three polymers, which are shown in **Figure 5.6**. The behaviour of MEH-PPP is very similar to that of P3HT: they are both essentially straight lines with very similar slopes. More interesting, however, is the behaviour of MEH-PPV, which shows a dramatic rise initially before settling to a linear rise with a similar slope as the other two polymers by ~ 6 atoms/nm². Note that this correlates very well with the calorimetric data, which levels out at roughly the same coverage, as can be seen in **Figure 5.7** when the two sets of data are plotted in the same graph.

In order to gain more insight about the different slopes seen in MEH-PPV versus P3HT and MEH-PPP, it may be helpful to look at the absorptance changes in terms of absorption cross-sections, σ . The change in absorptance formally depends on the number of absorbers in a film, and also local field effects that are dependent on the distribution of absorbers, as well as thin film interference effects as demonstrated in the thin film optics discussion in **Appendix 1**. Thin film effects can be accounted for by using the multilayer model composed of the gold substrate, the polymer, a near-surface layer where the absorbers are embedded in the polymer, and vacuum. We can then extract absorption cross-sections by neglecting local field effects, as is often the case in literature.¹¹⁵ We should keep in mind that the local field contribution to the optical response could change with coverage, but the low observed absorptance of about 0.05 (absolute absorptances of the polymers prior to calcium deposition will be

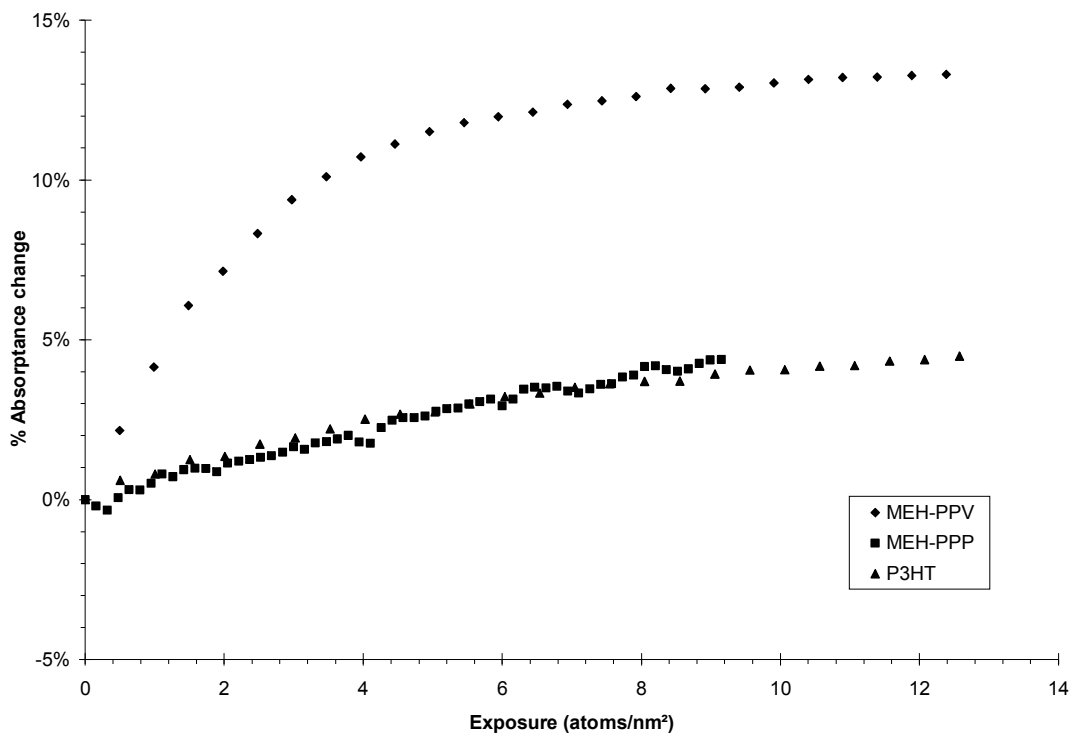


Figure 5.6: Percentage absorptance changes at 1.85 eV for all three polymers studied in this thesis

The behaviours of MEH-PPP and P3HT are very similar, with essentially linear rises of similarly small slopes. MEH-PPV shows a much different profile, growing quickly initially before tapering off to a linear rise with a similar slope as the other polymers by $\sim 6 \text{ atoms/nm}^2$.

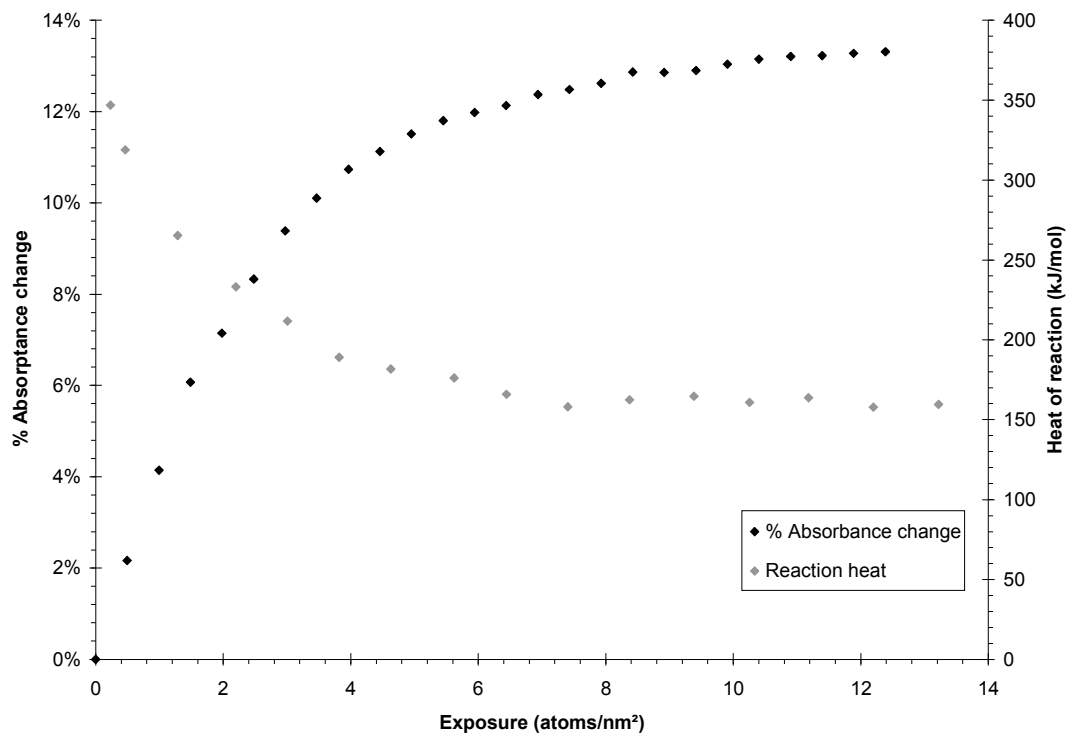


Figure 5.7: Laser data at 1.85 eV and calorimetry data for MEH-PPV

Both sets of data have an initial rapid change that tapers off by ~ 6 atoms/nm², suggesting that both the heat and absorptance change are caused by the same chemistry.

presented in the next section) implies that there should only be a small polarization effect. We thus tentatively analyse the data by assuming a Beer's Law-type behaviour where the amount of absorption is proportional to the number of absorbers in the film, i.e., that the extinction coefficient α , which is itself dependent on the imaginary part of the refractive index k , can be written in terms of σ such that:

$$\frac{4\pi k}{\lambda} = \alpha = \rho\sigma \quad (5.13)$$

where $\lambda = 671$ nm is the wavelength of the light and ρ is the density of absorbers.

An expression for translating k into σ can then be written taking into account film thickness:

$$n\sigma = \frac{4\pi kd}{\lambda} \quad (5.14)$$

where n is the projected areal density of absorbers, and d is the thickness of the film that the absorbers are embedded in. In order to obtain σ , multilayer calculations are carried out using k as a fitting parameter to arrive at the observed absorptance changes. The value of k is then converted into $n\sigma$ via expression 5.14 and plotted. It should be noted that, due to interference effects, the value of k , and thus $n\sigma$, is dependent on the assumed thickness of the absorbing near-surface layer. Since the diffusion layer has been suggested to be between 20 to 40 Å when calcium is deposited onto PPV-type polymer, as mentioned previously,²³ calculations are carried out for these two thicknesses. **Figure 5.8** is the result of these calculations for P3HT, while the results for MEH-PPV, using the refractive index by M. Tammer *et al.*¹¹⁶, is shown in **Figure 5.9**. Calculations are not performed for MEH-PPP, since the absorptance change for this polymer is very similar to P3HT such that the P3HT

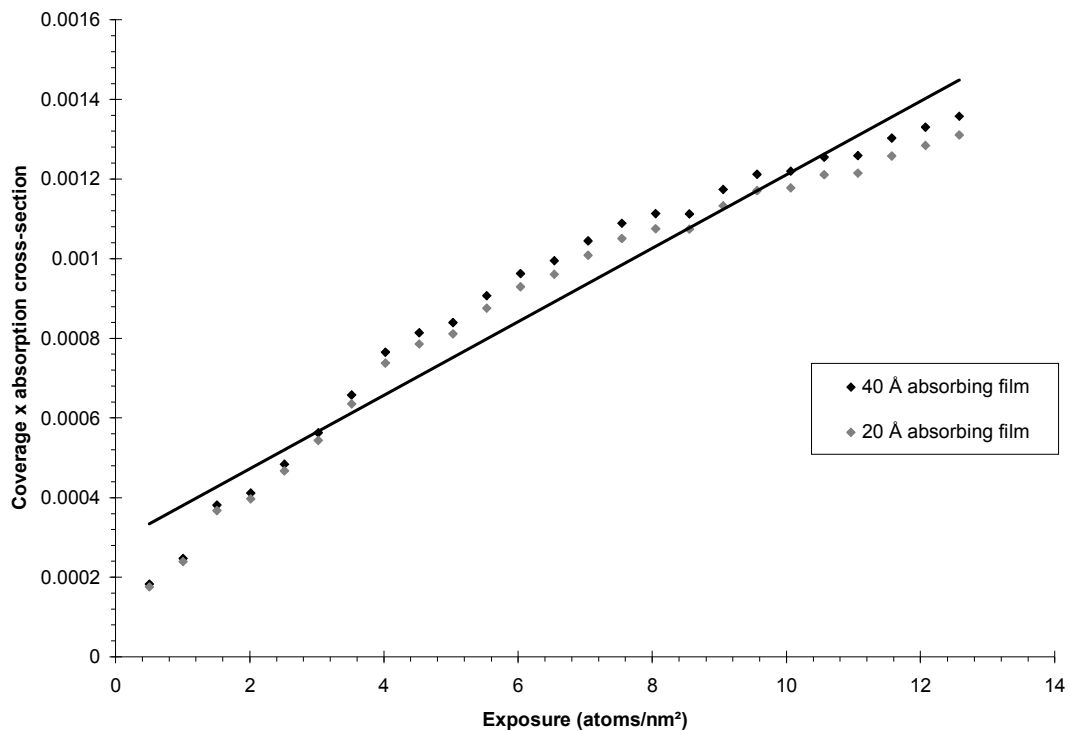


Figure 5.8: Plot of $n\sigma$ as a function of calcium deposition for P3HT

Results for both 20 and 40 Å thick diffusion layers are shown in this graph. The absorption cross-section, which is the slope, has been found to be $9 \times 10^{-19} \text{ cm}^2$, as indicated by the best fit on the average of the two diffusion layer thicknesses.

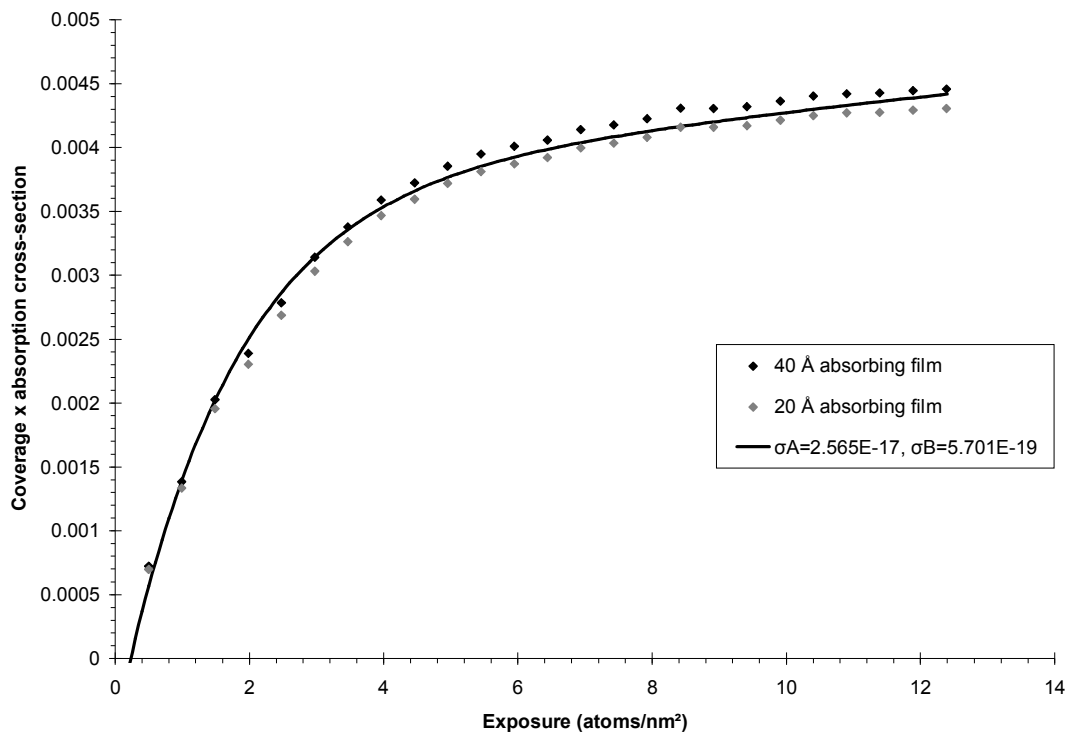


Figure 5.9: Plot of $n\sigma$ as a function of calcium deposition for MEH-PPV

Results for both 20 and 40 Å thick diffusion layers are shown in this graph. The best fit line is for the average of the two thicknesses, where the two absorption cross-sections have been found to be 3×10^{-17} and $6 \times 10^{-19} \text{ cm}^2$.

calculations should be representative for both polymers, given the similar refractive indices at the photon energy in question.¹¹⁷

Since the P3HT/Ca system is the simpler of the two, let's first examine the results for this before considering the MEH-PPV/Ca system. The assumption of different diffusion layer thicknesses does not significantly affect the calculations here. The best fit line on the average of the two sets of calculations has a slope of $9 \times 10^{-19} \text{ cm}^2$, which corresponds to the absorption cross-section. The fit is obviously not perfect: if we take tangents at the low exposure end and at the high exposure end, the cross-section would appear to change from $1.5 \times 10^{-18} \text{ cm}^2$ (at $\sim 2 \text{ atoms/nm}^2$) to $5.5 \times 10^{-19} \text{ cm}^2$ (at $\sim 12 \text{ atoms/nm}^2$). The cross-section obtained here is rather small: it corresponds to a Beer's Law molar extinction coefficient of $\sim 250 \text{ L}\cdot\text{mol}^{-1}\cdot\text{cm}^{-1}$. To put this number into perspective, the extinction coefficient for d-d transitions in metal complexes can be as large as $1000 \text{ L}\cdot\text{mol}^{-1}\cdot\text{cm}^{-1}$, while symmetry allowed charge transfer bands can have coefficients up to $50,000 \text{ L}\cdot\text{mol}^{-1}\cdot\text{cm}^{-1}$.¹¹⁸

How does the absorption cross-section for the MEH-PPV/Ca system compare with the P3HT/Ca system we have just discussed? We first note that the optical and calorimetric data for MEH-PPV both have exponential dependencies on calcium exposure. Since we argued previously that the calorimetric data shows two distinct reactions when calcium is deposited onto MEH-PPV where calcium atoms either react with the polymer or they react with calcium that is already on the surface, we propose that there too are two absorption cross-sections involved in the optical data, corresponding to the two products from the reactions. Information from the calorimetric data is therefore incorporated in determining the best fit $n\sigma$ line shown in **Figure 5.9**: we obtain the populations of the individual states from the 2-state model introduced in the calorimetry analysis, and use the two cross-sections as fitting parameters to the multilayer calculation. Recall from **Chapter 4.1** that the number of available empty binding sites, or site A in the previous discussion, n_A , is given by:

$$\frac{n_A}{n_0} = e^{\frac{-s_A \theta}{n_0}} \quad (4.5)$$

Continuing with the binding site labels used in the previous discussion, since a site B is generated when a site A becomes occupied, the total number of occupied site A, n'_A , is the number of available site B. Recall as well that the total number of available sites of any type is n_0 such that $n_A + n_B = n_0 = 1.7 \text{ nm}^{-2}$. The population of site A (equivalent to the amount of products from the first reaction) is thus:

$$n'_A = n_0 \left(1 - e^{\frac{-\theta}{n_0}} \right) \quad (5.15)$$

The sum of the two states' populations should add up to the amount of calcium deposited θ , which yields an expression for the population of site B (equivalent to the amount of products from the second reaction), n'_B :

$$n'_B = \theta - n_0 \left(1 - e^{\frac{-\theta}{n_0}} \right) \quad (5.16)$$

Using these populations, the best fit σ_A is $3 \times 10^{-17} \text{ cm}^2$, while the best σ_B is $6 \times 10^{-19} \text{ cm}^2$. The value for σ_B is roughly similar to the cross-section obtained for P3HT, as the similar slopes for P3HT and MEH-PPV at higher exposure indicates, and is attributable in all cases as due to condensation of calcium clusters.

It is very interesting that σ_A is much larger than σ_B . What may be the cause of this large absorption cross-section? If calcium is capable of n-doping the polymer, negative polarons would form, and new electronic states would appear inside the band gap, as indicated schematically in **Figure 5.10**.¹¹⁹ This figure also shows some

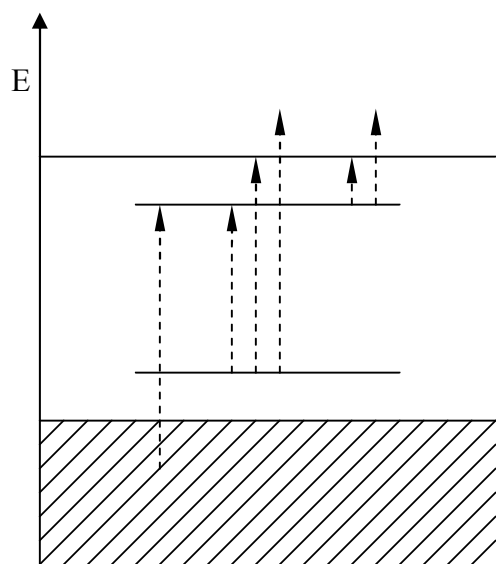


Figure 5.10: Schematic diagram of possible transitions, and thus absorption energies, for negative polarons

Recall that for a negative polaron the lower polaronic level is filled, while the upper is half-filled, such that transitions can potentially occur from the valence band to the upper polaronic level, from the lower level to the upper level or to the valence band, or from the upper level to the valence band.

of the potential optical transitions for the negative polaron.¹²⁰ The distance from the band edge is related to the polaronic relaxation energy,¹²¹ which is a small number: values in the literature range up to ~ 0.7 eV.¹²² The 1.85 eV photon energy used is 0.25 eV less than the MEH-PPV band gap of 2.1 eV,¹⁴ thus the absorption we observe may be due to polarons. The polaronic absorption cross section found by I. H. Campbell *et. al.*, where field-induced charges were introduced into MEH-PPV,¹²³ has been estimated to be no larger than to 1×10^{-16} cm², which compares quite well with our σ_A .

It is very exciting that our calorimetry data clearly correlates so well with the optical data, and that we might have a chemical probe of the photo-physical doping reaction. Combining the calorimetric and optical results, we propose the following chemical picture in regards to calcium deposition on MEH-PPV: calcium undergoes a redox reaction with MEH-PPV to form calcium cation and polymer anion. The electron-rich vinylene double bond in the polymer ion then acts as a ligand and interacts with the calcium ion. This chemistry agrees beautifully with the findings of V.-E.Choong *et. al.*, where DFT calculations indicate that calcium ions are located at the vinylene double bonds, with their electrons transferred onto the conjugated backbone.⁴⁴

Returning to P3HT, it is interesting that the cross-section is such a small value at 9×10^{-19} cm², since one might expect to be able to observe absorption due to polarons with this polymer's band gap of 2.2 eV.¹⁸ P. J. Brown *et. al.* have measured the cross-section due to polarons in P3HT, formed through field-induced charge injection, to be on the order of 10⁻¹⁶ cm²,¹²⁴ at 1.34 and 1.65 eV. The 1.65 eV signal in Brown's study decayed by $\sim 30\%$ by 1.85 eV, but there was nevertheless a reasonably strong absorption. The lack of absorption in our experiments thus appears to suggest that calcium deposition does not cause polaron formation. This is consistent with the calorimetric data showing no strong reaction of incident calcium atoms with the P3HT.

5.2. Xenon Lamp Studies

Spectroscopic experiments using a xenon lamp coupled with a monochromator were also carried out. However, before any *in situ* experiments were performed using the calorimeter, the absorptance spectra for the gold substrate and polymers were collected in an integrating sphere *ex situ* using the same light source and associated optics. The spectra are shown in **Figure 5.11**.

It is obvious that MEH-PPV shows a lot more absorption at 1.85 eV than P3HT. This is rather surprising, given that the two polymers share similar band gaps at 2.1 and 2.2 eV respectively.^{14,18} Calculations are thus carried out using a 3-phase vacuum-polymer-gold model, using the same equations as before with photon energy dependent refractive indices taken from the literature,^{94,95,96,116,117} to hopefully shed some light into this unexpected result. Polymer layer thickness is used here as a parameter to fit the observed spectra. As a check before fitting the experimental data with polymer film thickness as a parameter, a calculation with a polymer thickness of 0 Å is first carried out to verify that there is agreement between theory and experiment. This is shown in **Figure 5.12**. Comparisons between calculated and measured absorptances for MEH-PPV, P3HT and MEH-PPP are shown in **Figure 5.13**, **Figure 5.14** and **Figure 5.15** respectively.

There is good agreement between the calculated absorptance for a 20 nm polymer film and the observed MEH-PPV absorptance. This is therefore the thickness used for the calculations in the laser data discussion. This thickness reproduces accurately the rise of the absorption with increasing photon energy, as well as the dip after the absorption peak. However, the fit is not very good at the peak. It is interesting to note that the 10 nm calculation reproduces the feature in the data at ~2.5 eV, which is perhaps a consequence of the imaginary part of gold's dielectric constant having a “kink” at this photon energy.⁹⁶

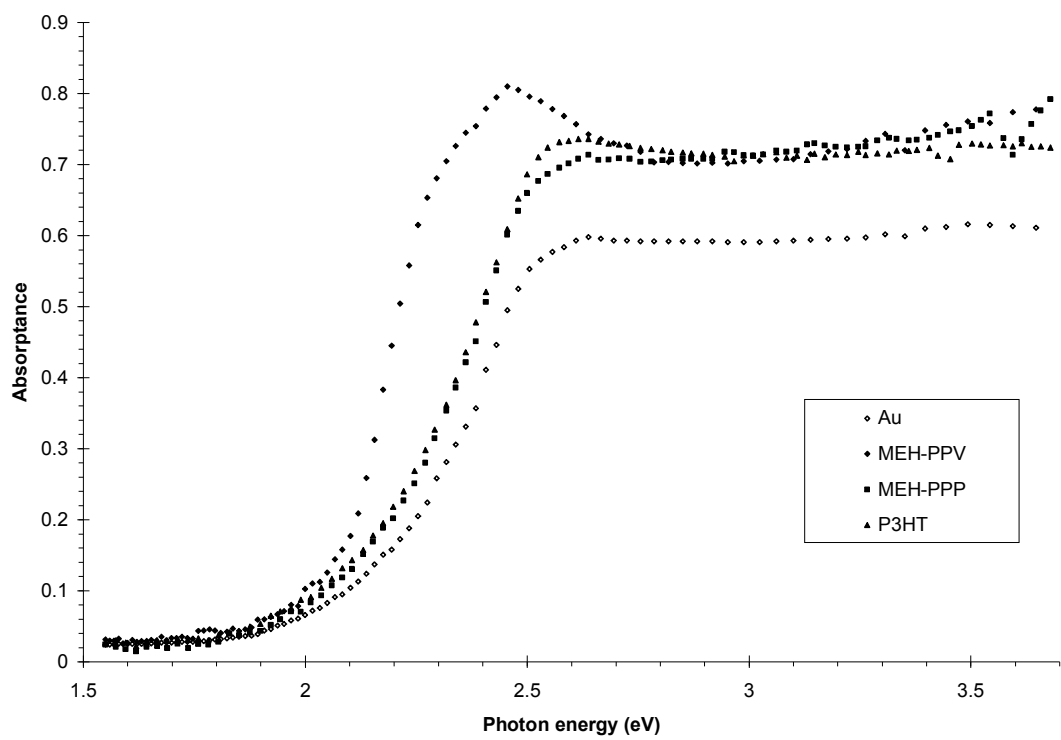


Figure 5.11: Absorptance spectra for the three polymers, as well as the gold substrate, as collected using an integrating sphere

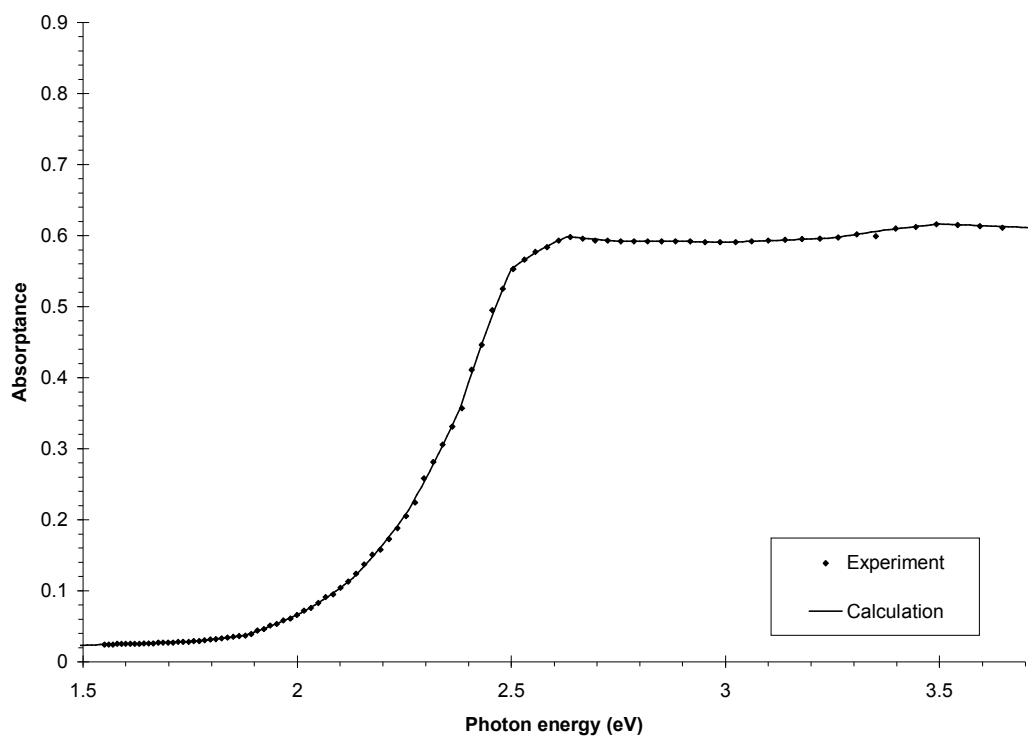


Figure 5.12: Comparison between measured absorptance of the gold substrate *ex situ* in integrating sphere and the calculation

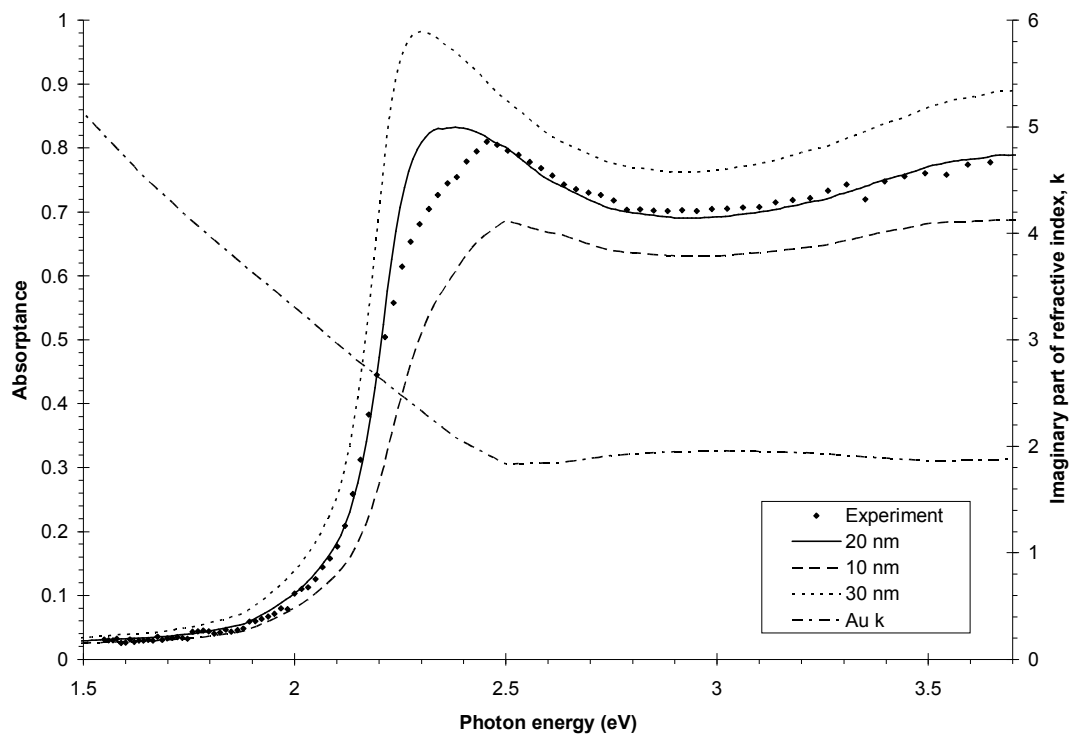


Figure 5.13: Comparison between measured MEH-PPV absorptance *ex situ* in integrating sphere and the best fit calculation

The best fit curve has a polymer thickness of 20 nm. Also shown are the calculated absorptances of 10 and 30 nm thick films. The imaginary part of gold's refractive, k , is shown as well to illustrate the location of the “kink”.

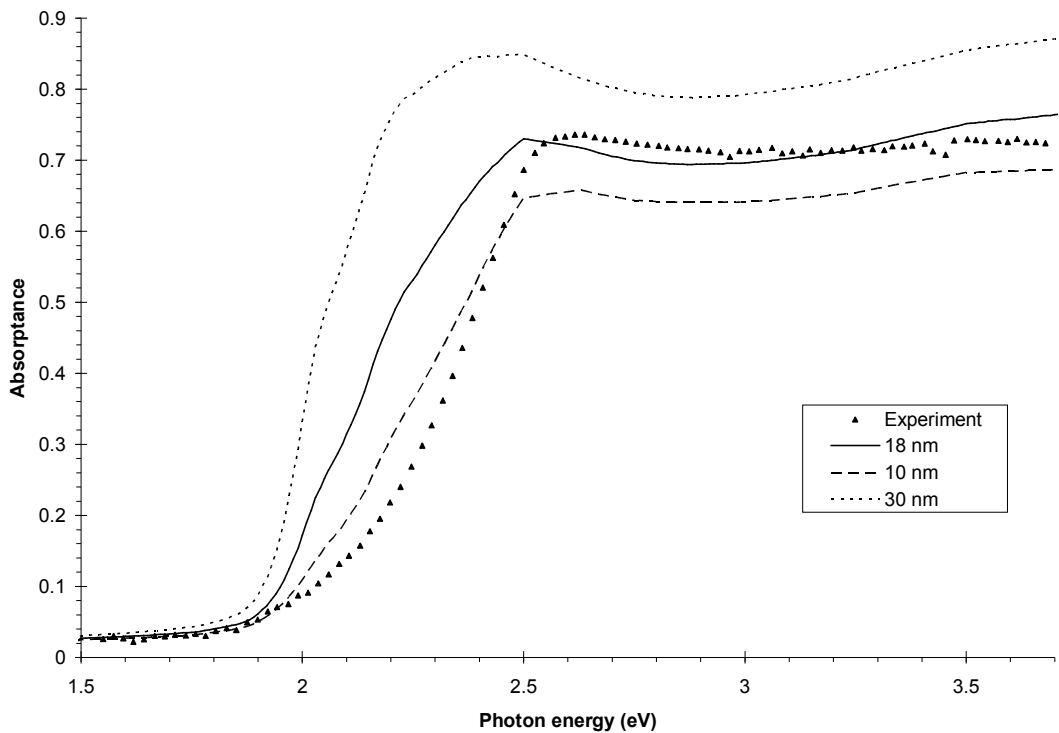


Figure 5.14: Comparison between measured P3HT absorptance *ex situ* in integrating sphere and calculation

The agreement is quite poor for this polymer: the absorption between 2 and 2.5 eV is much lower in the experimental data. The best fit is for an 18 nm thick polymer film, while calculated absorptances for 10 nm and 30 nm films are also included for comparison.

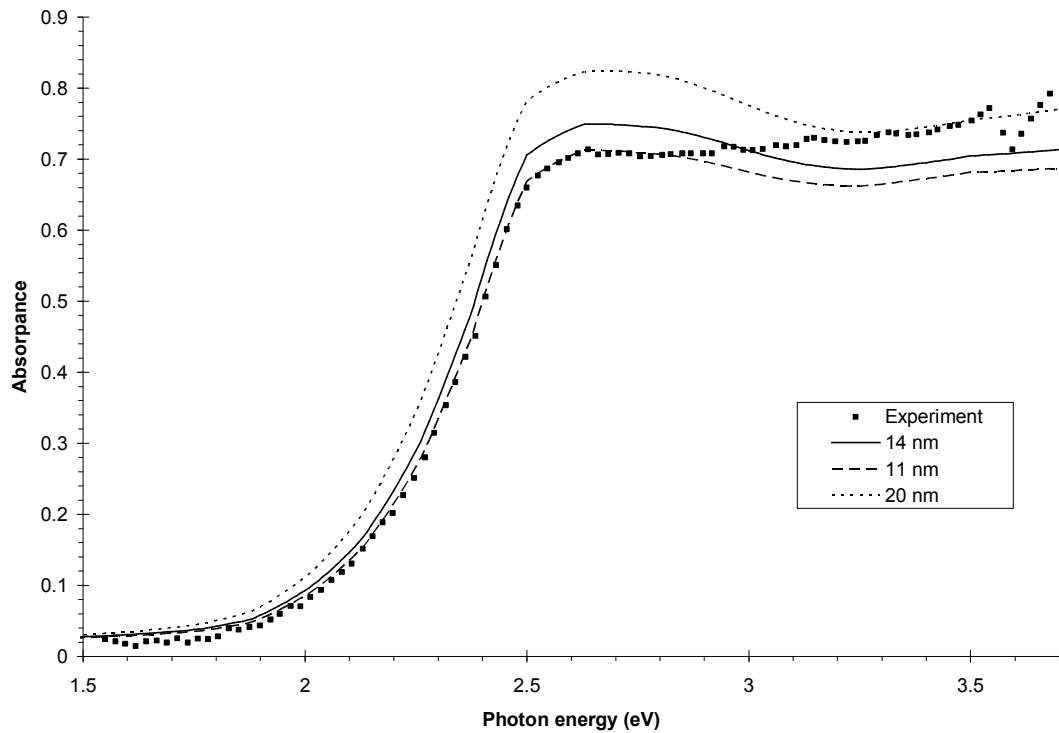


Figure 5.15: Comparison between measured MEH-PPP absorptance *ex situ* in integrating sphere and calculations for 11 nm, 14 nm (best fit), and 20 nm thick films

The fit is also poor for this polymer. However, the fit is based on the PPP polymer poly(*p*-phenylene-alt-co-*p*-2,5-dioctyloxyphenylene), since the refractive index for MEH-PPP appears to not have been published in the literature.

The agreement for P3HT is, on the contrary, quite poor. A thickness of 18 nm does match the high energy regime reasonably well, but the observed absorptance around the band gap region is significantly lower than the calculated values. While the most obvious reason for this observation would be that the P3HT did not adhere during spin-coating onto the substrate, a film was definitely present and visible to the eye. It should be noted that the MEH-PPV was a brightly coloured film, while the P3HT was very lightly coloured, even though one would expect the two materials to appear similar. There may be interfacial effects between P3HT and gold that are absent in MEH-PPV. Further studies will need to be carried out to determine the cause of this phenomenon.

The agreement for MEH-PPP is also quite poor. An 11 nm film is a good fit for photon energies below $\sim 2.7\text{ eV}$, but cannot reproduce the observed absorptance at higher energies, while a 20 nm film appears to be a good fit above $\sim 3.3\text{ eV}$, but overestimates the absorptance for all energies below. However, the inability to fit the experimental data is perhaps not unexpected, given that the refractive index used in the calculations is actually that of the PPP polymer poly(*p*-phenylene-alt-co-*p*-2,5-dioctyloxyphenylene), a polymer where there are side-chains only on every other phenyl ring, as well as having side-chains of different lengths from those in MEH-PPP. Indeed, the main absorption peak of this polymer is at 2.9 eV,¹¹⁷ which corresponds quite well to the location of the peaks in the calculations. The absorption peak for MEH-PPP is, however, at 3.8 eV according to the manufacturer, which is perhaps the reason for the observed rise in absorptance at the high energy end of the experimental data. Unfortunately it would require a significant effort in measuring the photon energy-dependent complex refractive index of MEH-PPP, which would be a major project in and of itself.

Regarding spectra recorded *in situ* after calcium deposition, the original idea of this exploratory work using a xenon lamp was to have stepwise calcium deposition with a full spectrum at each step to complement the laser studies. Unfortunately, the results

were erratic, likely due to the 20-30 minutes required to record each spectra, during which time the sample was exposed to background gases, as well as photo-degradation.^{125,126} Since both the calorimetry and laser data indicate that the majority of the reaction occurred before 4.5 atoms/nm², or 2 Å, of calcium exposure, we chose this dosage for the lamp experiments. The percentage absorptance changes as a function of photon energy for the three polymers are shown in **Figure 5.16**.

At the diode laser energy of 1.85 eV, the lamp data indicates an approximately 18% absorptance change for MEH-PPV; this is somewhat larger than the 11% seen in the laser diode experiments. There is essentially no absorptance change observed in the lamp experiments for MEH-PPP and P3HT, whereas 2% can be seen in the laser data. While it would have been ideal that the numbers from the two sets of experiments match perfectly, the lamp data nevertheless demonstrates qualitatively what is observed in the laser data. We deem the laser data to be more accurate since the time delay between deposition and measurement was minimal in these experiments; as well, a significantly better signal-to-noise ratio was possible compared to the lamp experiments due to the higher and more stable light intensity the laser provided.

The most noticeable feature in **Figure 5.16** is that only MEH-PPV absorbs appreciably differently after the deposition of 4.5 atoms/nm² of calcium, with increased absorption at energies below ~2.2 eV, which is the sub-band gap region of this polymer. It has been reported in the literature that an absorption band appears at 1.6 eV when charge carriers are injected into MEH-PPV;¹²³ the absorption seen in the lamp experiment is likely to be the same band, which further consolidates our conclusion that polarons formed during calcium deposition on MEH-PPV.

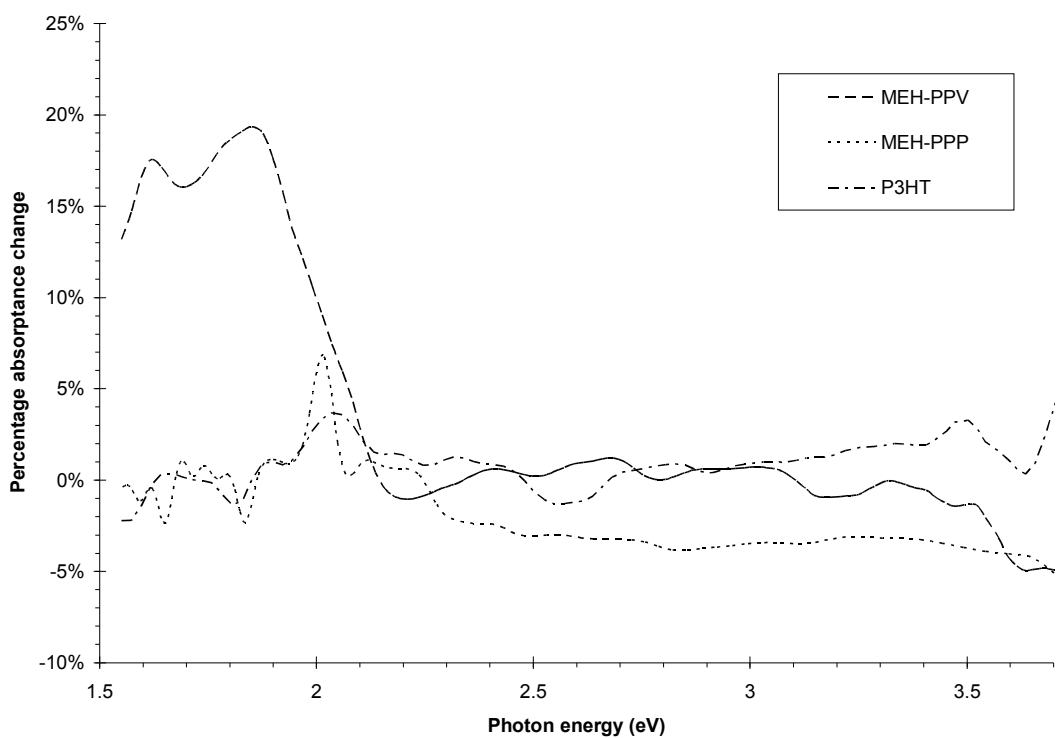


Figure 5.16: Percentage absorptance change upon the deposition of 4.5 atoms/nm² of calcium for all three polymers as a function of photon energy
Only MEH-PPV can be observed to have a significant change in absorptance. As a reminder, the laser diode energy is 1.85 eV.

5.3. Summary of Optical Studies

We have demonstrated theoretically (the full derivation is presented in **Appendix 1**) that in the thin film limit where a growing overlayer has a thickness much smaller than the wavelength of the light incident on the system, the change in absorptance is linear with the overlayer's thickness. This is true for any number of underlying films, as long as these films' refractive indices/dielectric functions do not change in the course of the overlayer growth. This linear absorptance change is strictly a result of interference effects within the multi-layer system, and does not require an absorbing overlayer. However, if the overlayer is not absorbing, at least one film in the underlying multilayer must be absorbing, or the system will just be completely non-absorbing regardless of the overlayer thickness, as intuition would suggest.

We have presented exploratory work utilizing the calorimeter sensor as a detector for changes in optical absorption using the laser energy of 1.85 eV. In the case of calcium deposition on MEH-PPV we observe a large optical cross section of 3×10^{-17} cm² per incident atom, which we attribute to polaron formation.

In the case of P3HT and MEH-PPP, we observe a linear change of absorbance with exposure, which indicates constant sticking of calcium, most reasonably unit sticking. However attempts to fit the absorbance with models assuming unit sticking failed.

The optical behaviour of MEH-PPP during Ca deposition was similar to that of P3HT. While we suspect the polymer may be doped upon deposition, since the calorimetric data suggests similar chemistry as for MEH-PPV, 1.85 eV is too low an energy to probe the band-edge region of this polymer, whose band gap is 3.8 eV.

We have presented further exploratory work in this chapter where absorption spectra have been collected over the visible spectrum of wavelengths. Even though the signal-to-noise ratio is significantly worse than the laser experiments, the lamp data nevertheless reproduced qualitatively the laser results. There is essentially no

absorptance change for MEH-PPP and P3HT after the deposition of 4.5 atoms/nm² of calcium, while an absorption which we believe is due to polarons is present below ~2.1 eV for MEH-PPV.

The measured absorptances for the 3 pristine polymers show varying degrees of discrepancies from calculated values based on refractive indices found in the literature. Whereas there is a reasonably good agreement for MEH-PPV, the band gap region cannot be described accurately for P3HT. This lack of absorption around the band gap has also been observed visually, where there is a lack of colour on the spin-coated polymer film. Barring decomposition of the polymer, this lack of absorption may be due to interactions between P3HT and the gold substrate. The agreement is also poor for MEH-PPP, but this is not entirely unexpected: since there is a lack of optical studies in the literature on MEH-PPP, the calculations have been based upon a copolymer between PPP and PPV.

6. Conclusion and Proposals for future work

There were in practice two parts to this project. The first part was to use the calorimeter for its original purpose in measuring the heat of reaction during polymer metallization. Most of this work centred around the benchmark PLED material MEH-PPV. By comparison with MEH-PPP, we propose that the binding site for calcium on MEH-PPV is the vinylene moiety on the polymer backbone. The heat of reaction at these sites is 360 kJ/mol, and they are occupied at a projected areal density of 1.7 sites/nm². Incident calcium atom is likely to be immobilized once it encounters a reaction site, which can either be an empty binding site, or an occupied binding site that then acts as a nucleation site for calcium island/overlayer growth.

Calorimetry experiments were also performed on MEH-PPP and P3HT, which showed more complex behaviour. A model involving two distinct binding energies and three reaction steps has been suggested as a plausible explanation to the behaviour seen in MEH-PPP, while the P3HT data cannot be modeled mathematically at the present time without further experiments using other techniques as guidance. The model for MEH-PPP, if correct, suggests that the binding sites have a projected areal density of 3.5 sites/nm², with a first binding energy of 200 kJ/mol and a second binding energy of 360 kJ/mol. The binding energies can be explained if the phenyl rings on the polymer backbone are the reaction sites. In this picture, an unreacted phenyl ring interacts with calcium via one of the three double bonds. This interaction requires energy to overcome the aromatic stabilization, which is on the order of 150 kJ/mol; thus the expected reaction heat for the first calcium would be 360 kJ/mol (as measured for MEH-PPV) offset by this amount, which is comparable to the 200 kJ/mol obtained.

While we have not proposed a model that can accurately describe the P3HT calorimetric data, it is consistent with calcium island growth without a strong interaction with the polymer. However, the reaction heat profile could also be due to

the formation of an overlayer which requires significant alterations of the polymer's chemical structure, such as the formation of a calcium sulphide film, during which sulphur atoms are abstracted from the polymer's backbone. Nevertheless, calcium island growth is the more likely explanation, since data from the laser studies also appears to support this hypothesis.

The second part of this project involved the expansion of the calorimeter's capability to measuring optical absorbance, formally absorptance, initially using a laser diode, and subsequently expanded further with a lamp and scanning monochromator. It has been demonstrated quite successfully that the calorimeter is capable of functioning as a spectrometric sensor. Using MEH-PPV as the test case, it has been determined, through calculations using a thin film optical model, that the absorption cross-section for polaronic species in this polymer is $\sim 3 \times 10^{-17}$ cm², comparable to literature reports. With further development the laser diode technique can potentially be used as a real-time coverage monitor concurrent with calorimetric studies.

Throughout this thesis, we have reported the amount of calcium deposited in terms of exposure. It is important that we upgrade our calorimeter to measure sticking probabilities in real time so as to gain information on the reaction heats as a function of the amount of calcium *reacted*, since this is important information in the understanding of the chemistry of these reactions.

For other future work, it would be very interesting to study the variations of binding site densities on MEH-PPV and MEH-PPP due to sample preparation methods, since the polymer film morphology can be expected to vary widely depending on factors such as solution concentration, spin speeds, and indeed also on whether the sample was dip cast, spin coated, deposited as polymer chains or cured *in situ*, etc. This is especially important in terms of doping, for a higher density of binding sites means a higher degree of doping, which might significantly alter device efficiency.

Future work could also include the study of the interaction between calcium and other technologically important polymers. Given that side groups can be used to tailor the photoluminescence colour of polymers as well as alter their physical properties, such as solubility, of importance to PLED device fabrication, it would be interesting to study PPV and PPP polymers with different side groups to determine if they would interfere with the reactions seen in MEH-PPV and MEH-PPP. Other classes of PLED polymers with different backbones, such as polyfluorene, where the repeat unit has two benzene rings fixed in a coplanar geometry by a bridging 5-member ring, and the related polyfluorene vinylene, would also be interesting systems to study, especially given the backbone reactivities seen in the polymers examined in this thesis.

One could also consider broadening the program to include the deposition of non-metallic materials that are of technological importance onto semiconducting polymers. One such material that was contemplated was lithium fluoride, which has been found to significantly increase OLED performance when an appropriate layer is deposited before the low work function cathode.^{127,128,129} As well, there is no reason the calorimeter should only be used for polymers; since it is already equipped with an effusion cell, films of molecular OLED materials can be grown using the cell, which can subsequently be studied just as has been done for polymers.

Bibliography

1. P.E. Burrows, G. Gu, V. Bulović, Z. Shen, S. R. Forrest, and M. E. Thompson, *IEEE Trans. Elec. Dev.* **44** (1997) 1188
2. R. H. Friend, R. W. Gymer, A. B. Holmes, J. H. Burroughes, R. N. Marks, C. Taliani, D. D. C. Bradley, D. A. Dos Santos, J. L. Brédas, M. Lögdlund, and W. R. Salaneck, *Nature* **397** (1999) 121
3. A. Kraft, A. C. Grimsdale, and A. B. Holmes, *Angew. Chem. Int. Ed. Engl.* **37** (1998) 402
4. H. Sirringhaus, T. Kawase, R. H. Friend, T. Shimoda, M. Inbasekaran, W. Wu, and E. P. Woo, *Science* **290** (2000) 2123
5. A. Pron, and P. Rannou, *Prog. Polym. Sci.* **27** (2002) 135
6. H. Sirringhaus, N. Tessler, R. H. Friend, *Science* **280** (1998) 1741
7. R. E. Martin, F. Geneste, and A. B. Holmes, *C. R. Acad. Sci. Paris 1 Série IV* (2000) 447
8. Q. Pei, and Y. Yang, *J. Am. Chem. Soc.* **118** (1996) 7416
9. T. Ahn, S.G-. Lee, and H.-K. Shim, *Opti. Mater.* **21** (2002) 191
10. L. C. Lopez, P. Strohriegl, and T. Stübinger, *Macromol. Chem. Phys.* **203** (2002) 1926
11. P. K. H. Ho, D. S. Thomas, R. H. Friend, and N. Tessler, *Science* **285** (1999) 233
12. K. S. Whitehead, M. Grell, D. D. C. Bradley, M. Jandke, and P. Strohriegl, *Appl. Phys. Lett.* **76** (2000) 2946
13. I. D. Parker, *J. Appl. Phys.* **75** (1994) 1656
14. R. Cervini, X.-C. Li, G. W. C. Spencer, A. B. Holmes, S. C. Moratti, and R. H. Friend, *Synth. Met.* **84** (1997) 359
15. F. Bartha, I. A. Howard, P. Geerlings, C. Van Alsenoy, D. Vanderzande, T. J. Cleiji, F. Bogár, *Int. J. Quant. Chem.* **106** (2006) 1912

16. N. H.-S. Lee, Z.-K. Chen, S.-J. Chua, Y.-H. Lai, W. Huang, *Thin Solid Films* **363** (2000) 106
17. B.-H. Wang, J. Yin, M. Xue, J. Wang, G. Zhong, and X. Ding, *Thin Solid Films* **424** (2003) 186
18. M. Onoda, K. Tada, A. A. Zakhidov, K. Yoshino, *Thin Solid Films* **331** (1998) 76
19. U. Salzner, J. B. Lagowski, P. G. Pickup, R.A. Poirier, *Synth. Met.* **96** (1998) 177
20. S. Janietz, D. D. C. Bradley, M. Grell, C. Giebel, M. Inbasekaran, and E. P. Woo, *Appl. Phys. Lett.* **73** (1998) 2453
21. Y. He, J. K. Politis, H. Cheng, M. D. Curtis, and J. Kanicki, *IEEE Trans. Electron Dev.* **44** (1997) 1282
22. H. Plank, R. Güntner, U. Scherf, and E. J. W. List, *Soft Matter* **3** (2007) 713
23. W. R. Salaneck, and M. Löglund, *Polym. Adv. Technol.* **9** (1998) 419
24. L. Ke, S.-J. Chua, K. Zhang, and N. Yakovlev, *Appl. Phys. Lett.* **80** (2002) 2195
25. Y. Sohn, Ph.D. thesis, University of British Columbia (2004)
26. *CRC Handbook of Chemistry and Physics, Internet Version 2007, 87th Ed.* <http://www.hbcpnetbase.com/>, D. R. Lide, ed., Taylor and Francis, Boca Raton, Florida (2007)
27. M. Königstein, and C. R. A. Catlow, *J. Solid State Chem.* **140** (1998) 103
28. Information from manufacturer, e.g.
<http://www.solvaychemicals.us/products/productshidden/0,,40550-2-0,00.htm>
29. T. P. Hanusa, *Chem. Rev.* **93** (1993) 1023
30. R. Zerger, and G. Stucky, *J. Organomet. Chem.* **80** (1974) 7
31. K. Mashima, H. Sugiyama, N. Kanehisa, Y. Kai, H. Yasuda, and A. Nakamura, *J. Am. Chem. Soc.* **116** (1994) 6977
32. T. P. Hanusa, *Coord. Chem. Rev.* **210** (2000) 329

33. M. J. Harvey, T. P. Hanusa, and V. G. Yong, Jr., *Angew. Chem. Int. Ed.* **38** (1999) 217
34. K. Mochida, Y. Hiraga, H. Takeuchi, and H. Ogawa, *Organomet.* **6** (1987) 2293
35. P. R. Markles, T. Nomoto, G. Schat, O. S. Akkerman, and F. Bickelhaupt, *Organomet.* **10** (1991) 3826
36. S. A. Kinsley, A. Streitwieser, Jr., and A. Zalkin, *Organomet.* **4** (1985) 52
37. P. Dannetun, M. Löglund, C. Fredriksson, C. Fauquet, S. Stafström, C. W. Spangler, J. L. Bredás, and W. R. Salaneck, *J. Chem. Phys.* **100** (1994) 6765
38. P. Dannetun, M. Fahlman, C. Fauquet, K. Kaerijama, Y. Sonoda, R. Lazzaroni, J. L. Bredás, and W. R. Salaneck, *Synth. Met.* **67** (1994) 133
39. A. J. Heeger, *Angew. Chem. Int. Ed.* **40** (2001) 2591
40. J. L. Bredás and G. B. Street, *Acc. Chem. Res.* **18** (1985) 309
41. T. B. Lynge, and T. G. Pedersen, *Comp. Met. Sci.* **30** (2004) 212
42. J. Birgerson, M. Fahlman, P. Bröms, and W. R. Salaneck, *Synth. Met.* **80** (1996) 125
43. R. Lazzaroni, M. Löglund, A. Calderone, J. L. Brédas, P. Dannetun, C. Fauquet, C. Fredriksson, S. Strafström, and W. R. Salaneck, *Synth. Met.* **71** (1995) 2159
44. V.-E. Choong, Y. Park, B. R. Hsieh, and Y. Gao, *J. Phys. D: Appl. Phys.* **30** (1997) 1421
45. G. G. Andersson, W. J. H. van Gennip, J. W. Niemantsverdriet, and H. H. Brongersma, *Chem. Phys.* **278** (2002) 159
46. Y. Gao, K. T. Park, and B. R. Hsieh, *J. Appl. Phys.* **73** (1993) 7894
47. K. Honda, Y. Furukawa, K. Furuya, H. Torii, and M. Tasumi, *J. Phys. Chem. A* **106** (2002) 3587
48. Y. Furukawa, H. Ohtsuka, and M. Tasumi, *Synth. Met.* **55** (1993) 516
49. Y. Furukawa, H. Ohtsuka, M. Tasumi, I. Wataru, T. Kanbara, and T. Yamamoto, *J. Raman. Spectrosc.* **24** (1993) 551

50. N. Koch, A. Rajagopal, J. Ghijsen, R. L. Johnson, G. Leising, and J.-J. Pireaux, *J. Phys. Chem. B* **104** (2000) 1434
51. A. Rajagopal, N. Koch, J. Ghijsen, R. L. Johnson, G. Leising, and J.-J. Pireaux, *J. Appl. Phys.* **87** (2000) 1331
52. J. Murr, and Ch. Ziegler, *Phys. Rev. B* **57** (1998) 7299
53. R. Mikalo, and D. Schmeißer, *Synth. Met.* **127** (2002) 273
54. K. Z. Xing, M. Fahlman, M. Löglund, M. Berggren, O. Inganäs, M. R. Andersson, M. Boman, S. Stafström, G. Iucci, P. Bröms, N. Johansson, and W. R. Salaneck, *Synth. Met.* **80** (1996) 59
55. M. Boman, S. Strafström, and J. L. Brédas, *J. Chem. Phys.* **97** (1992) 9144
56. P. Dannetun, M. Boman, S. Strafström, W. R. Salaneck, R. Lazzaroni, C. Fredriksson, J. L. Brédas, R. Zamboni, and C. Taliani, *J. Chem. Phys.* **99** (1993) 664
57. S. Černý, *Surf. Sci. Rep.* **26** (1996) 1
58. C. E. Borroni-Bird and D. A. King, *Rev. Sci. Instrum.* **62** (1991) 2177
59. A. Stuck, C. E. Wartnaby, Y. Y. Yeo, J. T. Stuckless, N. Al-Sarraf, D. A. King, *Surf. Sci.* **349** (1996) 229
60. J. T. Stuckless, N. A. Frei, and C. T. Campbell, *Rev. Sci. Instrum.* **69** (1998) 2427
61. H. J. Coufal, R. K. Grygier, D. E. Horne, and J. E. Fromm, *J. Vac. Sci. Technol. A* **5** (1987) 2875
62. R. Murdey, Ph.D. thesis, University of British Columbia (2003)
63. R. Murdey, S. J. S. Liang, and J. T. Stuckless, *Rev. Sci. Instrum.* **76** (2005) 023911
64. L. S. Liao, L. F. Cheng, M. K. Fung, C. S. Lee, S. T. Lee, M. Inbasekaran, E. P. Woo, and W. W. Wu, *Chem. Phys. Lett.* **325** (2000) 405
65. L. Ke, S. F. Lim, and S. J. Chua, *J. Polym. Sci., Part B: Polym. Phys.* **39** (2001) 1697

66. S. Cros, M. Firon, S. Lenfant, P. Trouslard, and L. Beck, *Nucl. Instrum. Methods Phys. Res., Sect. B* **251** (2006) 257
67. P. Bröms, J. Birgersson, N. Johansson, M. Löglund, and W. R. Salaneck, *Synth. Met.* **74** (1995) 179
68. J. Zhu, P. Goetsch, N. Ruzycki, and C. T. Campbell, *J. Am. Chem. Soc.* **129** (2007) 6432
69. J. M. Bharathan, and Y. Yang, *J. Appl. Phys.* **84** (1998) 3207
70. V. Choong, Y. Park, Y. Gao, T. Wehrmeister, K. Müllen, B. R. Hsieh, and C. W. Tang, *Appl. Phys. Lett.* **69** (1996) 1492
71. J. T. Stuckless, D. E. Starr, D. J. Bald, and C. T. Campbell, *Phys. Rev. B* **56** (1997) 13496
72. V. Zaporojtchenko, K. Behnke, A. Thran, T. Strunkus, and F. Faupel, *Appl. Surf. Sci.* **144-145** (1999) 355
73. E. Ettedgui, H. Razafitrimo, K. T. Park, Y. Gao, and B. R. Hsieh, *J. Appl. Phys.* **75** (1994) 7526
74. E. Ettedgui, H. Razafitrimo, Y. Gao, B. R. Hsieh, W. A. Feld, and M. W. Ruckman, *Phys. Rev. Lett.* **76** (1996) 299
75. V.-E. Choong, Y. Park, Y. Gao, T. Wehrmeister, K Müllen, B. R. Hsieh, and C. W. Tang, *J. Vac. Sci. Technol. A* **15** (1997) 1745
76. V.-E. Choong, M. G. Mason, C. W. Tang, and Y. Gao, *App. Phys. Lett.* **72** (1998) 2689
77. L. S. Liao, L. F. Cheng, M. K. Fung, C. S. Lee, S. T. Lee, M. Inbasekaran, E. P. Woo, and W. W. Wu, *Phys. Rev. B* **62** (2000) 10004
78. J. M. Zhao, S. T. Zhang, X. J. Wang, Y. Q. Zhan, X. Z. Wang, G. Y. Zhong, Z. J. Wang, X. M Ding, W. Huang, and X. Y. Hou, *Appl. Phys. Lett.* **84** (2004) 2913
79. D. A. Clymer, and M. A. Matin, *Microwave Opt. Technol. Lett.* **48** (2006) 2070
80. F. J. Zhang, A. Vollmer, J. Zhang, Z. Xu, J. P. Rabe, and N. Koch, *Organic Electronics* **8** (2007) 606

81. C. Y. Yang, F. Hide, M. A. Díaz-García, A. J. Heeger, and Y. Cao, *Polymer* **39** (1998) 2299
82. F. J. J. Janssen, L. J. van IJzendoom, A. W. Denier van der Gon, M. J. A. de Voigt, and H. H. Brongersma, *Phys. Rev. B* **70** (2004) 165425
83. R. Murdey, J. T. Stuckless, *J. Am. Chem. Soc.* **125** (2003) 3995
84. S. A. Kafafi, *Chem. Phys. Lett.* **169** (1990) 561
85. L. Andrews, G. V. Chertihin, C. A. Thompson, J. Dillon, S. Byrne, and C. W. Bauschlicher, Jr., *J. Phys. Chem.* **100** (1996) 10088
86. J. Drowart, G. Exsteen, and G. Verhaegen, *Trans. Faraday Soc.* **60** (1964) 1920
87. J. A. Irvin, and P. J. Dagdigian, *J. Chem. Phys.* **73** (1980) 176
88. C. W. Bauschlicher, Jr., *Chem. Phys. Lett.* **94** (1983) 366
89. *Organic Chemistry 4th Ed.*, J. McMurry, Brooks/Cole Publishing Company, Pacific Grove (1996)
90. R. Resnel, N. Koch, F. Meghdadi, G. Leising, L. Athouel, G. Froyer, and F. Hofer, *Cryst. Res. Technol.* **36** (2001) 47
91. D. E. Starr, D. J. Bald, J. E. Musgrove, J. T. Ranney, and C. T. Campbell, *J. Chem. Phys.* **114** (2001) 3752
92. S. F. Diaz, J. F. Zhu, J. J. W. Harris, P. Goetsch, L. R. Merte, and C. T. Campbell, *Surf Sci* **598** (2005) 22
93. *Optical Properties of Thin Solid Films*, O. S. Heavens, Dover Publications, New York (1991)
94. C. M. Ramsdale, and N. C. Greenham, *J. Phys. D: Appl. Phys.* **36** (2003) L29
95. U. Zhokhavets, G. Gobsch, H. Hoppe, and N. S. Sariciftci, *Thin Solid Films* **451-452** (2004) 69
96. P. B. Johnson, and R. W. Christy, *Phys. Rev. B* **6** (1972) 4370
97. O. Levy, D. Stroud, *Phys Rev B* **56** (1997) 8035
98. I. J. Youngs, N. Bowler, K. P. Lymer, and S. Hussain, *J. Phys. D: Appl. Phys.* **38** (2005) 188

99. H. Du, H. Chen, J. Gong, T. G. Wang, C. Sun, S. W. Lee, and L. S. Wen, *Appl. Surf. Sci.* **233** (2004) 99
100. J. P. Petrakian, A. R. Cathers, J. E. Parks, R. A. MacRae, T. A. Callcott, and E. T. Arakawa, *Phys Rev B* **21** (1980) 3043
101. M.-L. Thèye, *Phys Rev B* **2** (1970) 3060
102. R. B. Somoano, and J. C. Thompson, *Phys. Rev. A* **1** (1970) 376
103. R. Y. Koyama, N. V. Smith, and W. E. Spicer, *Phys. Rev. B* **8** (1973) 2426
104. V. N. Pustovit, G. A. Niklasson, *J. Appl. Phys.* **90** (2001) 1275
105. P. Zhou, S.-Y. Wang, J. Li, R.-J. Zhang, H.-Y. You, Z.-C. Shen, and L.-Y. Chen, *Thin Solid Films* **455-456** (2004) 157
106. H. E. Bennett, J. M. Bennett, E. J. Ashley, and R. J. Motyka, *Phys. Rev.* **165** (1968) 755
107. N. M. Miskovsky, and P. H. Cutler, *Phys. Rev. B* **5** (1972) 1265
108. S. R. Nagel, and S. E. Schnatterly, *Phys. Rev. B* **9** (1974) 1299
109. S. R. Nagel, and S. E. Schnatterly, *Phys. Rev. B* **12** (1975) 6002
110. *Solid State Physics*, N. W. Ashcroft, N. D. Mermin, Saunders College, Philadelphia (1976)
111. J. Marfaing, and R. Rivoira, *Phys. Rev. B* **15** (1977) 745
112. C. Lopez-Rios, and C. B. Sommers, , *Phys. Rev. B* **12** (1975) 2181
113. T. W. H. Oates, and A. Mücklich, *Nanotechnology* **16** (2005) 2606
114. G. Nagy, and A. V. Walker, *J. Phys. Chem. C* **111** (2007) 8543
115. N. Daldosso, D. Navarro-Urrios, M. Melchiorri, L. Pavesi, C. Sada, F. Gourbilleau, and R. Rizk, *Appl. Phys. Lett.* **88** (2006) 161901
116. M. Tammer, and A. P. Monkman, *Adv. Mater.* **14** (2002) 210
117. M. Losurdo, G. Bruno, and E. A. Irene, *J. Appl. Phys.* **94** (2003) 4923

118. *Inorganic Chemistry 2nd Ed.*, C. E. Housecroft, and A. G. Sharpe, Pearson Education Limited, Essex (2005)
119. A. J. Heeger, S. Kivelson, J. R. Schrieffer, W.-P. Su, *Rev. Mod. Phys.* **60** (1988) 781
120. Y. Furukawa, *Synth. Met.* **69** (1995) 629
121. A. Moliton, and R. C. Hiorns, *Polym. Int.* **53** (2004) 1397
122. C. T. Tengstedt, W. Osikowicz, W. R. Salaneck, I. D. Parker, C.-H. Hsu, and M. Fahlman, *Appl. Phys. Lett.* **88** (2006) 053502
123. I. H. Campbell, D. L. Smith, C. J. Neef, and J. P. Ferraris, *Phys. Rev. B* **64** (2001) 035203
124. P. J. Brown, H. Sirringhaus, M. Harrison, M. Shkunov, and R. H. Friend, *Phys. Rev. B* **63** (2001) 125204
125. D. G. J. Sutherland, J. A. Carlisle, P. Elliker, G. Fox, T. W. Hagler, I. Jimenez, H. W. Lee, K. Pakbaz, L. J. Terminello, S. C. Williams, F. J. Himpsel, D. K. Shuh, W. M. Tong, J. J. Jia, T. A. Callcott, and D. L. Ederer, *Appl. Phys. Lett.* **68** (1996) 2046
126. M. Atreya, S. Li, E. T. Kang, K. G. Neoh, Z. H. Ma, K. L. Tan, and W. Huang, *Polym. Degrad. Stabil.* **65** (1999) 287
127. L. S. Hung, C. W. Tang, and M. G. Mason, *Appl. Phys. Lett.* **70** (1997) 152
128. G. E. Jabbour, Y. Kawabe, S. E. Shaheen, J. F. Wang, M. M. Morrell, B. Kippelen, and N. Peyghambarian, *Appl. Phys. Lett.* **71** (1997) 1762
129. S. E. Shaheen, G. E. Jabbour, M. M. Morrell, Y. Kawabe, B. Kippelen, N. Peyghambarian, M.-F. Nabor, R. Schlaf, E. A. Mash, and N. R. Armstrong, *J. Appl. Phys.* **84** (1998) 2324
130. J. D. E. McIntyre, and D. E. Aspnes, *Surf. Sci.* **24** (1971) 417

Appendix 1

Because of interference effects, the field strength of the light passing through a thin film does not decay exponentially throughout the thickness of the film as would be the case for an unbounded medium. The objective of this appendix is to demonstrate that the growth of an overlayer, regardless of it being absorbing or non-absorbing, leads a linear behaviour in percentage absorptance. This discussion will be structured as follows: general expressions related to electromagnetic wave propagation will first be presented, followed by a discussion of a simple 3-phase system, and finally a discussion of general multi-phase systems. It will be shown that a linear percentage absorptance change as a function of overlayer thickness can be expected for systems with any number of bounded phases between overlayer and substrate, in the limit that the overlayer is thin compared to the incident light's wavelength, and that none of the buried phases' optical properties change during the growth of the overlayer. This is a noteworthy extension of what is in the literature, which as far as we are aware has been demonstrated for 3 phases only.^{93,130}

The propagation of light in isotropic media is well known: it is governed by Maxwell's Equations:

$$\nabla \cdot \epsilon \vec{E} = 4\pi\rho \quad (\text{A1.1})$$

$$\nabla \cdot \mu \vec{H} = 0 \quad (\text{A1.2})$$

$$\nabla \times \vec{E} = -\frac{\mu}{c} \frac{\partial \vec{H}}{\partial t} \quad (\text{A1.3})$$

$$\nabla \times \vec{H} = \frac{4\pi\sigma\vec{E}}{c} + \frac{\epsilon}{c} \frac{\partial \vec{E}}{\partial t} \quad (\text{A1.4})$$

where ϵ is the electric permittivity, ρ is the electric charge density, μ is the magnetic permittivity, σ is the conductivity, and c is the speed of light. Note that as written,

these equations are all expressed in the centimetre-gram-second system. Furthermore, electrical quantities are in electrostatic units such that there is no proportionality constant in Coulomb's Law:

$$\vec{F} = \frac{q_1 q_2}{|r|^3} \vec{r} \quad (\text{A1.5})$$

while magnetic quantities are in electromagnetic units such that there is no proportionality constant in the Biot-Savart Law:

$$\vec{B} = \frac{q \vec{v} \times \vec{r}}{|r|^3} \quad (\text{A1.6})$$

In order to obtain expressions for the electric and magnetic fields, one should note that the electric and magnetic field vectors are related to each other by the curl operator. Thus, the curl of the curl of either vector would separate out the dependence of the vectors from one another. Thus, using the mathematical identity:

$$\nabla \times \nabla \times \vec{F} = \nabla \cdot \nabla \cdot \vec{F} - \nabla^2 \vec{F} \quad (\text{A1.7})$$

and applying Maxwell's Equations, equation A1.8 can be written for $\vec{F} = \vec{E}$ and A1.9 for $\vec{F} = \vec{H}$:

$$-\frac{\mu}{c} \frac{\partial}{\partial t} (\nabla \times \vec{H}) = \nabla \cdot \frac{4\pi\rho}{\epsilon} - \nabla^2 \vec{E} \quad (\text{A1.8})$$

$$\frac{4\pi\sigma}{c} (\nabla \times \vec{E}) + \frac{\epsilon}{c} \frac{\partial}{\partial t} (\nabla \times \vec{E}) = -\nabla^2 \vec{H} \quad (\text{A1.9})$$

Applying Maxwell's equations once more on equations A1.8 and A1.9 followed by rearrangement yields wave equations for the electric and magnetic field vectors:

$$\frac{\epsilon\mu}{c^2} \frac{\partial^2 \vec{E}}{\partial t^2} + \frac{4\pi\mu\sigma}{c^2} \frac{\partial \vec{E}}{\partial t} = \nabla^2 \vec{E} \quad (\text{A1.10})$$

$$\frac{\epsilon\mu}{c^2} \frac{\partial^2 \vec{H}}{\partial t^2} + \frac{4\pi\mu\sigma}{c^2} \frac{\partial \vec{H}}{\partial t} = \nabla^2 \vec{H} \quad (\text{A1.11})$$

If light travels along the z-axis, and we assign the associated electric field to be along the x-axis, the following wave solution can be written, with E being the amplitude of the wave's electric field, ω being the angular frequency of the wave, n being the refractive index of the medium through which the wave is propagating, λ being the wavelength, and \hat{x} being the unit vector along the x-axis:

$$\vec{E} = E e^{i(\omega t \mp \frac{2\pi n z}{\lambda})} \hat{x} \quad (\text{A1.12})$$

Note that the negative sign at the exponent is for a wave travelling in the forward direction. When the wave encounters a boundary, part of it is reflected backwards. This backward travelling light thus has the opposite sign at the exponent as the forward travelling wave.

The magnetic field vector can be expressed in terms of the same electric field amplitude E as in equation A1.12 if we note that Maxwell's Equation A1.3 gives a relationship between the two vectors. Evaluating the curl of the electric field vector as written in equation A1.12 and writing the unit vectors along the y- and z-axis as \hat{y} and \hat{z} respectively then yields:

$$\frac{\partial \vec{H}}{\partial t} = -\frac{c}{\mu} \left[\hat{y} \frac{\partial}{\partial z} E e^{i(\omega t \mp \frac{2\pi n z}{\lambda})} - \hat{z} \frac{\partial}{\partial y} E e^{i(\omega t \mp \frac{2\pi n z}{\lambda})} \right] \quad (\text{A1.13})$$

Since the magnetic permittivity μ is essentially unity for materials in the visible spectrum, equation A1.13 can be simplified to the following:

$$\frac{\partial \vec{H}}{\partial t} = \pm \omega n i E e^{i(\omega t \mp \frac{2\pi n z}{\lambda})} \hat{y} \quad (\text{A1.14})$$

$$\vec{H} = \pm n E e^{i(\omega t \mp \frac{2\pi n z}{\lambda})} \hat{y} \quad (\text{A1.15})$$

Equations A1.12 and A1.15 are general expressions describing the electric and magnetic fields of light in the visible wavelengths propagating in a medium with refractive index n .

Let us now consider a simple 3-phase model, as shown in **Figure A1.1**, composed of a substrate, an overlayer, and vacuum from which the light originates. The refractive indices of the 3 phases are designated as n_2 , n_1 and $n_0 = 1$ respectively. Also demonstrated in **Figure A1.1** is how the incident light would propagate in this 3-phase model: whenever light approaches an interface it is split into a beam that passes through and one that is reflected. The coordinate system is set up with the z-axis normal to the surface, while the origin is defined at the top of the overlayer (phase 1), which is of thickness d .

This discussion is based on the analysis by O. S. Heavens but slightly different: whereas the present discussion is a derivation for *absorptance*, Heavens performed an analysis on *reflectance*.⁹³ Through this discussion the percentage change in absorptance will be shown to increase linearly as a function of the thickness of the overlayer, i.e. phase 1, if the refractive indices of all phases stay unchanged.

From equations A1.12 and A1.15, expressions can be written for the electric and magnetic field vectors, which are sums of the individual forward and backward travelling components, present in each of the 3 phases. In writing these expressions the + and - superscripts designate the forward and the backward propagating wave

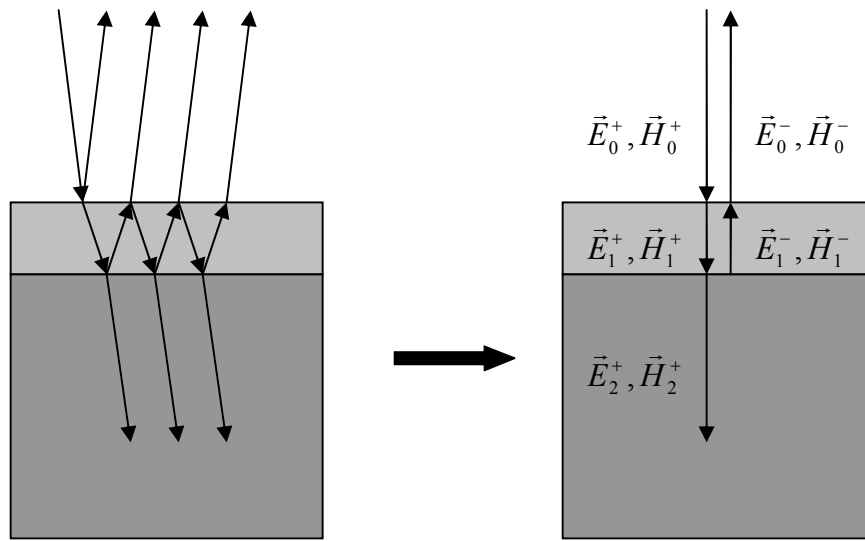


Figure A1.1: Schematic diagram of a 3-phase system

The light approaches from the top of this system. The diagram on the left demonstrates how light is reflected and transmitted at each interface between phases. On the right is a vector sum representation, where \vec{E} is the electric field vector, and \vec{H} the magnetic field vector. The notation for these vectors is such that the subscript designates the phase, while the superscript designates direction. The two representations are different, but mathematically equivalent.

respectively, while the subscripts designate the particular phase in question. Note that the refractive index of the phase 0, vacuum, is unity. We will limit this discussion to normal incidence. This significantly simplifies the physics since there is no angle dependence, and there is no distinction between s- and p-polarization in the light. This normal incidence is reflected in the following expressions:

$$\vec{E}_0^+ = E_0^+ e^{i\left(\frac{\omega t - 2\pi}{\lambda}\right)} \vec{x} \quad (\text{A1.16})$$

$$\vec{E}_0^- = E_0^- e^{i\left(\frac{\omega t + 2\pi}{\lambda}\right)} \vec{x} \quad (\text{A1.17})$$

$$\vec{E}_1^+ = E_1^+ e^{i\left(\frac{\omega t - 2\pi n_1 z}{\lambda}\right)} \vec{x} \quad (\text{A1.18})$$

$$\vec{E}_1^- = E_1^- e^{i\left(\frac{\omega t + 2\pi n_1 z}{\lambda}\right)} \vec{x} \quad (\text{A1.19})$$

$$\vec{E}_2^+ = E_2^+ e^{i\left(\frac{\omega t - 2\pi n_2 z}{\lambda}\right)} \vec{x} \quad (\text{A1.20})$$

$$\vec{H}_0^+ = E_0^+ e^{i\left(\frac{\omega t - 2\pi}{\lambda}\right)} \vec{y} \quad (\text{A1.21})$$

$$\vec{H}_0^- = -E_0^- e^{i\left(\frac{\omega t + 2\pi}{\lambda}\right)} \vec{y} \quad (\text{A1.22})$$

$$\vec{H}_1^+ = n_1 E_1^+ e^{i\left(\frac{\omega t - 2\pi n_1 z}{\lambda}\right)} \vec{y} \quad (\text{A1.23})$$

$$\vec{H}_1^- = -n_1 E_1^- e^{i\left(\frac{\omega t + 2\pi n_1 z}{\lambda}\right)} \vec{y} \quad (\text{A1.24})$$

$$\vec{H}_2^+ = n_2 E_2^+ e^{i\left(\frac{\omega t - 2\pi n_2 z}{\lambda}\right)} \vec{y} \quad (\text{A1.25})$$

For the model to be physical, the total electric and magnetic field vectors must each be continuous when crossing the interface boundaries. This translates into the following four expressions for the two interfaces at $z = 0$ (equations A1.26, A1.27) and $z = d$ (equations A1.28, A1.29) respectively:

$$E_0^+ + E_0^- = E_1^+ + E_1^- \quad (\text{A1.26})$$

$$E_0^+ - E_0^- = n_1(E_1^+ - E_1^-) \quad (\text{A1.27})$$

$$E_1^+ e^{-i\frac{2\pi n_1 d}{\lambda}} + E_1^- e^{i\frac{2\pi n_1 d}{\lambda}} = E_2^+ e^{-i\frac{2\pi n_2 d}{\lambda}} \quad (\text{A1.28})$$

$$n_1 \left(E_1^+ e^{-i\frac{2\pi n_1 d}{\lambda}} - E_1^- e^{i\frac{2\pi n_1 d}{\lambda}} \right) = n_2 E_2^+ e^{-i\frac{2\pi n_2 d}{\lambda}} \quad (\text{A1.29})$$

Combining the two equations for each interface, it can then be shown that the amplitudes of the electric fields in each phase can be expressed as a linear combination of the amplitudes of the electric fields in the next phase:

$$E_0^+ = \frac{1}{t_1} E_1^+ + \frac{r_1}{t_1} E_1^- \quad (\text{A1.30})$$

$$E_0^- = \frac{r_1}{t_1} E_1^+ + \frac{1}{t_1} E_1^- \quad (\text{A1.31})$$

$$E_1^+ e^{-i\frac{2\pi n_1 d}{\lambda}} = \frac{1}{t_2} E_2^+ e^{-i\frac{2\pi n_2 d}{\lambda}} \quad (\text{A1.32})$$

$$E_1^- e^{i\frac{2\pi n_1 d}{\lambda}} = \frac{r_2}{t_2} E_2^+ e^{-i\frac{2\pi n_2 d}{\lambda}} \quad (\text{A1.33})$$

In these four expressions, the various r 's and t 's are linear combinations of the refractive indices: called Fresnel coefficients:

$$r_1 = \frac{n_0 - n_1}{n_0 + n_1} = \frac{1 - n_1}{1 + n_1} \quad (\text{A1.34})$$

$$r_2 = \frac{n_1 - n_2}{n_1 + n_2} \quad (\text{A1.35})$$

$$t_1 = \frac{2n_0}{n_0 + n_1} = \frac{2}{1 + n_1} \quad (\text{A1.36})$$

$$t_2 = \frac{2n_1}{n_1 + n_2} \quad (\text{A1.37})$$

Dividing equation A1.33 from A1.32 followed by some rearrangement yields an expression that relates the amplitudes of the two electric field components in phase 1 with each other:

$$E_1^- = r_2 E_1^+ e^{-i\frac{4\pi n_1 d}{\lambda}} \quad (\text{A1.38})$$

Substitution of equation A1.38 into A1.30 and A1.31 yields, respectively:

$$E_0^+ = \frac{1}{t_1} E_1^+ \left(1 + r_1 r_2 e^{-i\frac{4\pi n_1 d}{\lambda}} \right) \quad (\text{A1.39})$$

$$E_0^- = \frac{1}{t_1} E_1^+ \left(r_1 + r_2 e^{-i\frac{4\pi n_1 d}{\lambda}} \right) \quad (\text{A1.40})$$

The ratio between the electric field amplitude of the beam reflected off the first interface and that of the incident beam is related to the reflectance of the system.

Designating this ratio as $r(d)$, it can be expressed as:

$$r(d) = \frac{E_0^-}{E_0^+} = \frac{r_1 + r_2 e^{-2i\beta}}{1 + r_1 r_2 e^{-2i\beta}} \quad \beta = \frac{2\pi n_1 d}{\lambda} \quad (\text{A1.41})$$

The variable d measures the thickness of phase 1. If the overlayer is a thin film such that $d \ll \lambda$, where λ is on the order of 100 nm, approximations can be made to

simplify equation A1.41. By expressing the exponential terms as a series and ignoring higher order terms of β since $\beta \ll 1$, i.e.,

$$e^{-2i\beta} \approx 1 - 2i\beta \quad (\text{A1.42})$$

we can write:¹³⁰

$$r(d) \approx \frac{r_1 + r_2(1 - 2i\beta)}{1 + r_1 r_2(1 - 2i\beta)} \quad (\text{A1.43})$$

So far in this discussion all derivations have been done in electric and magnetic fields, which are not directly measured in experiments. Instead, the calorimeter is sensitive to energies. Electric and magnetic fields are related to energy by the Poynting vector, which represents energy flux:

$$\vec{S} = \frac{c}{4\pi} \vec{E} \times \vec{H} \quad (\text{A1.44})$$

The Poynting vector points toward the direction of energy flow, while its magnitude, $|\vec{S}|$, gives the energy per area per time. The reflectance R of the system is therefore given by the ratio of $|\vec{S}|$ for the reflected beam to that for the incident beam at the first interface:

$$R = \left| \frac{\vec{S}_0^-}{\vec{S}_0^+} \right| = \left| \frac{\vec{E}_0^- \times \vec{H}_0^-}{\vec{E}_0^+ \times \vec{H}_0^+} \right| \quad (\text{A1.45})$$

Substituting in the respective field vectors from equations A1.16, A1.17, A1.21, and A1.22 thus gives a relationship between the reflectance R and the previously defined electric field amplitude ratio r :

$$R(d) = \left| \frac{E_0^-}{E_0^+} \right|^2 = |r(d)|^2 \quad (\text{A1.46})$$

Furthermore, since the energy that is not reflected is absorbed somewhere in the multilayer, and that there is no transmittance given a thick enough substrate, absorptance is related to reflectance by the simple expression:

$$A(d) = 1 - R(d) \quad (\text{A1.47})$$

The last step of this derivation is to determine the behaviour that has been measured, namely the percentage absorptance change. Noting that the pristine substrate can be represented using the multilayer model by requiring that the overlayer (phase 1) thickness d be 0, the percentage absorptance change can be expressed as:

$$\begin{aligned} \frac{A(d) - A(0)}{A(0)} &= \frac{A(d)}{A(0)} - 1 \\ &= \frac{1 - R(d)}{A(0)} - 1 = \frac{1 - \frac{R(d)}{R(0)} R(0)}{A(0)} - 1 = \frac{1 - \left| \frac{r(d)}{r(0)} \right|^2 R(0)}{A(0)} - 1 \end{aligned} \quad (\text{A1.48})$$

In order to obtain an expression for the percentage absorptance change then, the ratio of $r(d)$ to $r(0)$ needs to be evaluated. To simplify the resulting expression, the same thin film limit expression from equation A1.43 is used:

$$\frac{r(d)}{r(0)} \approx \frac{\frac{r_1 + r_2(1 - 2i\beta)}{1 + r_1 r_2(1 - 2i\beta)}}{\frac{r_1 + r_2}{1 + r_1 r_2}} = \frac{\frac{r_1 + r_2(1 - 2i\beta)}{r_1 + r_2}}{\frac{1 + r_1 r_2(1 - 2i\beta)}{1 + r_1 r_2}} = \frac{1 - \frac{2i\beta r_2}{r_1 + r_2}}{1 - \frac{2i\beta r_1 r_2}{1 + r_1 r_2}} \quad (\text{A1.49})$$

In order to simplify this expression further, we concentrate on the denominator. It can be rearranged, and subsequently expanded in its entirety as a series around β ; discarding higher order terms in β then yields:

$$\begin{aligned} \frac{1}{1 - \frac{2i\beta r_1 r_2}{1 + r_1 r_2}} &= \frac{1 + r_1 r_2}{1 + r_1 r_2 - 2i\beta r_1 r_2} \\ &\approx 1 + \left[(1 + r_1 r_2) \frac{-(-2ir_1 r_2)}{(1 + r_1 r_2 - 2i\beta r_1 r_2)^2} \right]_{\beta=0} = 1 + \frac{2i\beta r_1 r_2}{1 + r_1 r_2} \end{aligned} \quad (\text{A1.50})$$

After substituting equation A1.50 back into A1.49 and once again ignoring higher terms in β , the ratio of $r(d)$ to $r(0)$ we seek can be written as:

$$\frac{r(d)}{r(0)} \approx \left(1 - \frac{2i\beta r_2}{r_1 + r_2} \right) \left(1 + \frac{2i\beta r_1 r_2}{1 + r_1 r_2} \right) \approx 1 - 2i\beta \frac{r_2(1 - r_1^2)}{(r_1 + r_2)(1 + r_1 r_2)} \quad (\text{A1.51})$$

We recall from equation A1.41 that $\beta = 2\pi n_1 d / \lambda$, thus substitution into equation A1.51 gives:

$$\frac{r(d)}{r(0)} \approx 1 - i \frac{4\pi d \gamma}{\lambda} \quad \gamma = \frac{n_1 r_2 (1 - r_1^2)}{(r_1 + r_2)(1 + r_1 r_2)} \quad (\text{A1.52})$$

Since the factor γ in equation A1.52 is composed of, ultimately, refractive indices of the various phases (all the r 's with subscripts are Fresnel coefficients that are

calculated from refractive indices), and they can be complex values if they absorb light, γ is also a complex number. This means that in order to calculate the percentage absorptance change according to equation A1.48, the real and complex parts of γ , which are designated as $\text{Re}(\gamma)$ and $\text{Im}(\gamma)$ respectively, must be written out separately, since the magnitude of a complex number is calculated by taking the square root of the product between the complex conjugate pair. The ratio of reflectances, as required in equation A1.48, can then be written out as:

$$\begin{aligned}\left|\frac{r(d)}{r(0)}\right|^2 &\approx \left(1 - i \frac{4\pi d}{\lambda} [\text{Re}(\gamma) + i \text{Im}(\gamma)]\right) \left(1 - i \frac{4\pi d}{\lambda} [\text{Re}(\gamma) + i \text{Im}(\gamma)]\right)^* \\ &= \left(1 + \frac{4\pi d}{\lambda} \text{Im}(\gamma) - i \frac{4\pi d}{\lambda} \text{Re}(\gamma)\right) \left(1 + \frac{4\pi d}{\lambda} \text{Im}(\gamma) + i \frac{4\pi d}{\lambda} \text{Re}(\gamma)\right)\end{aligned}\quad (\text{A1.53})$$

Continuing the thin film approximation, if higher order terms in d / λ are ignored, equation A1.53 can be further simplified:

$$\left|\frac{r(d)}{r(0)}\right|^2 \approx 1 + \frac{8\pi d}{\lambda} \text{Im}(\gamma)\quad (\text{A1.54})$$

Finally, putting equation A1.54 back into A1.48 and rearranging the result gives an expression for the percentage absorptance change:

$$\frac{A(d) - A(0)}{A(0)} = -\frac{8\pi}{\lambda} \frac{\text{Im}(\gamma)}{\text{R}(0)} d\quad (\text{A1.55})$$

This equation indicates that if the refractive index of the substrate does not change over the course of overlayer growth, and that the overlayer's refractive index is independent of thickness, the percentage absorptance change should be linear for a 3-

phase system. It should be noted that according to this expression, the overlayer needs not be absorbing for the absorptance to change linearly; the overlayer could be a dielectric material, and a linear behaviour would still be observed. However, in order to observe a non-zero absorptance change, $\text{Im}(\gamma)$ must be non-zero as well, i.e., there must be at least one phase in the system that has a dielectric constant with a non-zero imaginary part. In other words, at least one phase needs to be absorbing in order to observe a linear percentage change in absorptance as a function of overlayer thickness.

The following discussion extends the concepts originally put forth by J. D. E. McIntyre and D. E. Aspnes,¹³⁰ which we have detailed above: it is an attempt to show that the result in equation A1.55 also applies to a 4-phase system. Indeed, this result further applies to systems with any number of phases, so long as the only phase with a changing thickness is the overlayer (phase 1), and that all refractive indices stay constant.

Expressions analogous to equations A1.30 through A1.33 can be written for a 4-phase system, with the interfaces at $z = 0$, $z = d_1$, and $z = d_2$:

$$E_0^+ = \frac{1}{t_1} E_1^+ + \frac{r_1}{t_1} E_1^- \quad (\text{A1.56})$$

$$E_0^- = \frac{r_1}{t_1} E_1^+ + \frac{1}{t_1} E_1^- \quad (\text{A1.57})$$

$$E_1^+ e^{-i\frac{2\pi n_1 d_1}{\lambda}} = \frac{1}{t_2} E_2^+ e^{-i\frac{2\pi n_2 d_1}{\lambda}} + \frac{r_2}{t_2} E_2^- e^{i\frac{2\pi n_2 d_1}{\lambda}} \quad (\text{A1.58})$$

$$E_1^- e^{i\frac{2\pi n_1 d_1}{\lambda}} = \frac{r_2}{t_2} E_2^+ e^{-i\frac{2\pi n_2 d_1}{\lambda}} + \frac{1}{t_2} E_2^- e^{i\frac{2\pi n_2 d_1}{\lambda}} \quad (\text{A1.59})$$

$$E_2^+ e^{-i\frac{2\pi n_2 (d_1 + d_2)}{\lambda}} = \frac{1}{t_3} E_3^+ e^{-i\frac{2\pi n_3 (d_1 + d_2)}{\lambda}} \quad (\text{A1.60})$$

$$E_2^- e^{i \frac{2\pi n_2(d_1+d_2)}{\lambda}} = \frac{r_3}{t_3} E_3^+ e^{-i \frac{2\pi n_3(d_1+d_2)}{\lambda}} \quad (\text{A1.61})$$

Dividing equation A1.60 from A1.61 followed by rearrangement yields:

$$E_2^- = r_3 E_2^+ e^{-i \frac{4\pi n_2(d_1+d_2)}{\lambda}} \quad (\text{A1.62})$$

Substituting equation A1.62 into A1.58 and A1.59 gives, respectively:

$$E_1^+ e^{-i \frac{2\pi n_1 d_1}{\lambda}} = \frac{1}{t_2} E_2^+ e^{-i \frac{2\pi n_2 d_1}{\lambda}} \left(1 + r_2 r_3 e^{-i \frac{4\pi n_2 d_2}{\lambda}} \right) \quad (\text{A1.63})$$

$$E_1^- e^{i \frac{2\pi n_1 d_1}{\lambda}} = \frac{1}{t_2} E_2^+ e^{-i \frac{2\pi n_2 d_1}{\lambda}} \left(r_2 + r_3 e^{-i \frac{4\pi n_2 d_2}{\lambda}} \right) \quad (\text{A1.64})$$

The electric fields of the forward and backward travelling light in phase 1 can then be obtained by dividing equation A1.64 from A1.63, followed by some rearrangement:

$$E_1^- = \alpha E_1^+ e^{-i \frac{4\pi n_1 d_1}{\lambda}} \quad \alpha = \frac{r_2 + r_3 e^{-i \frac{4\pi n_2 d_2}{\lambda}}}{1 + r_2 r_3 e^{-i \frac{4\pi n_2 d_2}{\lambda}}} \quad (\text{A1.65})$$

At this point, in order to evaluate the percentage absorbance change, equation A1.65 needs to be substituted into equation A1.56 and A1.57. The subsequent two expressions could then be used for writing the ratio of \vec{E}_0^- to \vec{E}_0^+ . Alternatively, we present the argument as follows.

Equation A1.38, which gives an expression for \vec{E}_1^- in the 3-phase system, is:

$$E_1^- = r_2 E_1^+ e^{-i \frac{4\pi n_1 d}{\lambda}} \quad (\text{A1.38})$$

It can be seen that the only difference between the expressions for \vec{E}_1^- in the 3-phase equations A1.38 and corresponding 4-phase equation A1.65 is that the factor r_2 in A1.38 is replaced by a new factor α in A1.65. Noting that these expressions are both substituted into the same equations for the subsequent derivation (equations A1.30 and A1.31 in the 3-phase discussion are identical to A1.56 and A1.57 in the 4-phase) and that α is independent of the phase 1 thickness, the evaluation of percentage absorptance change in the current discussion proceeds exactly as previously. Thus the expression for percentage absorptance change for a 4-phase system is exactly as has been shown in equation A1.55, except that the factor γ has all references to r_2 replaced with α , which is an effective Fresnel coefficient. This shows then the percentage absorptance change is still linear with d when it is small.

If one is to look more closely at these thin film expressions, it can be observed that similar kinds of simplification can be realized in systems with even more layers. For instance, in the case of a 5-phase system equation A1.65 would give the expression for \vec{E}_2^- instead of \vec{E}_1^- with the subscripts of all the symbols incremented by one and d_1 replaced by $\sum_{j=1}^{k-3} d_j$ where $k = 5$ is the number of phases. This expression is of the same form as equation A1.62 for the 4 phase system other than some constants; as a result, the linear dependence of percentage absorptance change on the overlayer thickness is unchanged. This argument can be repeated for systems with more layers, i.e., no matter how many layers there are in a system, the growth of an overlayer causes a linear increase in absorptance in the thin film limit, where the thickness of the overlayer is much smaller than the wavelength of the incident light.